UNIVERSITÀ
DEGLI STUDI
DI PADOVA

Università degli Studi di Padova

Dipartimento di Geoscienze

Ph.D. COURSE IN: EARTH SCIENCES
SERIES XXXI

GEOPHYSICAL CHARACTERIZATION OF GAS HYDRATE SYSTEMS OF THE SOUTH SHETLAND MARGIN (ANTARCTICA)

Thesis written with the financial contribution of China Scholarship Council (grant number 201506400061)

Coordinator: Prof. Claudia Agnini
Supervisor: Prof. Giorgio Cassiani
Co-Supervisor: Dr. Umberta Tinivella
Dr. Michela Giustiniani

Ph.D. student: Sha Song

Abstract

During the last few decades, interest in gas hydrates has been increasing significantly because of their economic potential as future energy source and their potential role in geohazards and global climate change. The global climate change is a particularly sensitive issue for the Polar Regions, such as Antarctica. In the South Shetland margin (Antarctic Peninsula), the occurrence of a potential gas hydrate reservoir has been demonstrated from the analysis of geophysical data acquired during three Italian Antarctic cruises. In order to enhance the knowledge of gas hydrate systems, I analyzed Ocean Bottom Seismometer (OBS) and coincident multi-channel seismic (MCS) data acquired in 2004. The main objectives of this thesis are to estimate the distributions and concentrations of gas hydrate and free gas within the sediments, and to investigate the system's petrophysical properties.

Travel time inversion and forward modeling of OBS data were performed to estimate detailed P- and S-wave velocity fields. The P-wave velocity field was determined by the inversion of refractions and reflections in OBS data, while the S-wave velocity field was obtained by ray-tracing forward modeling of the converted S-waves from the horizontal components of OBS data. Several velocity models were tested in order to reduce the errors caused by the spatial drift of the OBS from the MCS line during sinking, and the errors from inversion. The final velocity model shows that P-wave velocity increases gradually with depth down to the bottom simulating reflection (BSR) at approximately 510-650 m below the seafloor. The layer with high P-wave velocity of 2.0-2.1 km/s just above the BSR can be associated with the presence of gas hydrates. Below the BSR, a low velocity layer of 1.4-1.6 km/s is observed, which indicates the presence of free gas. From the analysis of critical refractions in OBS data, the base of free gas layer (BGR) occurs at a depth varying between 80-160 m below the BSR. Forward modeling of converted S-waves in OBS data allows us to obtain Poisson's ratio estimates. We observe that Poisson's ratios are fairly uniform within each layer and they show good agreement with previous study performed in this area. The comparison of Poisson's ratio indicates that the gas hydrate reservoir shows no significant regional variations.

The resulting velocity fields were translated in terms of gas hydrate and free gas concentrations, using a modified Biot-Geerstma-Smit theory. The results show that hydrate concentration in the layer just above the BSR ranges from 10% to 15% of total volume, and free gas concentration is approximately 0.3% to 0.8% of total volume assuming a uniform gas distribution.

Part of this research related to the OBS analysis and gas-phase estimation, has been published in the international journal Energies (Song et al., 2018) and included in the Appendix 1.

Contents

Abstract **III**

Contents **IV**

List of Figures **VII**

List of Tables **IX**

Acknowledgments **X**

1 Introduction **1**

1.1 Gas hydrates 1

1.1.1 Gas hydrate structures 1

1.1.2 Gas hydrate stability zone 3

1.1.3 Gas hydrate morphology in nature 5

1.1.4 Geophysical methods for marine gas hydrate studies 7

1.1.5 Importance of gas hydrates 11

1.2 Gas hydrates on the South Shetland margin 14

1.2.1 Geological setting 14

1.2.2 Previous geophysical studies 16

1.3 Objectives and outline of thesis 18

2 Seismic data and processing **20**

2.1 Data acquisition 20

2.2 MCS data processing 22

2.3 OBS data processing 24

2.3.1 OBS relocation 24

2.3.2 Processing of the hydrophone and vertical components 27

2.3.3 Processing of the horizontal components 29

2.4 Summary 31

3 Seismic traveltime inversion 32

3.1 Introduction 32

3.2 Theoretical background 32

3.2.1 Model parameterization 33

3.2.2 Forward modeling 34

3.2.3 Inversion 35

3.3 P-wave velocity modeling 37

3.3.1 Event identification 37

3.3.2 Modeling 41

3.4 S-wave velocity modeling 44

3.4.1 Event identification 44

3.4.2 Modeling 46

3.5 Results: velocity model 48

3.6 Uncertainty of the velocity model 50

3.7 Modified velocity model 51

3.8 Summary 53

4 Estimation of gas hydrate and free gas concentrations 55

4.1 Introduction 55

4.2 Available theories in literature 56

4.2.1 Empirical relations 56

4.2.2 Three-phase effective-medium theory (TPEM) 58

4.2.3 Differential effective-medium theory (DEM) 59

4.2.4 Three-phase Biot-theory (TPB) 60

4.3 Approximated modified-Biot theory 61

4.4 Estimation of gas hydrate and free gas concentrations 66

4.4.1 Porosity estimation 66

4.4.2 Concentration estimation by using inverted porosity 69
4.4.3 Concentration estimation by using Hamilton's porosity 71
4.5 Summary 75

5 Discussion **76**

5.1 BSR analysis 76
5.2 Comparison with previous results 78
5.2.1 Velocity model 78
5.2.2 Gas hydrate and free gas concentrations 78
5.3 Implications of the study 85

6 Conclusions **87**

References **88**

Appendix 1 **103**

List of Figures

Figure 1.1: Typical structure of gas hydrate 2
Figure 1.2: Gas hydrate crystal structures..... 2
Figure 1.3: Location of test exploitation, sampled and inferred gas hydrate occurrences in oceanic sediments of outer continental margins and permafrost regions..... 4
Figure 1.4: Gas hydrate stability zone in marine (A) and permafrost (B) settings..... 4
Figure 1.5: Four types of natural gas hydrate deposition in sediments 6
Figure 1.6: Microscopic models of gas hydrate formation: pore-filling (A), load-bearing (B), and cementation (C)..... 6
Figure 1.7: Part of seismic section of MCS line BSRstar8..... 8
Figure 1.8: Marine seismic acquisition systems, including single- and multi-channel seismic streamer, deep-towed multichannel streamer, and Ocean-bottom seismometer..... 10
Figure 1.9: (a) Shaded relief of bathymetric data derived from gravimetric data. (b) Shaded relief of the high resolution morpho-bathymetry image..... 15
Figure 2.1: Bathymetric map of the study area indicating the locations of seismic lines and OBSs.. 21
Figure 2.2: Processing sequence flow..... 23
Figure 2.3: Example of one shot gather before and after processing..... 23
Figure 2.4: Time migrated section of part of MCS line BSRstar8.. 24
Figure 2.5: Results of OBS relocation..... 26
Figure 2.6: The fit between calculated and observed travel times (a) and the time residuals (b) for OBS 6..... 26
Figure 2.7: The fit between calculated and observed travel times (a) and the time residuals (b) for OBS 7..... 27
Figure 2.8: Data example from OBS 7. 28
Figure 2.9: An example of hodogram analysis.. 30
Figure 2.10: Rotation of horizontal components of OBS 7. 31
Figure 3.1: An example of velocity model parametrization. 33
Figure 3.2: Ray groups are modeled via ray tracing: refracted waves, reflected waves, and head-waves..... 35
Figure 3.3: (a) Stack section of part of MCS line BSRstar8; (b) and (c) Correlation of the hydrophone component of OBS 7 and the MCS stack section; (d) Close-up view of OBS panel (c) showing the BSR..... 39
Figure 3.4: Travel time picks of P-wave reflections from hydrophone component of OBS 7..... 40
Figure 3.5: Travel time picks of P-wave refraction from hydrophone component of OBS 7.. 40
Figure 3.6: The relative error of offset for OBS 6..... 41
Figure 3.7: The relative error of offset for OBS 7..... 42

Figure 3.8: Top: P-wave ray diagram modeled on OBS 7; Bottom**:** the fit between calculated and observed travel times 43
Figure 3.9: Ray paths of PP-, SS- and PS-waves for OBS.. 45
Figure 3.10: (a) Inline component of OBS 7 showing travel time picks of PS-waves; (b) PS-wave ray diagram modeled on OBS 7; (c) The fit between calculated and observed travel times 47
Figure 3.11: P-wave velocity model obtained after joint inversion of MCS and OBS data. 49
Figure 3.12: P- and S-wave velocity and Poisson's ratio profiles extracted at the location of OBS 7. 49
Figure 3.13: An example of sensitivity analysis applied to the velocity of Layer L2.. 51
Figure 3.14: Modified P-wave velocity model. 52
Figure 3.15: The P- and S-wave velocity and Poisson's ratio profile extracted at the locations of OBS 6 (a) and OBS 7 (b). 53
Figure 4.1: Comparison between the three-phase Biot theory and the approximation for seismic frequency.. 63
Figure 4.2: Compressional velocity versus free-gas saturation calculated with the uniform-saturation model and the patchy-saturation model 64
Figure 4.3: Poisson's ratio versus free-gas saturation calculated with the uniform-saturation model and the patchy-saturation model 64
Figure 4.4: The porosity profiles extracted at the locations of OBS 6 (a) and OBS 7 (b).. 68
Figure 4.5: The porosity section determined by velocity fields. 68
Figure 4.6: The seismic velocity profiles after inversion and reference velocity curves extracted at the locations of OBS 6 (a) and OBS 7 (b). 70
Figure 4.7: Concentration section of gas hydrate and free gas based on estimated porosity. 71
Figure 4.8: The final P-wave velocity model obtained after travel time inversion of MCS and OBS data. 73
Figure 4.9: The final seismic velocity profiles after inversion and reference velocity curves and Poisson's ratio profiles extracted at the locations of OBS 6 (a) and OBS 7 (b). 74
Figure 4.10: Concentration section of gas hydrate and free gas based on Hamilton's porosity. 74
Figure 5.1: The theoretical and observed BSR depths 77
Figure 5.2: Bathymetric map showing the locations of chirp profiles 80
Figure 5.3: (a) Example of chirp profile 43; (b) Seafloor reflection coefficient obtained from this chirp profile. 81
Figure 5.4: (a) Example of chirp profile 29; (b) Seafloor reflection coefficient obtained from this chirp profile 82
Figure 5.5: Seafloor reflectivity map derived from chirp data. 83
Figure 5.6: Seafloor reflection coefficients obtained from OBS 6, OBS 7, and chirp data 84

List of Tables

Table 2.1 Deployed and relocated coordinates of OBSs 25
Table 3.1 The summary of P-wave velocity modeling for OBS 7 44
Table 3.2 The summary of PS-wave velocity modeling for OBS 7 46
Table 3.3 Percentage errors of P-wave and S-wave velocities estimated from the sensitivity analysis 51
Table 3.4 Percentage errors of P-wave and S-wave velocities in the modified model. 52
Table 4.1 List of parameters and variation of material properties versus depth 65
Table 4.2 Values of main parameters used in equations (4.4) and (4.5) 69
Table 4.3 Percentage errors of P-wave and S-wave velocities in the final model 73
Table 5.1 Average reflection coefficient at the seafloor obtained from chirp and OBS data 84

Acknowledgments

First of all, I would like to express my sincere and heartfelt thanks to my supervisor Prof. Giorgio Cassiani and co-supervisors Dr. Umberta Tinivella and Dr. Michela Giustiniani for giving me this wonderful opportunity to do Ph.D. under their guidance at the University of Padova and Istituto Nazionale di Oceanografia e di Geofisica Sperimentale (OGS). I am profoundly grateful for their continuous support, advice, patience, expertise, and funding throughout my Ph.D. project. They have provided me extensive personal and professional guidance and taught me a great deal about both scientific research and life in general. I have learned and benefited a lot from their valuable suggestions and discussions during my study, which will be the treasure of my life. I appreciate their support for all the conferences, courses, summer schools and seismic data acquisition I have participated during the three years. Thank you very much for everything!

A special thanks to Prof. Xuewei Liu from China University of Geosciences (Beijing), for his support and recommendation during my application of Ph.D. project at the University of Padova, and continuous concern and help in these three years. I am also very grateful to all my former colleagues and officemates for supporting my choice to undertake this Ph.D. project. I especially thank to Dr. Jiachun You for his help and helpful discussions.

I would also like to thank Prof. Stefan Bünz and Sunny Singhroha for enhancing my knowledge and skills on the analysis of ocean-bottom seismic data, during one month STSM mission I conducted at the Centre of Excellence for Arctic Gas Hydrates, Environment and Climate (CAGE), UiT The Arctic University of Norway. Thanks to the COST-MIGRATE project group for giving me this opportunity and providing the financial support for the STSM mission.

During these three years, I was fortunate to study at the university and OGS. I would like to thank all faculty and staff, researchers and students from both institutions. Particularly, thanks to Prof. Fabrizio Nestola, Prof. Claudia Agnini, Prof. Andrea D'Alpaos, Prof. Angelo Camerlenghi and Dr. Mounir Ghribi for their support and organization during my Ph.D. courses and activities; thanks also to Dr. Laura Busato, Dr. Jacopo Boaga, Dr. Kim Anne Barchi, Dr. Sula Milani, Dr. Chengying Bai, Dr. Xiuli Mao, Xin Jin, Xiaohuan Sun, Xia Li and Chiara Balestrieri for their support and help.

I gratefully acknowledge the financial support for my Ph.D. project, which provided by the China Scholarship Council (CSC). I am also grateful to the scientists and the technicians participating in the Antarctic cruises.

Last but not least, I would like to thank my parents for all their emotional support and encouragement throughout this thesis and my life in general. Their love, support, and sacrifices have been my biggest motivation over the years.

Chapter 1

Introduction

1.1 Gas hydrates

1.1.1 Gas hydrate structures

Gas hydrates are ice-like crystalline solids composed of water and gas molecules (Sloan, 1998). Gas hydrates are known as clathrates, which mean that guest gas molecules are engaged in a host framework of water molecules (Figure 1.1). The gas molecules interact with water molecules through van der Waals (nonpolar) forces. Methane is the predominant gas forming gas hydrates, but other higher-order hydrocarbons, carbon dioxide and hydrogen sulphide may also occur (Sloan and Koh, 2008).

Generally, gas hydrate structures are divided into three types: structure I (sI), structure II (sII), and structure H (sH) (Figure 1.2). The formation of different structures depends on the nature and the size of the largest guest molecules (Sloan, 1998; Kirchner et al., 2004). sI hydrate consists of pentagonal dodecahedrons and tetrakaidecahedrons, sII hydrate consists of pentagonal dodecahedrons and hexakaidecahedrons, while sH hydrate consists of small and large guest molecules. sI hydrate is the most common occurring hydrate in the nature that is formed with gases such as methane, ethane, carbon dioxide or hydrogen sulphide. The presence of components larger than ethane (propane, butane) leads to the formation of sII hydrate. Larger hydrocarbon molecules form the sH hydrate when methane is present.

Methane hydrate complexes can intercalate in the expected variety of clays present in gas hydrate reservoirs. Some order of the methane hydrate structure is preserved within the interlayer and is related to the formation of methane clathrate structures with H_2O and the clay surfaces and the

formation of a hydrogen-bonded network in the interlayer (e.g., Cygan et al., 2004). Smectites are expandable 2:1 layer type clay minerals and they are pervasive on the ocean floor and it is present at continental margins to oceanic ridges Smectites (e.g., Sposito, 1984; Chamley, 1997). The formation of smectite-methane-hydrate complexes depend on the swelling capacity in the smectite. In samples with limited swelling properties, methane hydrate is formed in the pore spaces between particles and on the external surface of clays (e.g., Sutton and Sposito 2001; Martos-Villa et al., 2014).

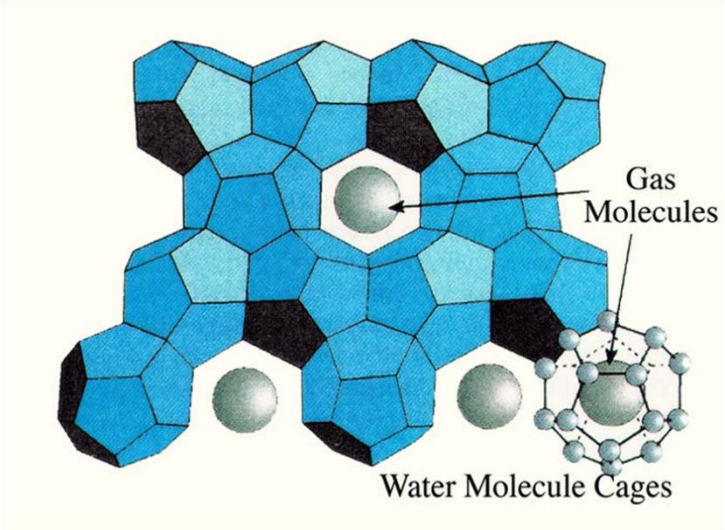

Figure 1.1: Typical structure of gas hydrate

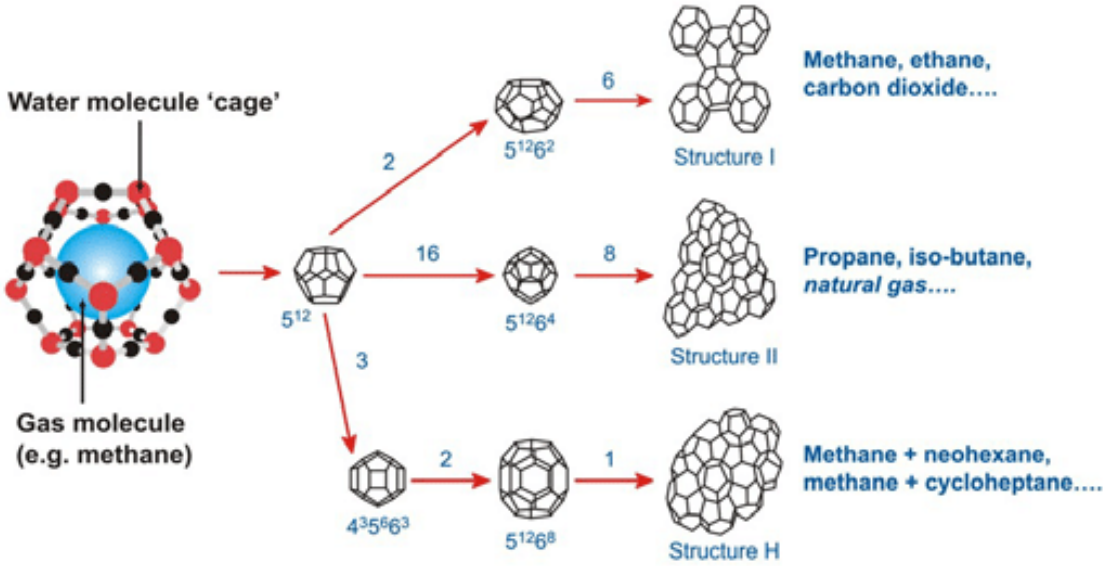

Figure 1.2: Gas hydrate crystal structures (from Collett et al., 2009).

1.1.2 Gas hydrate stability zone

Gas hydrates are common in permafrost regions and beneath the sea in sediments of outer continental margins (Figure 1.3). The formation of gas hydrates need appropriate conditions of low temperature and high pressure, and when sufficient gas and water are available. In marine sediments, gas hydrates are commonly found in the regions where water depths exceed about 300 m at high latitudes and 500 m in temperate latitudes, between 135 and 1000 m below the seafloor, depending on the geothermal gradient (Kvenvolden, 1988, 1993; Ruppel, 2011). The zone where gas hydrates are stable is called the gas hydrate stability zone (GHSZ). Figure 1.4 shows a typical situation of stability zone for marine and permafrost settings (Ruppel, 2011). In oceanic sediments at an arbitrary water depth of 1200 m (Figure 1.4A), temperature gradually decreases with water depth, and a minimum value near 0 ℃ is reached at the seafloor; below the seafloor, temperatures steadily increase. From the theoretical phase diagram, gas hydrate can form anywhere local thermal conditions are colder than the phase boundary at any given depth, i.e. gas hydrate is in theory stable at the water depth greater than about 600 m to a depth of about 200 m below the seafloor. For permafrost settings (Figure 1.4B), gas hydrate is stable from about 200 to 600 m within bottom part of permafrost-bound sediments and extending to 600 m to 1100 m beneath the base of permafrost. Actually, the phase diagram is the equilibrium curve and it depends on the gas composition and the pore water salinity. It shows only the region where gas hydrate is stable, not where it actually occurs in nature. For the formation and preservation of gas hydrates, methane has to be present above its local solubility in sediment pore waters or in the water column.

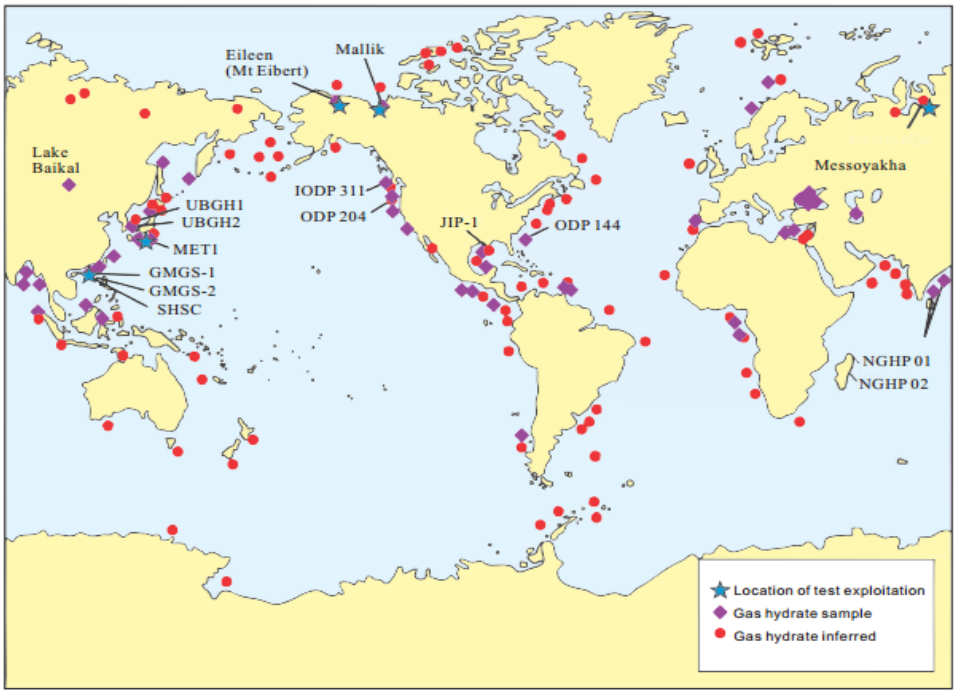

Figure 1.3: Location of test exploitation, sampled and inferred gas hydrate occurrences in oceanic sediments of outer continental margins and permafrost regions. (SHSC-Shenhu Test Exploitation; IODP-Integrated Ocean Drilling Program; UBGH-Ulleung Basin Gas Hydrate Expedition; ODP-Ocean Drilling Program; JIP-Joint Industry Project; METI-Ministry of Economy, Trade, and Industry; GMGS-Guangzhou Marine Geological Survey; NGHP-India National Gas Hydrate Program. from Cui et al., 2018).

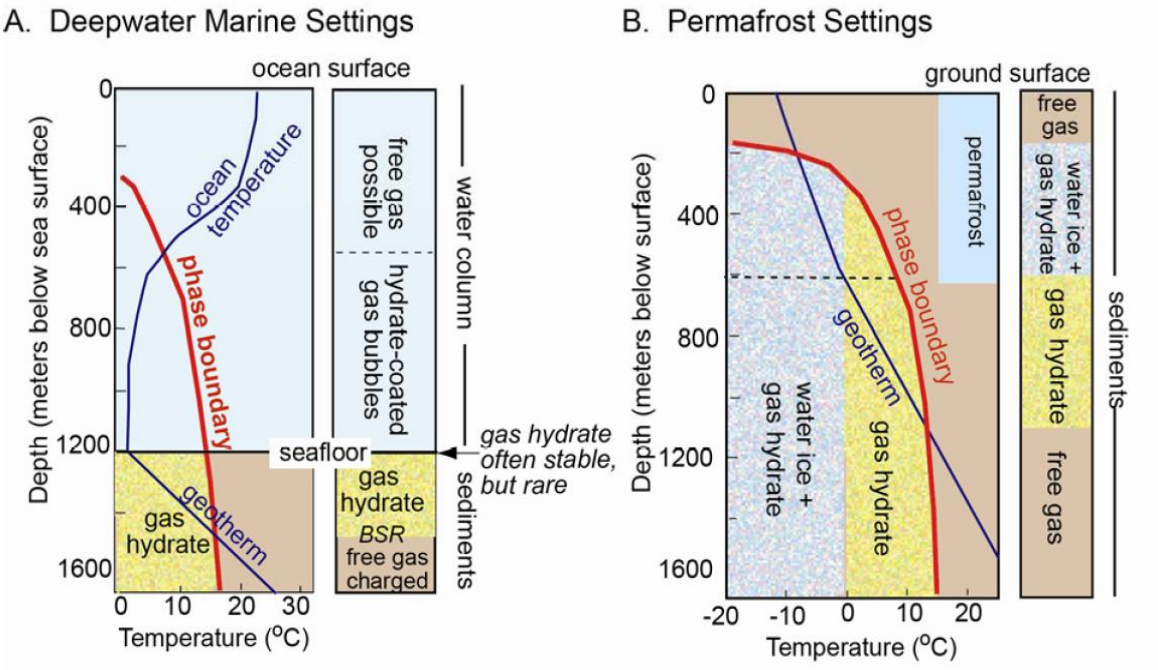

Figure 1.4: Gas hydrate stability zone in marine (A) and permafrost (B) settings (from Ruppel, 2011).

1.1.3 Gas hydrate morphology in nature

The morphology of gas hydrates has large influences on the physical properties of the sediment-hydrate matrix. It is important for understanding the formation of gas hydrate deposits, for estimating the concentrations of gas hydrate from geophysical data, and for predicting their response to climate change or commercial production (Holland et al., 2008). Gas hydrates can be considered on two scales: macro-morphology and micro-morphology. Marco-morphology describes the structure of hydrate formation in the sediments at large scale, while micro-morphology refers to the interaction of gas hydrate with host sediments at the pore scale.

The available data show that hydrates can form in sediments in four distinct morphologies: disseminated, nodular, vein, and massive (Malone, 1985) (Figure 1.5). Disseminated hydrate occurs within the pore space of the sediment, while the other three forms occur where the sediment is disturbed either by regional tectonic stresses or through the stress resulting from hydrate crystal growth. The advances in hydrate sampling and imaging has led to another classification and two basic types of morphology are found: pore-filling and grain-displacing (Holland et al., 2008; Collett et al., 2008). Pore-filling morphology of gas hydrates replaces pore fluid between grains of sediment; this gas hydrate may or may not cement grains together. Grain-displacing gas hydrate does not occupy pore volume between grains and instead forces grains apart, forming veins, layers, and lenses of pure gas hydrate. Grain-displacing hydrate may cover a vast range of sizes, from thin veins of possibly only a few microns thick to nodules tens of centimeters or even meters in diameter (Holland et al., 2008).

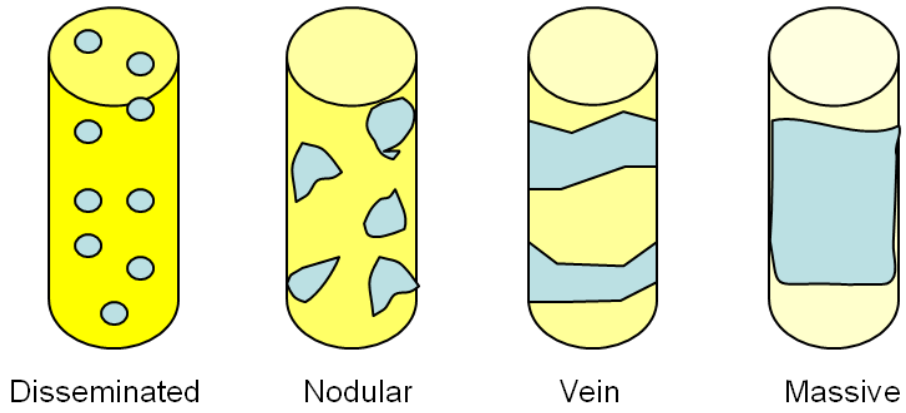

Figure 1.5: Four types of natural gas hydrate deposition in sediments (redraw from Malone, 1985).

The impact of gas hydrate formation on the physical properties of sediment depends on its spatial distribution. Three main formation habits at the pore scale are identified (Figure 1.6):

(1) **Pore-filling—**hydrate forms within the pore space and is part of the pore fluid, which primarily contributes to the bulk stiffness of pore fluid and has no effect on the stiffness of sediment (Helgerud et al., 1999; Ecker, 2001; Waite et al., 2004).

(2) **Load-bearing—** hydrate connects sediment grains and becomes a load-bearing component of the frame, which decreases the porosity and increases the shear stiffness of sediment (Helgerud et al., 1999).

(3) **Cementation**—hydrate cements grain contacts acting as bond bridges between grains, which reduces the porosity and increases the stiffness of sediment skeleton.

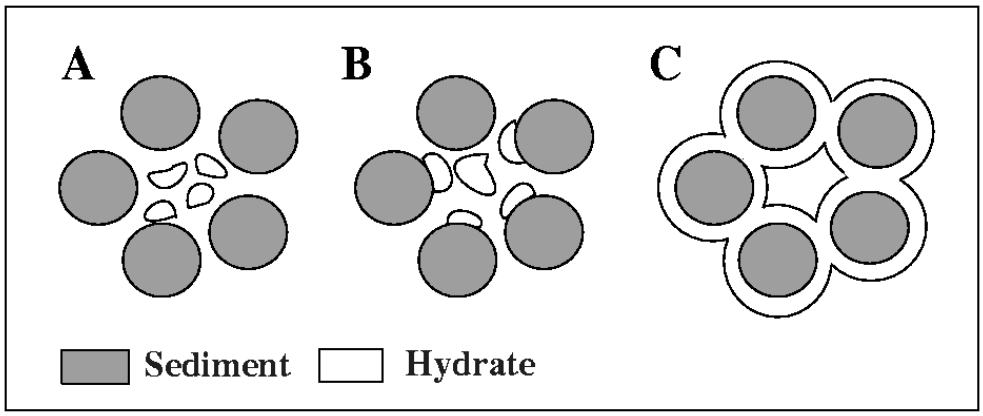

Figure 1.6: Microscopic models of gas hydrate formation: pore-filling (A), load-bearing (B), and cementation (C) (from Ecker, 2001).

1.1.4 Geophysical methods for marine gas hydrate studies

Gas hydrates in the marine sediments have commonly been inferred on the basis of seismic reflection profiles from the presence of a so-called bottom simulating reflector (BSR) that marks the base of the gas hydrate stability zone (Shipley et al., 1979). Generally, BSR is a high-amplitude reflector that approximately parallels to the seafloor with a reverse polarity, which is generated due to the strong impedance contrast between high-velocity hydrate-bearing sediments above and underlying low-velocity free gas-bearing sediments (Shipley et al., 1979; Singh et al., 1993) (Figure 1.7). Because the BSR follows a thermobaric surface rather than a structural or stratigraphic interface, it is normally observed to crosscut other reflectors (Dai et al., 2004). The presence of BSR is not the required condition for the occurrence of gas hydrates. ODP leg 164 drilled through BSRs on Blake Ridge and failed to find hydrates at locations where a BSR was observed on the seismic survey (Paull et al., 1996). Gas hydrates may also occur in regions without a BSR (Holbrook et al., 1996). Most of BSR amplitudes are due to the low velocity caused by the presence of free gas beneath gas hydrates (Singh et al., 1993; Holbrook et al., 1996; Hyndman et al., 2001; Pecher et al., 2001). If they are not accompanied by free gas, only very high hydrate concentrations produce visible amplitude anomalies in seismic data (Hornbach et al., 2003).

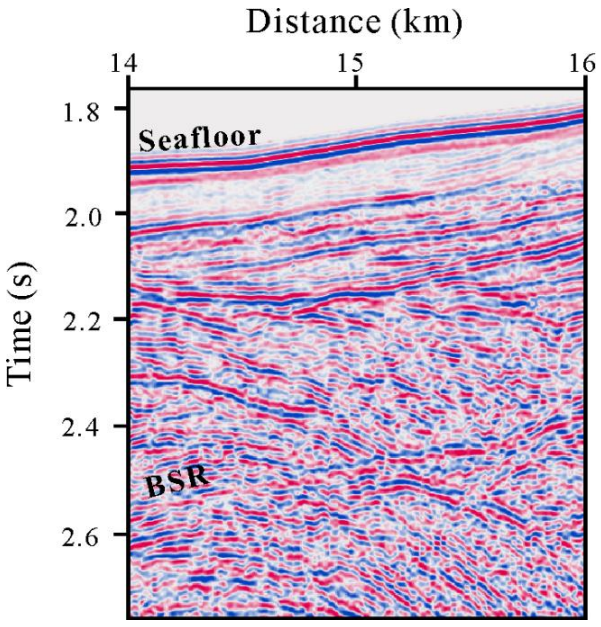

Figure 1.7: Part of seismic section of MCS line BSRstar8. Note that the BSR is relatively parallel to the seafloor and makes the base of gas hydrate stability zone. The BSR has a reverse polarity with respect to the seafloor.

It is important to recall that the BSR can be also caused by diagenesis of siliceous sediments, which occurs often at greater depth than the base of gas hydrate stability zone. The diagenesis-related BSR originates from the positive acoustic impedance contrast between silicate rich sediments of the different diagenetic stages opal A, opal CT and quartz (Kastner et al., 1977). Therefore, it shows the same polarity as the seafloor reflection, by comparison with the negative polarity associated with the hydrate-related BSR (e.g., Berndt, 2004). During burial, the pressure and temperature increases, and biogenic silica (opal-A) undergoes dissolution and reprecipitation (diagenesis) as opal-CT. This causes an increase of density and P-wave velocity and a decrease in porosity and permeability across the interface between the two forms of opal, producing an acoustic impedance contrast adequate to create a reflection with a positive polarity (e.g., Tribble et al., 1992; Nouzé et al., 2009). Temperature is a main factor controlling the Opal-A/Opal-CT transition and its ranges were estimated to be 35–50 ℃ (Hein et al., 1978) or 45–50 ℃ (Keller and Isaacs, 1985). The opal-A/opal-CT BSRs have been recognized in some areas, such as Monterey Formation in California (e.g., Isaacs, 1982), Bermuda Rise (e.g., Thein and von Rad, 1987), the Antarctic basin (e.g., Botz and Bohrmann, 1991), the Japan Sea (e.g., Kuramoto et al., 1992), Norwegian Sea (e.g., Berndt et al., 2004), the Faeroe-Shetland basin (e.g., Davies and Cartwright, 2002), New Zealand (e.g., Lynne and Campbell, 2004). Criteria for distinguishing a diagenesis-related BSR from the more common gas hydrate-related BSR have been discussed, which are mainly based on their seismic characteristics (e.g., Berndt et al., 2004; Nouzé et al., 2009; Geletti and Busetti, 2011). The most obvious difference between the two types of BSR is their apparent polarity without a short-window amplitude gain control. In addition, the depth range of the BSR and its lateral change in sub-bottom depth and lithology information can be used to distinguish the different BSRs (e.g., Berndt et al., 2004).

In addition to BSR, seismic velocities are commonly used to identify gas hydrates and provide information on the concentration and distribution of gas hydrate and free gas in sediments. Laboratory measurements show that pure methane hydrate has a P-wave velocity (V_p) of 3.65 km/s and a shear wave velocity (V_s) of 1.89 km/s (Waite et al., 2000). Poorly consolidated sediments with no gas hydrate or free gas typically present a value of 1.6-1.8 km/s for V_p and 0.3-0.8 km/s for V_s (Dash and Spence, 2001). Therefore, the presence of gas hydrates increases both the V_p and V_s. However, the effect of gas hydrates on S-wave velocity is different depending on the micro-scale distribution of gas hydrates within the sediments, i.e. as pore fluid component or cementing grain contacts. S-wave velocity increases significantly at low gas hydrate concentration if hydrates form cement around the grain particles, whereas it increases significantly only at very high hydrate concentration (higher than 40% of pore space) if hydrate fills the pore space with little grain contact (e.g., Chand et al., 2004; Yun et al., 2005). The presence of free gas (even a small amount) reduces the P-wave velocity significantly with respect to water-saturated sediments, but has nearly no effect on S-wave velocity (Domenico, 1977). Therefore, the measurement of S-wave velocity is crucial and it can help to understand the distribution of gas hydrates within the pore space and provide additional constraints in estimating hydrate concentration. The analysis of shear waves can be achieved by deploying multi-component Ocean Bottom Seismometers (OBS) on the seafloor which allows recording converted PS-wave reflections, in addition to wide-angle P-wave reflections and refractions.

Seismic attributes such as reflection strength, blanking or reduction in amplitudes, instantaneous frequency and attenuation can be used as important markers to identify gas hydrates in the absence of BSR or BSR becomes suspicious and ascertain whether a BSR is related to gas hydrates (Ojha and Sain, 2010). Compressional wave attenuation and shear wave attenuation may also prove to be indicators of gas hydrate and free gas (e.g., Lee and Collet, 2006; Rossi et al., 2007; Singhroha et al., 2016).

The common methods for velocity analysis are: semblance velocity analysis (e.g., Lee et al.,

2005), common-image gathers analysis (e.g., Tinivella et al., 2009), waveform inversion (e.g., Singh et al., 1993), travel time tomography (e.g., Lodolo et al., 2002) and amplitude versus offset analysis (e.g., Tinivella, 2002).

Since the presence of gas hydrate and free gas change the physical properties of marine sediments, such as velocities, densities and elastic modulus, geophysical techniques can make use of these anomalous physical properties to detect gas hydrate and free gas. The most common used tool is seismic investigation. Here, the main marine seismic acquisition systems (Figure 1.8) are briefly introduced, including single- and multi-channel seismic streamers, deep-towed multichannel streamers and Ocean-bottom seismometers (OBSs).

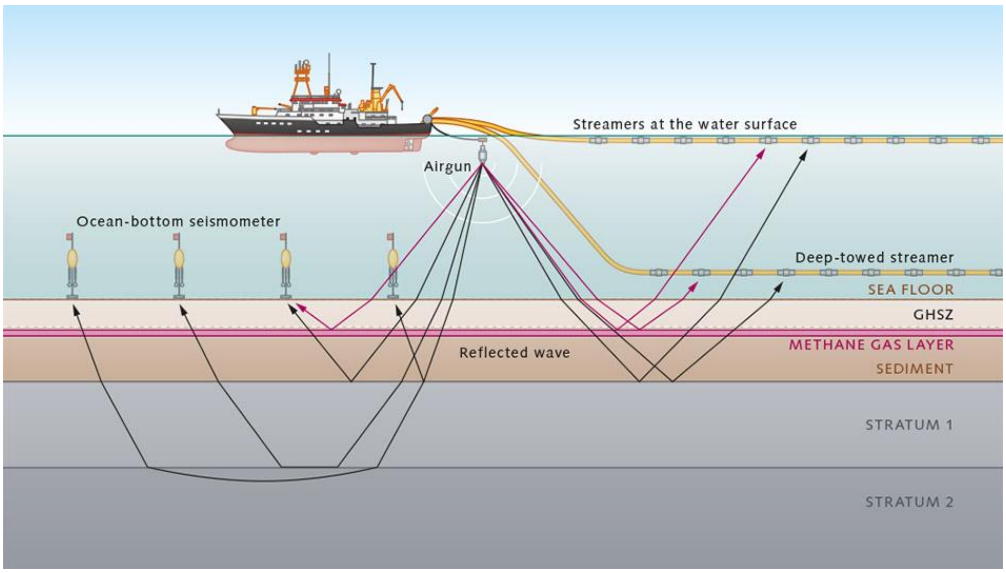

Figure 1.8: Marine seismic acquisition systems, including single- and multi-channel seismic streamer, deep-towed multichannel streamer, and Ocean-bottom seismometer (from https://worldoceanreview.com/en/wor-3/methane-hydrate/extraction/2/).

(a) Single- and multi-channel seismic streamers:

Seismic methods use airguns to produce acoustic waves that penetrate into the seabed, where they are reflected by the different layers at different strengths or refracted. Receivers mounted on a cable several kilometers long called a streamer are towed behind the ship and record the reflected waves. Single-channel seismic (SCS) data usually are acquired by a short length streamer with only

one hydrophone, which can provide structural image but no velocity information due to the lack of velocity move-out information. In multichannel seismic (MCS) data, the streamer has a longer length and numerous hydrophone groups, providing the opportunity to record long offsets and velocity-dependent move-out information.

(b) Deep-towed multichannel streamers:

To achieve a higher resolution of the seismic image, streamers can be towed through the water closer to the seabed in order to reduce the offset between receiver and target or both sources with receiver and target (Marsset et al., 2014). The advantage of this is that proximity to the bottom gives the streamers a wider-angle image of the seabed.

(c) Ocean-bottom seismometers (OBSs):

While short active length multichannel reflection seismic streamers are already capable of providing the required images, by use of mid-size multipurpose vessels they are usually not sensible enough to velocity. This gap can be closed by using ocean-bottom seismometers (OBSs) (Crutchley et al., 2016). OBSs are usually equipped with 4 component receivers, one hydrophone and three orthogonally orientated geophones. OBSs are not attached to a streamer but are planted on the sea floor, which allows greater observational depth coverage. Moreover, not only they can receive wide-angle P-wave reflections and refractions, but they can also receive converted S-waves that can provide additional constraints on velocities and distributions of gas hydrate and free gas.

1.1.5 Importance of gas hydrates

During the last few decades, much effort has been expended on the study of gas hydrates, the

main reasons are: (1) they are considered as potential energy source; (2) they may present a potential geological hazard; (3) they play a potential role in global climate change (e.g., Kvenvolden, 1988; Kvenvolden, 1998; Kennett et al., 2003; Mienert et al., 2005; Ruppel, 2011; Ruppel, 2017).

Potential energy source:

A large amount of methane stored in gas hydrates make them attractive as potential energy source in the future. Gas hydrates are especially attractive for countries with very limited conventional hydrocarbon resources that must import them at great cost. For example, Japan, which does not have any significant deposits of oil and natural gas, and is implementing sizeable projects concerning an economic production of gas hydrate. Release and production of methane from hydrate-bearing sediments are related to hydrate dissociation. Many methods have been developed for enhancing gas production. The most commonly proposed methods are thermal stimulation, depressurization, inhibitor injection and a combination of these methods (Collett, 2002).

Since gas hydrates were discovered in 1967, attempts have been made to estimate the total amount of gas hydrates on earth. The original estimates were between 10000 and 11000 GtC (2×10^{16} m^3) (MacDonald, 1990; Kvenvolden, 1998), which was more than 10 times the amount of carbon stored in gas hydrates as in the atmosphere and would exceed by far the amount of carbon stored in other fossil fuel reservoirs. The estimates of global methane amount have been decreasing over time because of improved knowledge about gas hydrate reservoir. Several independent assessments based on various observations, models, and methodology to converge on values that are mostly less than 2000 GtC sequestered in methane hydrates (e.g., the lower range of Milkov, 2004; Archer et al., 2009; Boswell and Collett, 2011; Piñero et al., 2013). Nonetheless, the estimate of hydrate resource is still huge compared with the conventional gas resources.

Geo-hazard:

Gas hydrates are considered as a geohazard due to the possible connection between hydrate dissociation and submarine sediment failures. When gas hydrate dissociates, the resulting volume and density change in the sediment can lead to local destabilization of the continental slope and result in submarine slides, collapses, and slump failures. There are many examples of this connection: surficial slides and slumps on the continental slope and rise of West Africa; slumps and collapse features on the U.S. Atlantic continental slope; large submarine slides on the Norwegian continental margin; sediment blocks on the sea floor in fjords of British Columbia; and massive bedding-plane slides and rotational slumps on the Alaskan Beaufort Sea continental margin (Kvenvolden, 1993, 1999, 2000). These submarine geohazards, caused by gas hydrate dissociation, are of immediate importance to near and offshore infrastructures. Human activities and installations in regions of gas-hydrate occurrence must take into account the presence of gas hydrate and deal with the consequences of its presence (Kvenvolden, 2000).

Climate change:

An increase in temperature, a decrease in pressure or a regional uplift may cause the dissociation of gas hydrates and release the methane into the atmosphere. Methane is very powerful greenhouse gas that can produce 26 times stronger global warming potential than carbon dioxide. The resulting enhanced greenhouse gas levels would additionally warm the atmosphere and hence maintain or reinforce hydrate dissociation. Therefore, gas hydrates have become one of the major concerns of global warming (Heimann, 2010). Some authors have documented that gas hydrate dissociation influenced significantly global climate change events in the late Quaternary period, whose effect is often used to frame how the gas hydrate reservoir may respond to future climate change (Kvenvolden, 1993; Dickens et al., 1995; Kennett et al., 2007; Reagan et al., 2007). The Clathrate Gun Hypothesis (Kennett et al., 2002) suggests that past increases in water temperatures near the

seafloor may have induced such a large-scale dissociation, with the methane spike and isotopic anomalies reflected in polar ice cores and in benthic foraminifera. This hypothesis has been challenged by other studies suggesting that methane from dissociating hydrate may never have reached the atmosphere (e.g., Kvenvolden, 1999). Alternatively it has been proposed that methane release may follow, rather than lead, climate change (Nisbet, 2002).

1.2 Gas hydrates on the South Shetland margin

The global climate change is particularly amplified in transition zones, such as the peri-Antarctic regions (Tinivella et al., 2008). So, the gas hydrate reservoir occurs offshore Antarctic Peninsula has been studied in the last 30 years and extensive geophysical dataset have been acquired.

1.2.1 Geological setting

The study area is located offshore Elephant Island in the South Shetland margin. The area extends from 60.5 ° S to 61.5 ° S and from 56 ° W to 58.5 ° W (Figure 1.9a). In this area, the continental margin shows a complex tectonic setting due to the subduction of the Antarctic and the "former Phoenix" plates beneath the South Shetland micro-continental block. Along the continental margin, a trench-accretionary prism–fore–arc basin sequence can be recognized (Maldonado et al., 1994; Kim et al. 1995). Active spreading along the Antarctic–Phoenix ridge stopped about 3.5 Ma ago (Larter and Barker, 1991), but subduction continued as a consequence of sinking and roll-back of the subducted slab coupled with extension in the Bransfield Strait marginal basin (Larter and Barker, 1991; Kim et al., 1995; Jin et al., 2002; Dietrich et al., 2004). The part of the Antarctic plate involved in the subduction process (a remnant of the Phoenix plate) is laterally bordered by two main fracture zones, the Hero (to the south) and the Shackleton (to the north), respectively. These two fracture zones intersect the continental lithosphere and their landward projections are associated

with structural and morphological variations in the overriding lithosphere (Grad et al., 1993; Kim et al., 1995; Jin et al., 2002; Loreto et al., 2006). A narrow accretionary prism has developed along the continental margin, ranging from 20 to 40 km in width. The prism is characterized by a range of deformational features, deduced by seismic data interpretation (Lodolo et al., 2002): reverse and thrust faults mainly affect the frontal part of the prism; extensional faults further from the trench are oriented sub-parallel to the continental shelf; a strike–slip fault has been interpreted as being related to the Shackleton Fracture Zone. This fault crosses the entire continental slope splitting the margin in two parts with different characteristics. To the northeast of the fault, a strong and continuous BSR is detected, while to the southwest it becomes weak and discontinuous. Small mid-slope basins are common within the prism, often bounded by extensional faults that locally reach the seafloor (Lodolo et al., 2002).

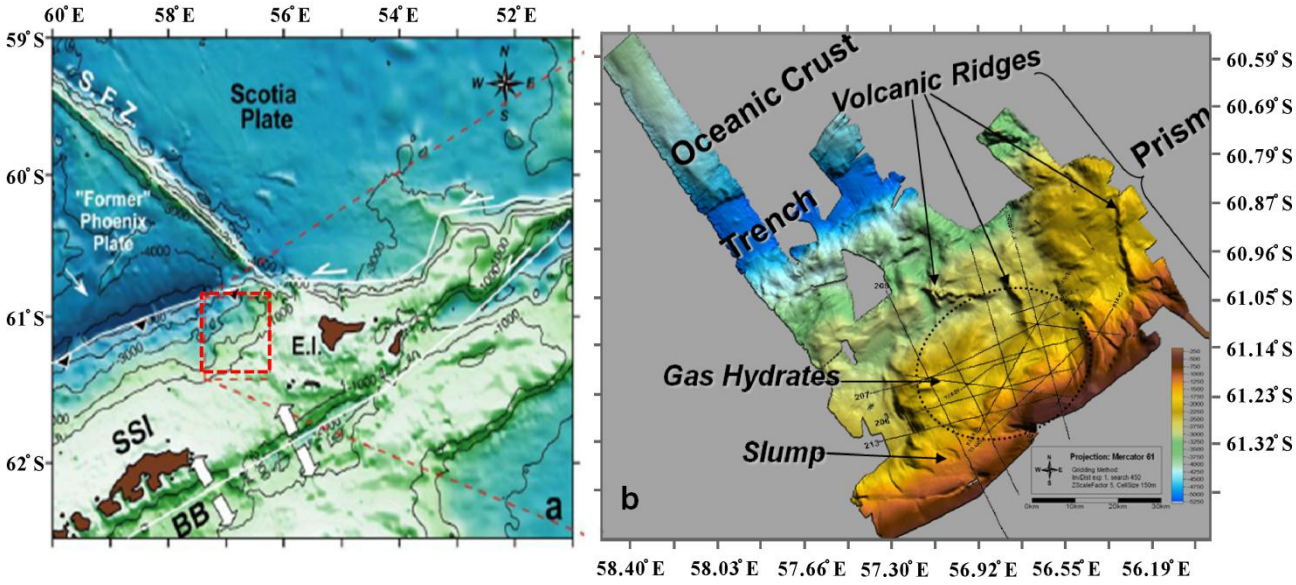

Figure 1.9: (a) Shaded relief of bathymetric data derived from gravimetric data. The white thick arrows indicate a schematic NW-SE extension affecting the Bransfield Strait Basin. The subduction direction of the "Former Phoenix Plate" is indicated by a white thin arrow. The transform movements are reported with double white thin arrows. The dashed rectangle indicates extent of detailed bathymetric data shown on the right. E.I. Elephant Island; SSI: South Shetland Islands; SFZ: Shackleton Fracture Zone. (b) Shaded relief of the high resolution morpho-bathymetry image. The black solid lines indicate the location of seismic lines acquired in this area (modified after Loreto and Tinivella, 2012).

1.2.2 Previous geophysical studies

The presence of a strong BSR across the accretionary prism of the South Shetland margin was firstly identified on two multichannel seismic reflection profiles acquired during the Italian Antarctic cruise of 1989–1990, onboard R/V OGS Explora, which is the first evidence of gas hydrate reservoir present in the Antarctic Peninsula region (Lodolo et al., 1993). Tinivella et al. (1998) applied reflection tomography techniques to the two multichannel seismic profiles and obtained a local velocity field associated with gas hydrate and free gas layers. Their analysis show that the BSR is a well defined, high-amplitude, reverse-polarity and nearly continuous reflector located between 500 and 900 ms below the seafloor in the water depths ranging from 1000 to 4600 m; a normal polarity reflector that locally present about 80 ms below the BSR is identified as the base of free gas layer (BGR), and the thickness of free gas layer is estimated about 50 m. The area has since then studied with an extensive range of geophysical surveys. About 750 km of intermediate-resolution multichannel and single-channel seismic reflection profiles were acquired during the cruise of 1996–1997 by the R/V OGS Explora, and one OBS was also deployed along a seismic profile where the BSR signature was particularly evident (Tinivella and Accaino, 2000; Lodolo et al., 2002). During the austral summer of 2003–2004, new geophysical data were acquired in this area, including multibeam bathymetry, MCS profiles, OBSs, chirp and sediment gravity cores (Tinivella et al., 2008).

The available data were analyzed by several authors to characterize the gas hydrate systems. Lodolo et al. (2002) interpreted the entire multichannel seismic data acquired in 1997 and they reported that BSR is widespread at water depths ranging from 1000 to 4800 m and its occurrence appears to be controlled by the geological structure of the margin. The P-wave velocity field obtained from reflection tomography inversion was used to map the BSR and quantify the amount of gas stored in gas hydrate and free gas layers, the results show that BSR occurs at depths varying between 1700 and 2800 m, following and exaggerating the wedge topography and showing

increasing depths seaward; the potential of the margin as a reservoir is about 2.36 $\times 10^{12}$ m^3 of natural gas. Tinivella et al. (2002) analyzed parts of seismic profiles in three different geological domains (the continental shelf, the accretionary prism and the trench). The P-wave velocity filed obtained from travel time inversion indicates an obviously higher value (up to 1000 m/s at 600-700 m below seafloor) in the continental shelf sediments than that of the other two geological domains, which is due to sediment overcompaction and erosion induced by the wax and waning of a grounded ice sheet. The average concentration of gas hydrate and free gas is 6.0% $\pm$1.2% and 4.3% $\pm$0.3% of volume. In order to obtain a more reliable estimation of gas content in this study area, Tinivella et al. (2009) performed the pre-stack depth migration and tomographic analysis of common image gathers (CIGs) to produce a detailed and regional velocity field and obtain information about the hydrate and free gas thickness. They also underlined that the presence of biogenic silica or structural elements can lead to an over- or underestimate for the gas phase amount. Loreto et al. (2011) applied the same approach to achieve the velocity fields and a 3D model of gas hydrate concentration from the seafloor to the BSR. The estimated amount of gas hydrate can vary in a range of $12 \times 10^9 - 20 \times 10^9$ m^3. Considering that 1 m^3 of gas hydrate corresponds to 140 m^3 of free gas in standard conditions, the total free gas trapped in this reservoir ranges between 1.68 $\times 10^{12}$ and 2.8 $\times 10^{12}$ m^3. Based on the available velocity fields, Loreto and Tinivella (2012) obtained information about porosity variation due to hydrate presence and analyzed the relationship between gas hydrate distribution and geological features. They observed that the hydrate porosity increases toward the limbs of anticline, and synclines favour the hydrate accumulation above the BSR, while the anticlines favour the free gas accumulation below the BSR, which is supported by micro-fracturing model.

Previous studies mentioned above are all based on the analysis of multichannel seismic data. Only one OBS (see Figure 2.1 for the location) deployed during the 1996/97 cruise was analyzed by Tinivella and Accaino (2000) to obtain P-wave velocity structure and Poisson's ratio in marine sediments. The P-wave velocity model determined by the travel time inversion of reflections from

MCS and OBS data shows that the high velocity layer (2.0–2.3 km/s) above the BSR is related to the presence of gas hydrate and the low velocity layer (1.2–1.5 km/s with a variable thickness of 100–400 m) below the BSR is associated with the presence of free gas, which was confirmed by the good result of pre-stack depth migration. The real base of free gas layer is identified by modeling of a refractor from OBS data. The Poisson's ratio obtained by travel time inversion of shear wave arrivals in the horizontal components of OBS data shows a good agreement with that obtained from AVO analysis of MCS data.

The new dataset acquired during the 2003/04 cruise was interpreted by Tinivella et al. (2008) and main results are reported: (1) the bathymetric map provided the evidences of mud volcanoes, collapse troughs and slides that border the gas hydrate reservoir discovered in 1996–1997; (2) five main mud volcano ridges have been recognized; (3) fluid analyses performed on the two gravity cores revealed the presence of several hydrocarbon gases, i.e., methane, ethane, propane, butane, pentane and hexane; the hydrocarbons possibly indicate the existence of deeper reserves.

1.3 Objectives and outline of thesis

In the South Shetland margin, the occurrence of a potential gas hydrate reservoir has been demonstrated from the analysis of geophysical data acquired during three Italian Antarctic cruises in 1989/1990,1996/1997 and 2003/2004. Long-term ocean warming could induce the dissociation of gas hydrates in this area and the release of methane may contribute to climate change (e.g., Mar ń-Moreno et al., 2016). Therefore, it is very important to enhance existing knowledge on the gas hydrate reservoir located in the South Shetland margin. OBS data have been used successfully in the characterization of gas hydrate reservoir by combined analysis of P- and S-waves, and the importance of S-wave velocity has been pointed out (e.g., Kumar et al., 2007; Dash and Spence, 2011). In this study area, only few studies were performed to characterize gas hydrate reservoir utilizing OBS data. For example, in the recent 20 years, only one OBS deployed during the 1996/97

cruise was analyzed by Tinivella and Accaino (2000). In order to better characterize and improve the knowledge of gas hydrate systems, we performed analysis on the OBS data acquired in 2003/2004 cruise. The detailed objectives of this thesis are:

(a) to determine detailed P- and S-wave velocity fields in this region;

(b) to obtain a reliable estimate of distribution and concentration of gas hydrate and free gas within the sediments;

(c) to investigate the change of petrophysical properties in the gas hydrate reservoir.

Chapter 2 describes the seismic data used in this thesis and the processing applied to the data. The main processing methods and steps performed on the MCS and OBS data are presented in this chapter, including the preprocessing of OBS data (OBS relocation and rotation of horizontal components).

Chapter 3 presents the application of seismic traveltime inversion to the MCS and OBS data. The background theory of traveltime inversion is firstly introduced, and then P- and S-wave velocity modeling procedures and velocity structures are reported. Finally, the errors in the velocity fields are analyzed and a modified velocity model is obtained.

In Chapter 4, the main theoretical models for estimation of gas-phase concentrations are reviewed, and the velocity fields obtained from traveltime inversion are used to estimate the concentrations of gas hydrate and free gas based on a modified Biot-Geerstma-Smit theory.

In Chapters 5 and 6, the main results are discussed and the conclusions of this study are summarized.

Chapter 2

Seismic data and processing

2.1 Data acquisition

In this study area, the available geophysical data were acquired during three Italian Antarctic cruises of 1989/90, 1996/1997 and 2003/2004 onboard of the R/V OGS Explora, in the frame of projects supported by the Italian National Antarctic Program (PNRA). During the curies, more than 1,000 km of single-channel and multichannel seismic lines were acquired. A 3000-m-long streamer with 120 channels was used during the first two cruises, while the seismic source was two arrays of 15 air-guns (total volume of 45 L) in the first cruise and two generator-injector (GI) guns (total volume of 3.5 L) in the second cruise. An OBS station was also deployed along a seismic profile where the BSR signature was particularly evident in the second cruise (MCS line I97206, see Figure 2.1).

The data used in this thesis were acquired during the austral summer of 2003-2004, focused on the continental slope where the BSR is strong that identified during the second cruise. The main target of this cruise was to verify the existence of a potential gas hydrate reservoir and to reconstruct the tectonic setting of the South Shetland margin. Two OBS stations were deployed along the MCS line BSRstar8 (Figure 2.1). The seismic source was two GI guns with a total volume of 3.5 L, which were towed at a water depth of 8 m and fired every 50 m. The OBS station consists of a hydrophone and a three-component geophone. Data were recorded up to 20 s with a sampling interval of 2 ms. The MCS line BSRstar8 was recorded simultaneously by an acquisition system consisted of a 600-m-long, 48-channel solid-state streamer, coupled to a 48-channel OYO DAS recording unit. The sampling interval of MCS data was 1 ms, and the record length was 8 s two-way traveltime. During this cruise, high resolution morpho-bathymetry and chirp sub-bottom profile data

were also acquired. The multibeam bathymetric data were collected using an Ocean Depth Multibeam Echo Sounder System (Reson Seabat 8150), which Reson multibeam echo sounding system is characterized by nominal depth ranging between 0.1 and 15 km, 234 beams and nominal frequency of 12 kHz. The chirp sub-bottom profile data were acquired by means of a Benthos CAP-6600 with a sweep of 7 kHz.

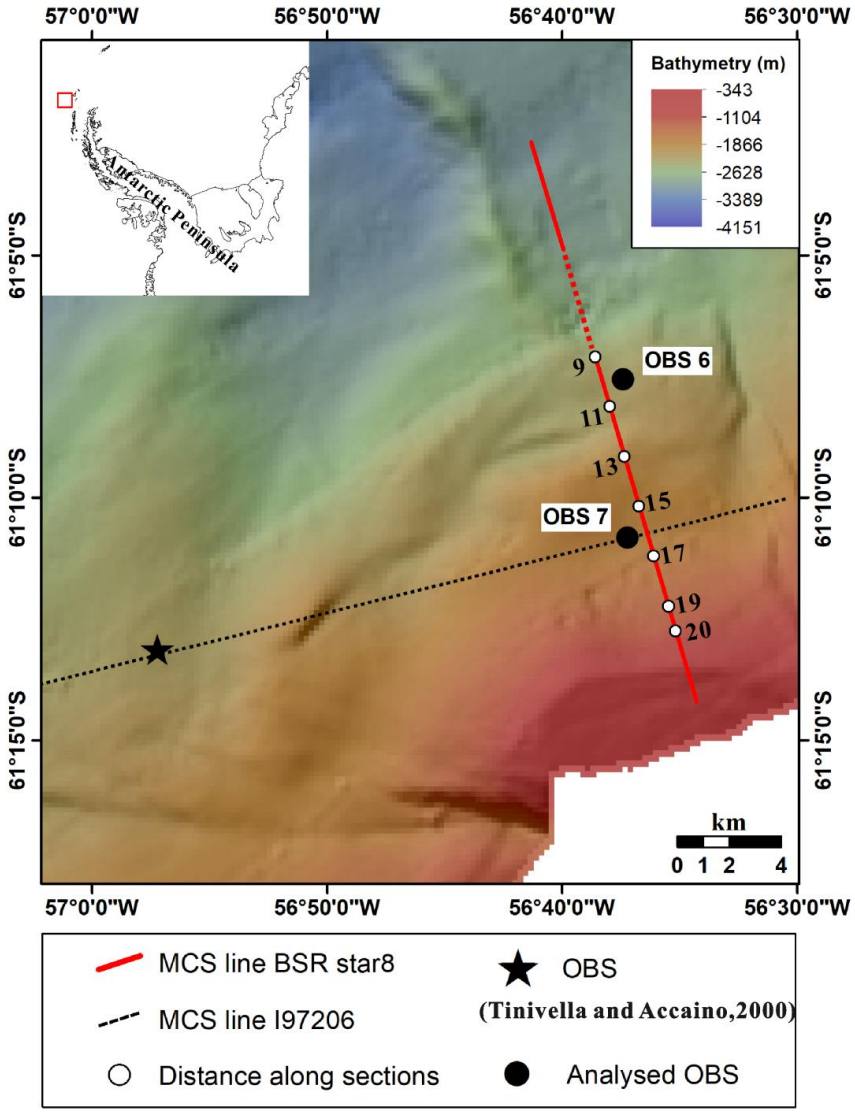

Figure 2.1: Bathymetric map of the study area (modified after Loreto et al., 2011), indicating the locations of seismic lines and OBSs. The black circles indicate the positions of OBSs. The red line indicates the MCS line shown in Figure 2.4; red dotted line indicates the gap for MCS line; the white circles and numbers along it show the corresponding distances along sections. The star and dashed line mark the OBS and seismic line analyzed in the study by Tinivella and Accaino (2000).

2.2 MCS data processing

As mentioned in section 2.1, the MCS reflection data was recorded by a 600 m long streamer with 48 channels and hydrophone group interval of 12.5 m. The shot point interval was 50 m; the CDP spacing is 6.25 m and the fold coverage is 6. Data processing was performed using the Seismic Unix (SU) package, a free software developed by the Center for Wave Phenomena (CWP) at Colorado School of Mines (Cohen et al., 2008). To obtain a seismic image, conventional seismic processing was performed to the MCS line BSRstar8. The main processing steps are summarized in Figure 2.2. Firstly, seismic data in SEGY format were converted to SU format. The next step was to set geometry. The water velocity was estimated by direct wave analysis, and the minimum offset was calculated according to direct wave and water velocity. Then geometry was set according to offset, source-receiver and common midpoint (CMP) coordinates. A trace editing was applied to remove very noisy traces. In order to attenuate noise and recover the true amplitudes of data, a spherical divergence amplitude correction and a band-pass filter (10-60 Hz) and gain were performed. Afterward, in order to improve temporal resolution and yield a representation of subsurface reflectivity, we applied a spiking deconvolution. The standard stacking velocity analysis was not performed on this MCS line because the short streamer did not provide enough move-out information, so the velocity derived from long steamer data analysis was used for the NMO correction and stack. On the post-stack data, we applied an FX deconvolution to attenuate random noise, a time-variant band-pass filter and a time-variant trace mixing for enhancing identified signals, defining a lateral window of 3 traces weighted by a symmetrical weighting function towards the central trace on the stacked data. Finally, a Kirchhoff post-stack time migration was applied. Figure 2.3 shows an example of shot gather before and after processing. The final migrated section shows a remarkable high-amplitude BSR at a two-way time of about 550-650 ms below the seafloor (Figure 2.4).

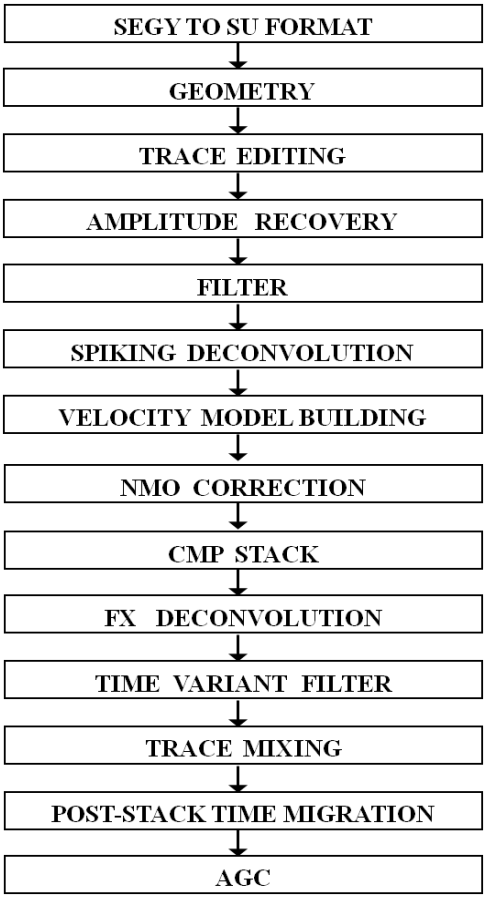

Figure 2.2: Processing sequence flow.

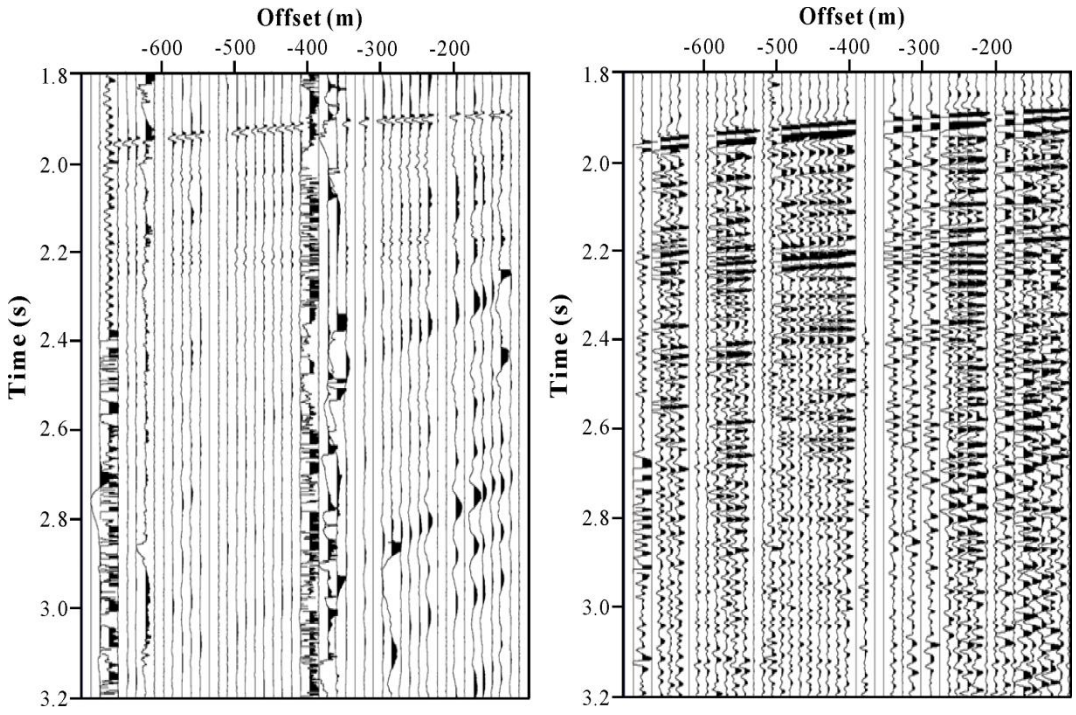

Figure 2.3: Example of one shot gather before (left) and after (right) processing.

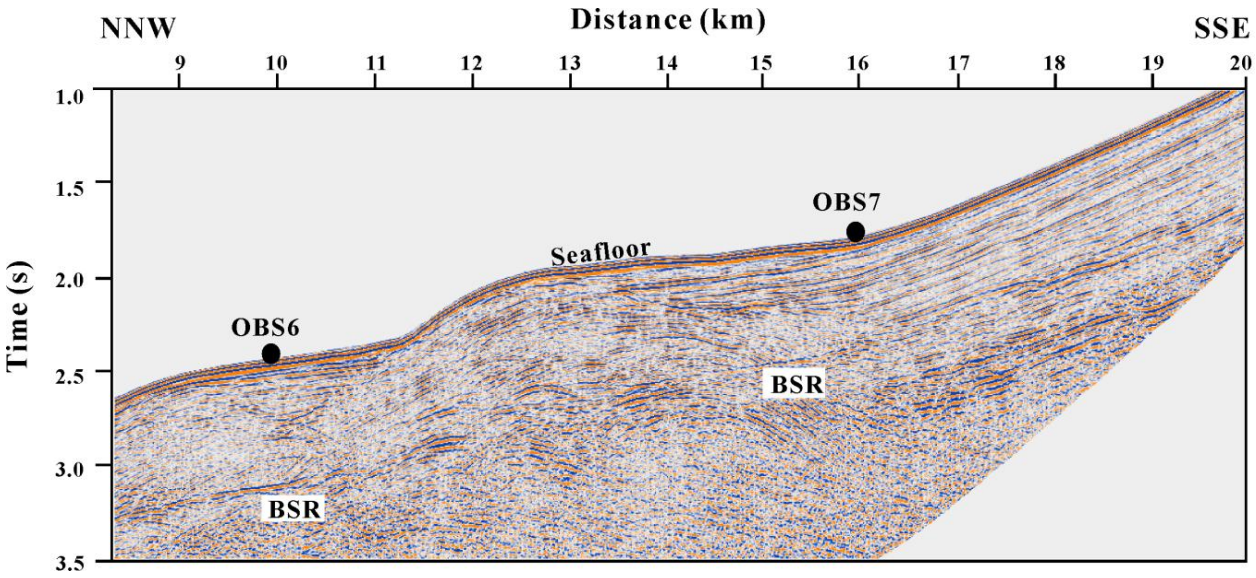

Figure 2.4: Time migrated section of part of MCS line BSRstar8. The solid circles indicate the OBS locations projected on the MCS line.

2.3 OBS data processing

2.3.1 OBS relocation

In OBS experiments, the deployment location of an OBS on the sea surface is accurately known from the differential Global Positioning System (GPS) of the ship. However, its actual location on the seafloor is not well known, because it can drift several hundreds of meters from the deployed position when sinking to the seafloor depending on the water depths and the water currents. Therefore, the first step we need to perform is the OBS relocation. Generally, the travel times of direct arrivals are used to relocate the OBS based on inversion methods. The OBS relocation problem is an inverse problem in which the objective is to find the OBS location on the seafloor and a time correction that minimize the error between the observed and calculated travel times of the direct arrivals through the water column.

For OBS 6 and OBS 7, there is only one seismic shot line and no constraint in the direction perpendicular to the shot line. In order to obtain a relatively precise OBS location, bathymetric data

were used to constrain the water depth. The bathymetric data has been calibrated using the velocity profile in the water column reconstructed from the conducibility–temperature–density (CTD) data. The size of a bathymetric grid is 200 × 200 m. Assuming the OBS is located somewhere on the bathymetric grid nodes around the deployed position, for the given grid, the distance to shot points is calculated and the theoretical travel times of direct wave are then calculated using a constant water velocity. The residuals between calculated and observed travel times of direct wave are then summed over all shots for that OBS. The grid node with the minimum root-mean-square (RMS) of residuals is the inverted location of the OBS. The grid area for global searching the location of each OBS is about 5 × 5 km. The travel time of direct arrival was picked on the hydrophone component that no filtering was performed. The values of relocated coordinate and water depth are shown in Table 2.1 and the final positions are shown in Figure 2.5. The Mercator projection with standard parallel equal to 61°S and spheroid WGS84 was adopted. The relocation result showed that both OBSs drifted about 750 m away perpendicular to the shot line, in a water depth of 1790 m and 1320 m respectively. This is likely caused by strong seawater currents. Figures 2.6 and 2.7 show the fit between calculated and observed travel times and the travel time residuals. An RMS value of 8 ms and 20 ms was obtained for OBS 6 and OBS 7, respectively.

Table 2.1 Deployed and relocated coordinates of OBSs

OBS	Deployed Position			Relocated Position		
	X (m)	Y (m)	Z(m)	X (m)	Y (m)	Z(m)
6	-3064427	-4188662	1810	-3063745	-4188510	1790
7	-3062930	-4194462	1328	-3063585	-4194612	1320

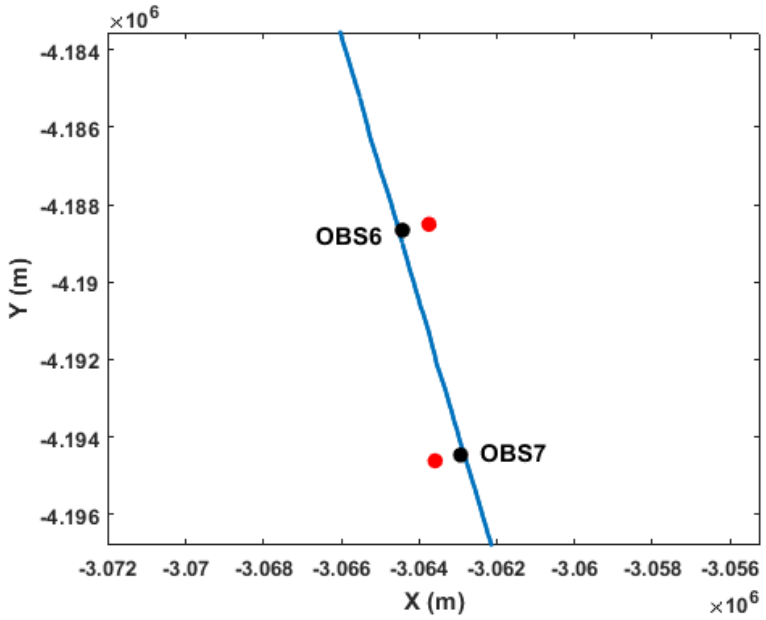

Figure 2.5: Results of OBS relocation. Black circles represent deployed positions while red circles represent relocated positions. The shot line of OBSs is marked as a blue line.

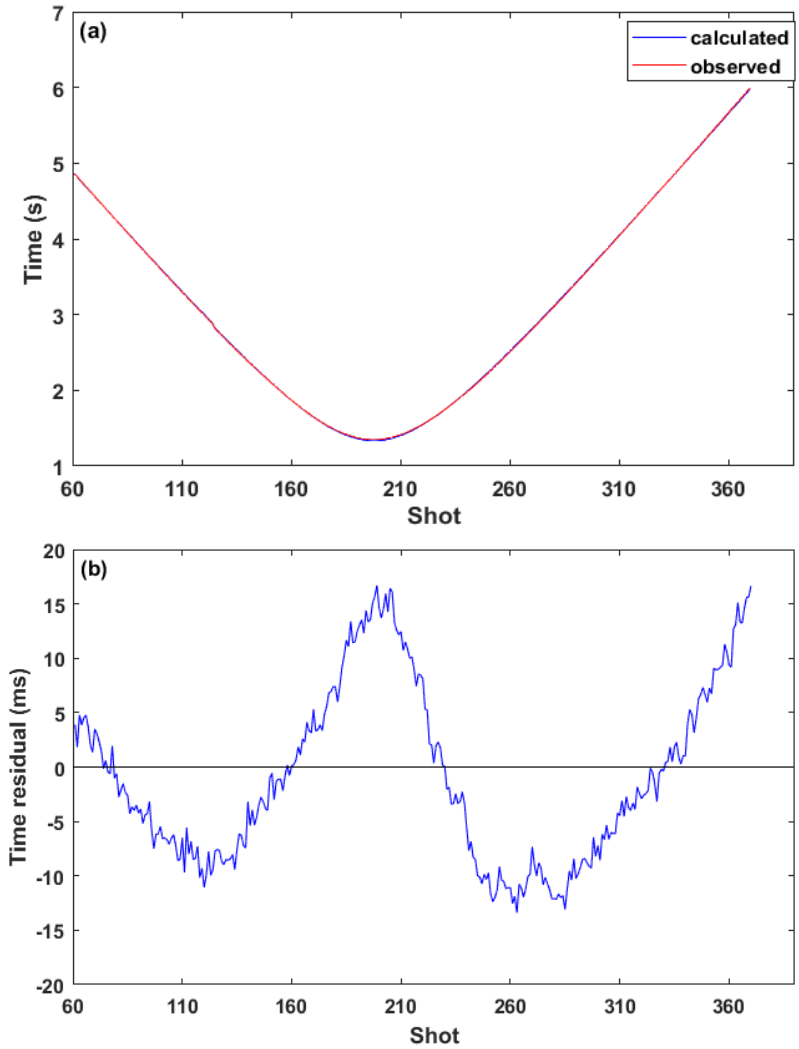

Figure 2.6: The fit between calculated (blue line) and observed (red line) travel times (a) and the time residuals (b) for OBS 6.

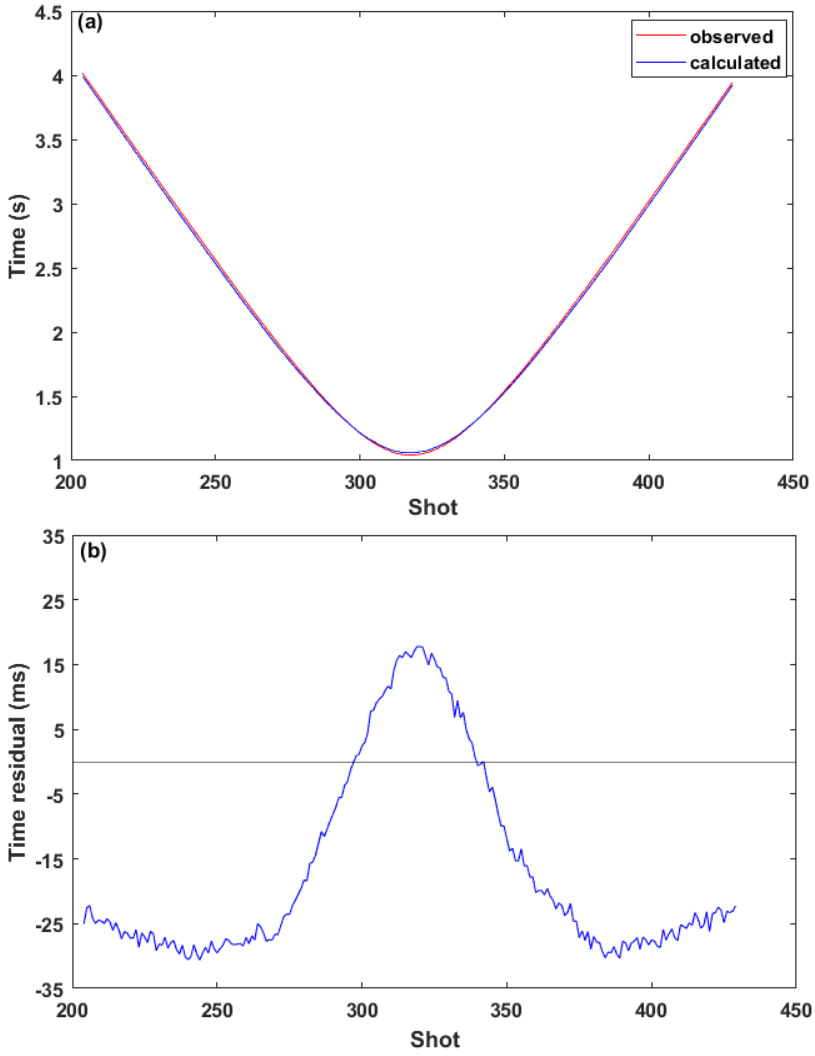

Figure 2.7: The fit between calculated (blue line) and observed (red line) travel times (a) and the time residuals (b) for OBS 7.

2.3.2 Processing of the hydrophone and vertical components

Each component of OBSs was recorded up to 20 s with a sampling interval of 2 ms, and the maximum offset is about 13 km in OBS 6 and 16 km in OBS 7, including wide-angle reflections and refractions. We compared the hydrophone component and the vertical component in order to identify events. The data in vertical component showed prominent ringing and obscured the primary reflections due to the effect of coupling between the instrument and the seafloor, while the data in hydrophone component did not because it was located within the water column. Figure 2.8 shows a data example from OBS 7. A spherical divergence amplitude correction and a 10-100 Hz band-pass

filter were applied to both components to improve the signal to noise ratio and enhance the phase identification. In order to attenuate the ringing noises, a predictive deconvolution with 160 ms operator length and 25 ms lag was applied to the vertical component, followed by a filter. However, the deconvolution was not very successful, and the ringing was still visible on the vertical component (Figure 2.8d). Therefore, the hydrophone component was chosen for event identification and picking of arrival times. The processed hydrophone component clearly shows the reflections (Figure 2.8c).

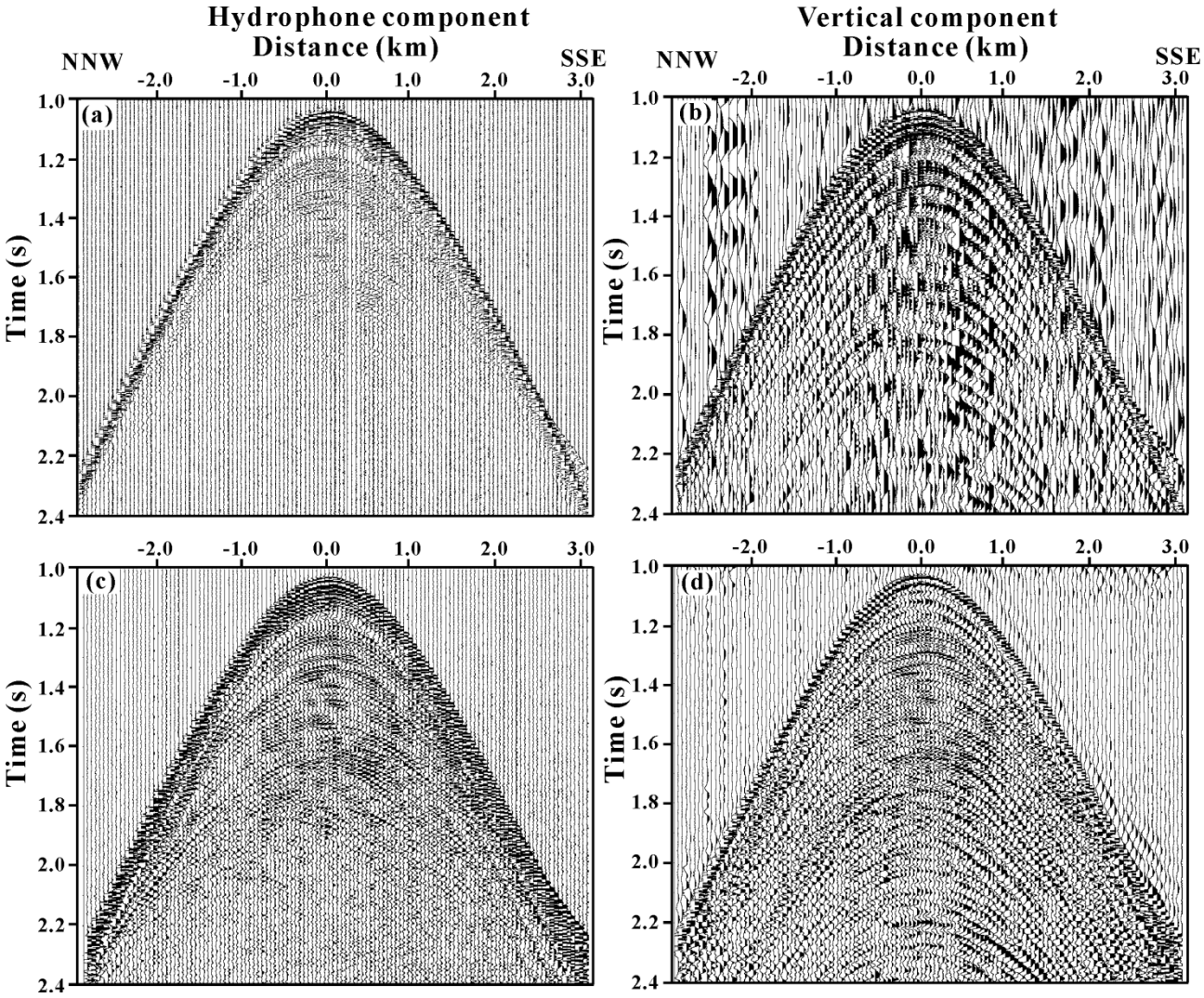

Figure 2.8: Data example from OBS 7. The left panels show raw (a) and processed data (c) from hydrophone component; the right panels show raw data (b) and processed data (d) from vertical component.

2.3.3 Processing of the horizontal components

The geophone casing was gimbaled so that the vertical component was known to be truly vertical on the seafloor. However, the free fall of OBS through water column led to the orientation of two horizontal components on the seafloor was unknown and both the two horizontal components record S-waves. So we need to determine the orientation of two horizontal components and perform rotation before further processing. A hodogram analysis (particle motion plot) is the commonly used method (Kumar, 2005). Figure 2.9 shows an example of hodogram analysis for one trace of OBS 7, where the particle motions of three components were plotted on a 2D plane. Firstly, we identified S-wave arrival by using particle motion plots between vertical (Z) and horizontal components (H1 and H2). The S-wave arrival can be identified if the energy is mainly transversal (Figures 2.9a and 2.9b). On the basis of the S-wave arrival, we plotted the particle motion of two horizontal components to estimate the rotation angle. The angle was calculated by fitting a line to the hodogram of two horizontal components (Figure 2.9c). And then the average orientation angle over all the shots was used to rotate the two horizontal components into inline and crossline components (Figure 2.9d). In this example, the linear trend gives an angle of 40^o; so the inline and crossline components were obtained by rotation of H1 towards H2 by 40^o using a simple matrix (Equation 2.1). Figure 2.10 shows the horizontal components of OBS 7 before (a) and after rotation. After rotation, the inline component contained much more energy than the crossline component, and this can facilitate the identification and picking of S-wave arrivals. The seismic processing performed on the inline component included: amplitude correction, predictive deconvolution (180 ms operator length and 50 ms lag) and band-pass filtering (14-100 Hz).

$$\begin{bmatrix} inline \\ crossline \end{bmatrix} = \begin{bmatrix} \cos\theta & \sin\theta \\ -\sin\theta & \cos\theta \end{bmatrix} \begin{bmatrix} H_1 \\ H_2 \end{bmatrix} \tag{2.1}$$

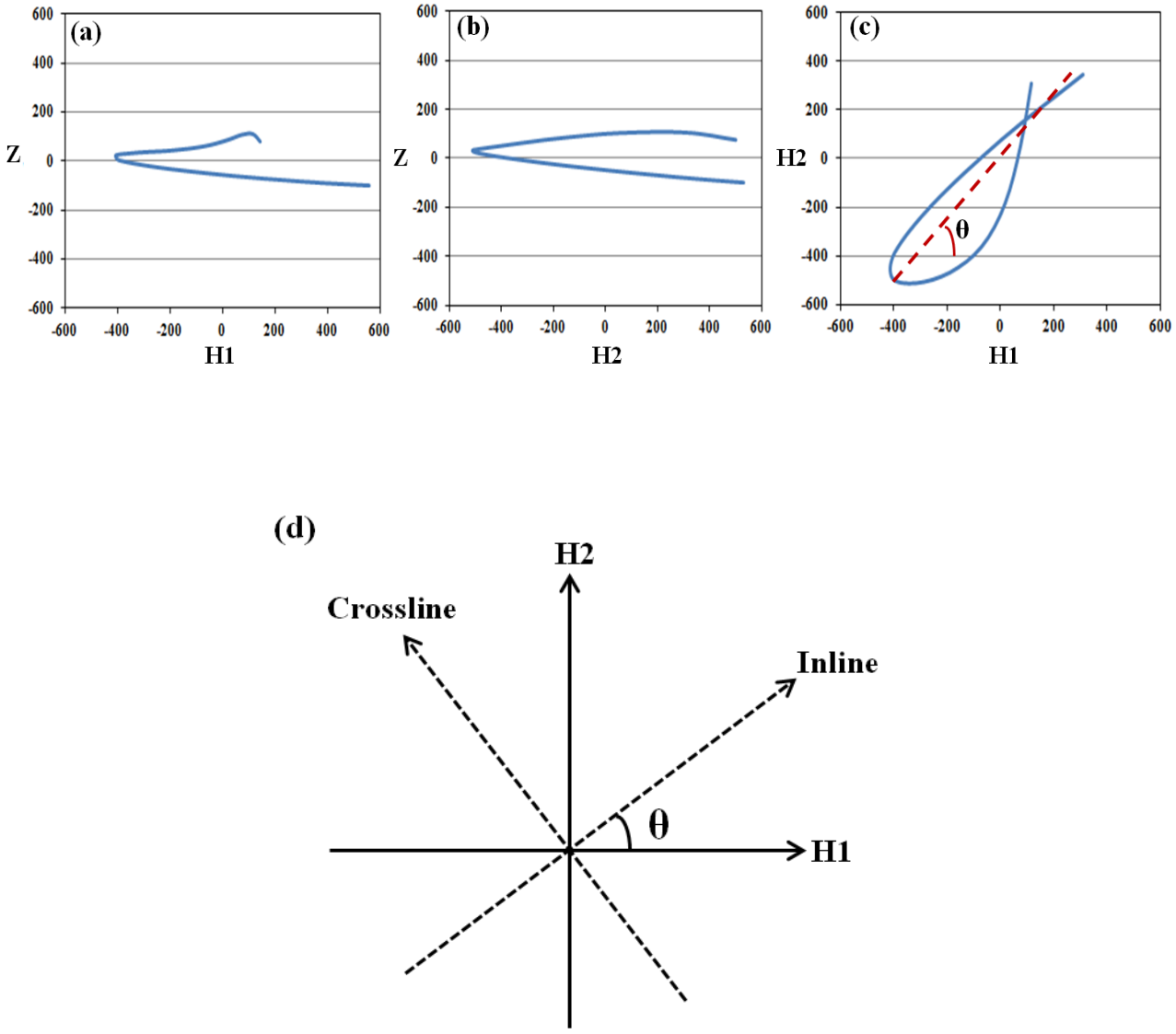

Figure 2.9: An example of hodogram analysis. (a) and (b) particle motion plots of vertical and horizontal components, (c) particle motion plot of two horizontal components, (d) rotation angle determined from the linear trend in (c) (Z: vertical component; H1 and H2: two horizontal components; θ: rotation angle).

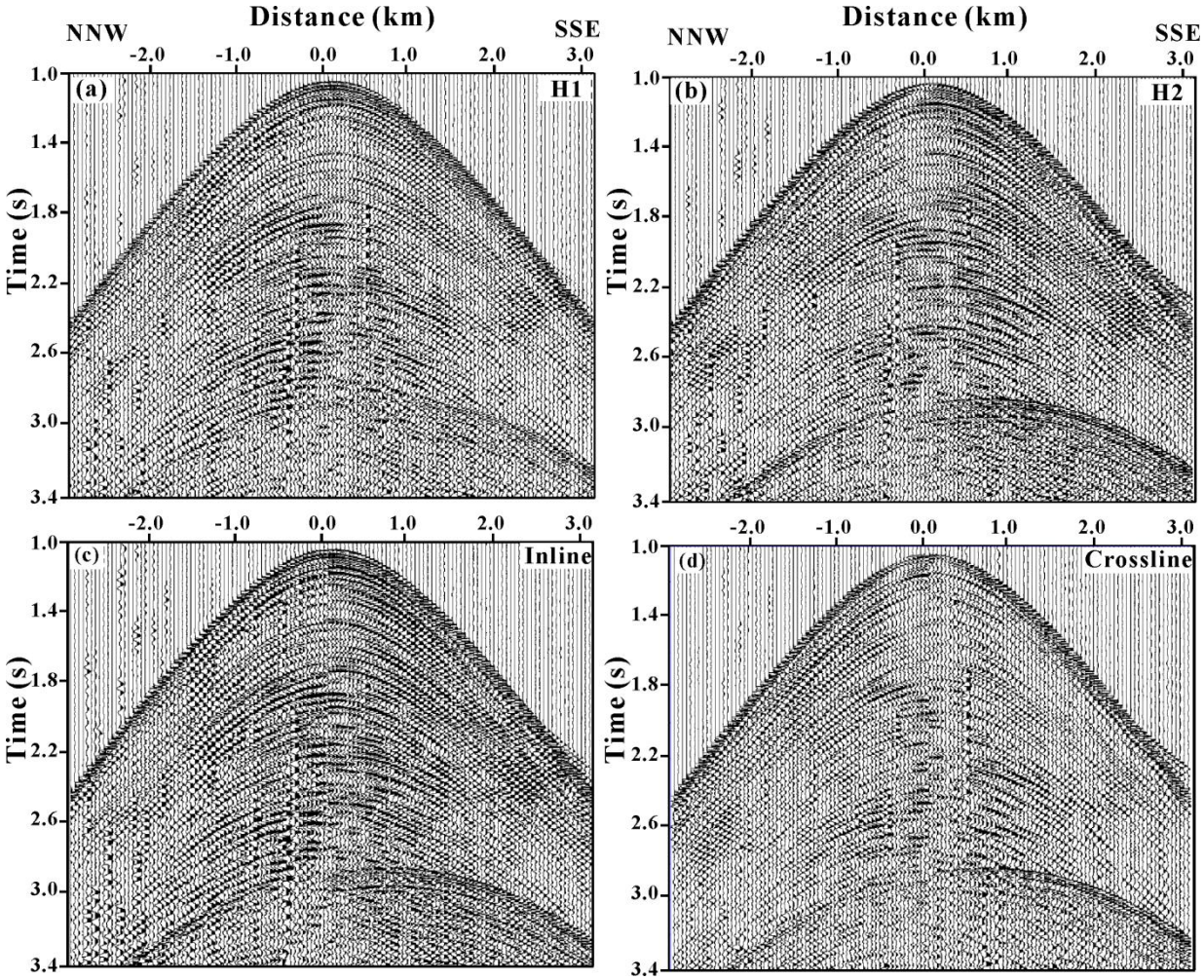

Figure 2.10: Rotation of horizontal components of OBS 7. Two horizontal components (a, b) are rotated into inline (c) and crossline components (d).

2.4 Summary

Wide-angle OBS and coincident MCS data were collected during the austral summer of 2003–2004. A standard seismic processing was applied to the MCS data and a time migrated section was obtained. The MCS data can provide a basis for building the starting model in the traveltime inversion. The exact locations of OBS on the seafloor were determined by using the arrival times of direct waves while the water depth is known from bathymetric data. The orientation of two horizontal components was evaluated based on hodogram analysis. The hydrophone and inline components were chosen for event identification and picking.

Chapter 3

Seismic traveltime inversion

3.1 Introduction

Seismic traveltime inversion involves determining the velocity structure of the subsurface by using travel time delays between source events and receivers arrivals. It has been successfully applied in various studies of earth structures ranging from the crust to the whole earth (e.g., Zelt et al., 1996; van der Hilst et al., 1997). It is the most popular technique for imaging subsurface structure at all scales.

In this study, the traveltime inversion algorithm of Zelt and Smith (1992) was used to determine both compressional and shear velocity models from the analysis of OBS/MCS data. This algorithm is widely used for traveltime inversion on wide-angle reflection and refraction data (e.g., Korenaga et al., 1997; Dash and Spence, 2011). In this chapter, the theoretical background of the traveltime inversion is firstly described, and then the application to the seismic data acquired in the 2003/2004 survey is presented.

3.2 Theoretical background

The steps required in the tomographic reconstruction of velocity field can be defined as follows:

1. **Model parametrization:** The seismic structure of the region under study is defined in terms of a finite number of model parameters. An initial estimate of model parameter values is required.
2. **Forward modeling:** Traveltimes are calculated using the source-receiver geometry and give a set of values for the model parameters.

3. **Inversion:** Model parameter values are updated to minimize the misfit between the observed data and the data calculated from the model parameters.

3.2.1 Model parameterization

The model is parameterized into a layered, irregular network of blocks to represent velocity structure. Layer boundaries are described by a set of one or more arbitrarily spaced nodes interpolated linearly. Within each layer, velocity nodes are specified on the upper and lower boundaries, the number and spacing of which may vary. An example of model parametrization is illustrated in Figure 3.1. Layer pinchouts and isolated bodies can also be included by reducing layer thickness to zero. To facilitate velocity interpolation, each layer is divided laterally into trapezoidal blocks separated by vertical boundaries, which occur at each upper and lower boundary node and velocity node. The velocity within each trapezoid is interpolated using the velocity values at the four corners so that the velocity within each layer varies linearly between the upper and lower boundaries in the vertical direction, and linearly along the upper and lower boundaries between nodes. Therefore, horizontal as well as vertical velocity gradients may exist within a trapezoid. Layer boundaries may or may not represent velocity discontinuities (Zelt and Smith, 1992).

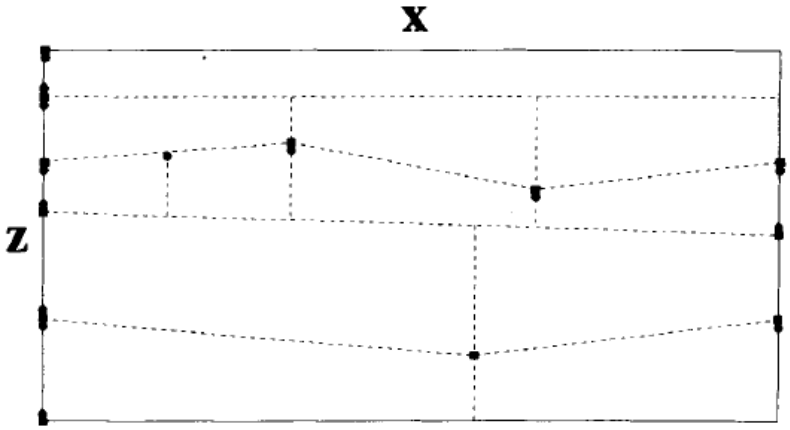

Figure 3.1: An example of velocity model parametrization. The five-layer model is divided into 12 trapezoidal blocks separated by vertical boundaries (from Zelt and Smith, 1992).

3.2.2 Forward modeling

Forward modeling involves the calculation of traveltimes between known endpoints through a given velocity structure. Two-dimensional ray tracing through a starting velocity model is performed and seismic traveltimes are calculated. The starting velocity model can be constructed from the velocity analysis of MCS data, or from the analysis of sonic-logs, or from previous model results. As the model can be rough, an appropriate starting model is necessary for rapid convergence and also for the overall ability of the inversion to converge to a reasonable final model. Rays are traced through the model used zero-order asymptotic ray theory by solving the ray tracing equations numerically (Cerveny et al., 1977) using a Runge Kutta method. At the intersection of a ray with a layer boundary, Snell's law is applied. The traveltime (t) between a source and a receiver along a ray path l is given in the integral form:

$$T = \int \frac{1}{v} dl = \int s \, dl \tag{3.1}$$

where dl is differential path length and v is velocity.

The travel times correspond to any ray paths which can be traced through the model, being either first or later arrivals. The partial derivatives of travel time with respect to those model parameters selected for adjustment are calculated analytically during ray tracing; these parameters include velocities and the vertical position of boundary nodes. The travel time residuals with respect to the observed data are also calculated.

The algorithm uses three different types of rays for the ray-tracing approach (Figure 3.2): (1) Refracted rays that occur while velocity increases monotonically with depth, (2) reflected rays from the layer boundaries, and (3) head-waves, which enter and exit a block at the critical angle and travel along the upper boundary of the block.

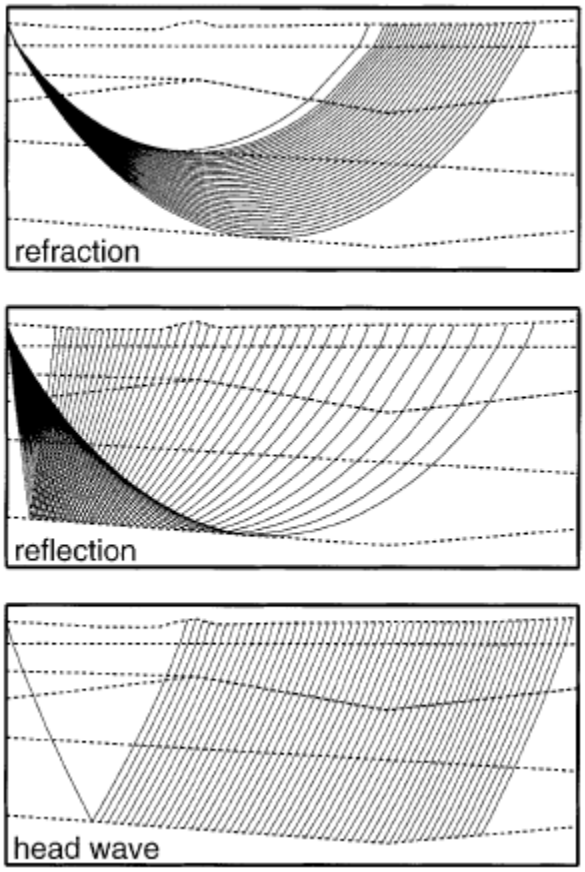

Figure 3.2: Ray groups are modeled via ray tracing: refracted waves, reflected waves, and head-waves (modified from Zelt, 1999).

3.2.3 Inversion

The inversion step refers to modifying the model parameters to minimize the misfit between the observed and calculated traveltimes. The ray path depends on the velocity structure thus making the traveltime inversion nonlinear. The inverse problem is solved by linearization using a Taylor series expansion about a starting model and neglecting higher order terms. A starting model and iterative approach are required due to the expansion. The linearized equation can be expressed as:

$$A\delta m = \delta t \tag{3.2}$$

$$\delta t = t_{obs} - t_{cal} \tag{3.3}$$

where A is the partial derivative matrix of travel time with respect to the model parameters (velocity or depth), δm is the model parameter adjustment vector, δt is the traveltime residual vector, representing the difference between the observed travel times (t_{obs}) and calculated travel times (t_{cal}). Both the traveltime residual vector and the partial derivative matrix are computed while ray tracing through a model during a particular iteration. After ray tracing, the parameter adjustment vector is solved for in (3.2) and applied to the current model, after which rays are traced through the updated model. This procedure is repeated until a satisfactory fit to the observed data is achieved, or a prescribed stopping criterion is satisfied.

Generally, the inverse problem is ill-conditioned, where the solution is non-unique or non-stable, and the problem is overdetermined. This is mainly related to the attempt to extract too much information from the data, and the noise in the data and errors both from the measurement uncertainties and the model approximations. Regularization of the solution is an effective way to deal with the ill-posed problem by including a priori information to the inverse problem. Additional constraints are imposed that control the under-determined part of the solution. A damped least-squares (DSL) technique as a form of regularization is used to solve the linearized equation (3.2) in an iterative approach that rays retraced after each iteration. The DSL solution is written as (Zelt and Smith, 1992):

$$\delta m = \left(A^T {C_d}^{-1} A + D {C_m}^{-1}\right)^{-1} A^T {C_d}^{-1} \delta t \tag{3.4}$$

where *D* is an overall damping parameter, usually equal to 1. C_d and C_m are the estimated data and model covariance matrices given by

$$C_d = diag\{{\sigma_i}^2\};\ C_m = diag\{{\sigma_j}^2\} \tag{3.5}$$

The standard deviation σ_i is the estimated uncertainty of the *i*th traveltime measurement and σ_j is an a priori estimate of the uncertainty of the *j*th model parameter.

3.3 P-wave velocity modeling

In order to obtain a reliable P-wave velocity model, we applied a 2D travel time inversion of reflected and refracted arrivals from OBS/MCS data. The MCS data provide a clear structural image but has extremely limited source-receiver offsets and thus cannot provide accurate velocity information. On the other hand, the wide-angle OBS data provide accurate velocity estimates but rather poor constraint on the structural image in comparison with that produced by MCS data. Therefore, by combining the two data sets in the travel time inversion, the velocity model can be better constructed.

3.3.1 Event identification

To facilitate the event identification, the near-offset OBS data were compared with the MCS reflection data at the location of OBS. Reflection events that originated from the same interface and were clear and continuous in both MCS and OBS data were identified and picked. Example of a comparison between MCS and wide-angle data from OBS 7 is shown in Figure 3.3. Since the OBS was offset from the MCS line, travel times of direct arrival in both data were different. MCS data was time-shifted to earlier arrival time in order to match the OBS data. Six reflections were identified: the seafloor (E1), the BSR (E6), four reflections between the seafloor and BSR (E2, E3, E4, E5). Below the BSR, the picking was not performed because no clear reflectors were recognized on either OBS or MCS data due to the poor quality of the data. Note that the BSR is a

strong reflector, and it thus masks structural features underneath. Hydrophone components of OBSs were chosen for picking of reflections. The picks were obtained up to 2.8 km on either side of the OBS stations. Beyond this distance, events are difficult to identify because of the weak signal and interference with other events. The picked reflections from OBS 7 are shown in Figure 3.4.

The arrival times of MCS data were picked on the common shot gathers; the picking of reflections was done at every shot at near offset (1 km on either side) of OBS locations, while every three shot with a spacing of 1.5 km at large offset. Considering the signal-to-noise ratio and complex geometry in the MCS data, the picking was done out to offsets of more than 4 km from the OBS locations for E1-E3 and E6 (BSR), up to 3 km for E4 and E5.

Several refractions were observed in both OBSs. By comparing their apparent velocities, some arrivals with similar velocities probably are the different phases from the same refraction; what's more, some refractions have very weak amplitudes and are not easy to pick on the raw data of OBS. The OBS data were filtered to better identify the seismic arrivals, but the picked arrival times were obtained from the unfiltered data to capture the original seismic waveform. Thus, one refraction event (E7) that is prominent in both OBSs was used for the inversion (Figure 3.5). This event has an apparent velocity of ~2.6-2.7 km/s and is associated with the layer below the BGR. The modeling of refractions from OBS data allowed us to determine the real base of the free gas layer and obtain the velocity information of the layer below BGR.

Based on the signal-to-noise ratio, an uncertainty of 20 ms was assigned for traveltime picks, except for the refraction where the uncertainty was 25 ms.

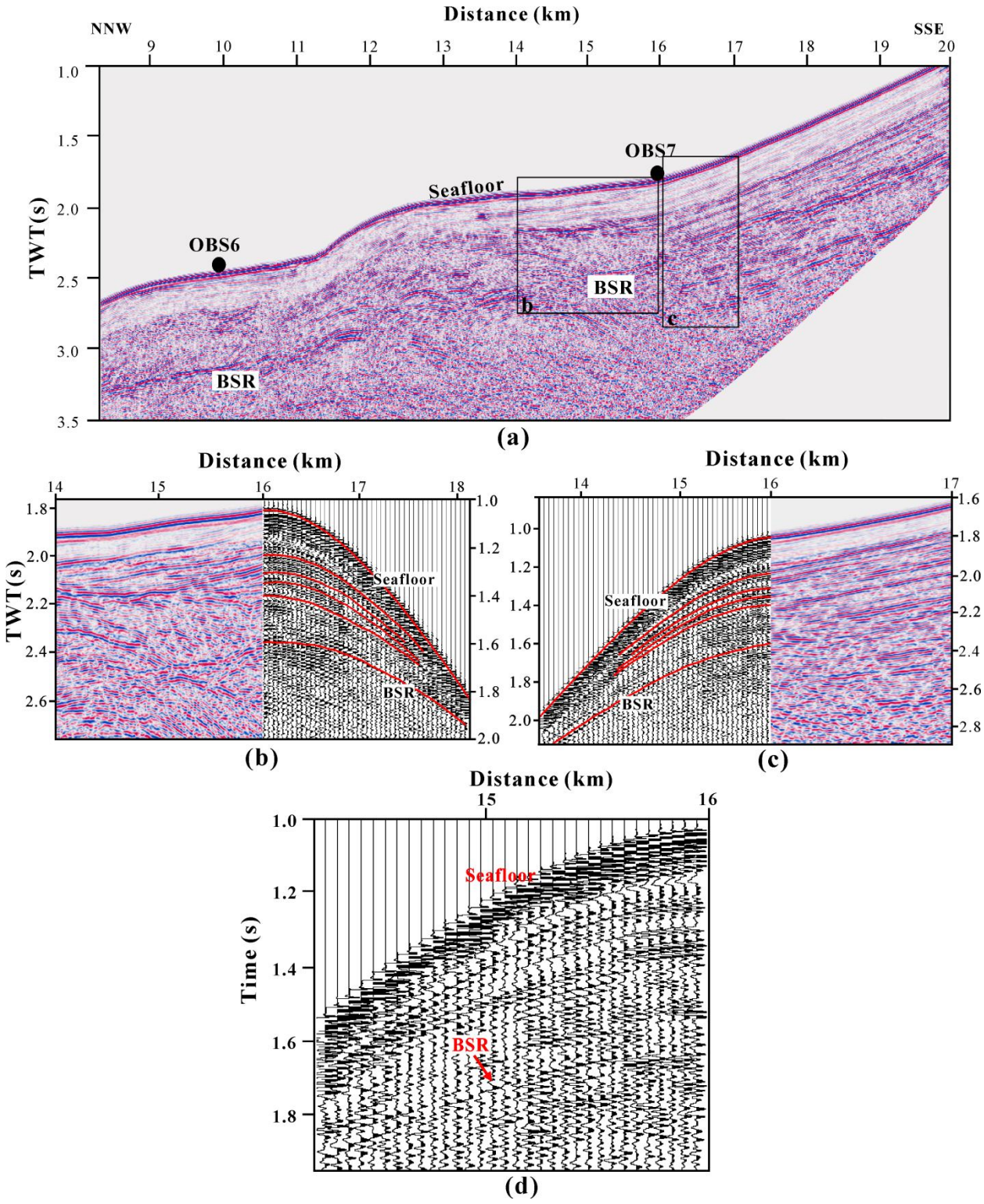

Figure 3.3: (a) Stack section of part of MCS line BSRstar8. An Automatic Gain Control (AGC) with a time window of 400 ms was applied to better image the BSR. The solid circles indicate the OBS locations projected on the MCS line. The boxes indicate the seismic part shown in panels (b) and (c); Panels (b) and (c) report the correlation of the hydrophone component of OBS 7 and the MCS stack section. The P-wave picks on the hydrophone data are shown as red lines on the OBS panels. See text for details; Panel (d) Close-up view of OBS panel (c) showing the BSR.

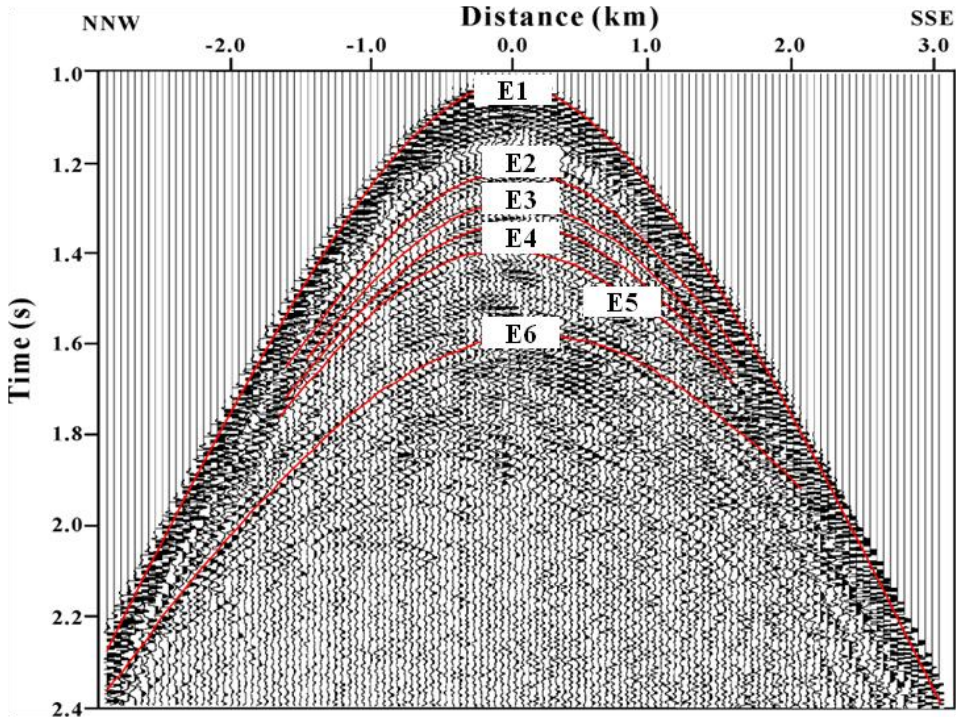

Figure 3.4: Travel time picks (red lines) of P-wave reflections from hydrophone component of OBS 7. The horizontal axis is the distance between projected OBS position and shot position.

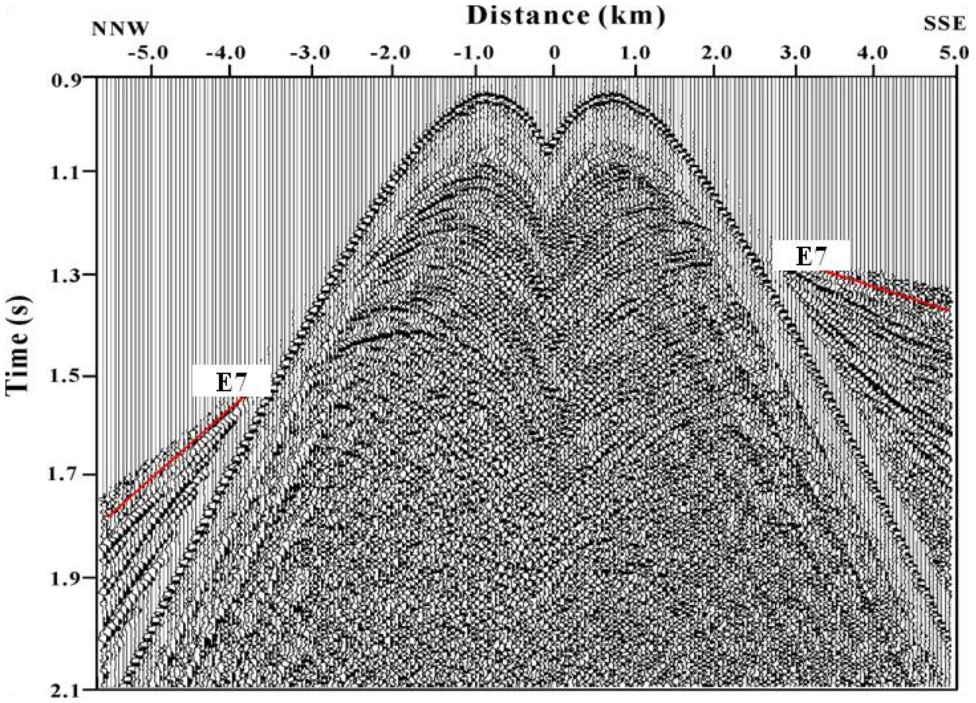

Figure 3.5: Travel time picks (red lines) of P-wave refraction from hydrophone component of OBS 7. The horizontal axis is the distance between projected OBS position and shot position. The time is reduced with a velocity of 3.2 km/s.

3.3.2 Modeling

The velocity model was obtained using the 2-D travel time inversion program Rayinvr deployed by Colin Zelt (Zelt and Smith, 1992), which employs a forward ray tracing step and a damped least-squares inversion step to modify the model parameters to minimize the difference between the observed and the predicted traveltimes. To satisfy the requirement of a 2D ray-tracing model, the OBS locations were projected onto the shooting line. As mentioned above, the OBSs drifted far from the shot line. So, taken into account the relative error of offset caused by projection (Figures 3.6 and 3.7), OBS reflections at near offset (as far as 1 km on either side) were excluded and only MCS data were used during the inversion to constrain the velocity model.

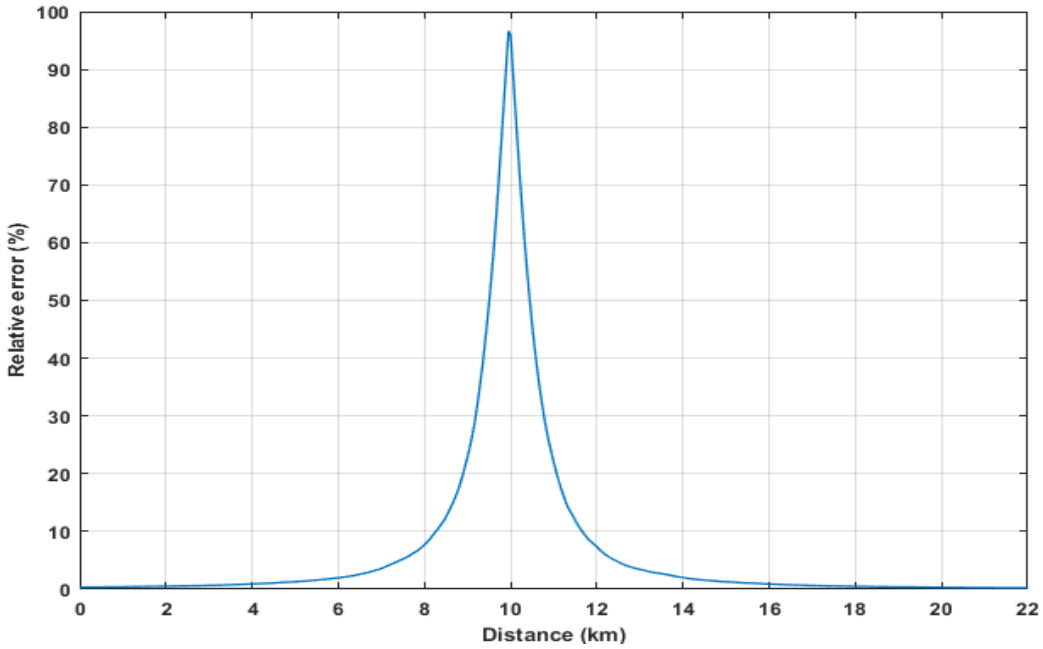

Figure 3.6: The relative error of offset for OBS 6.

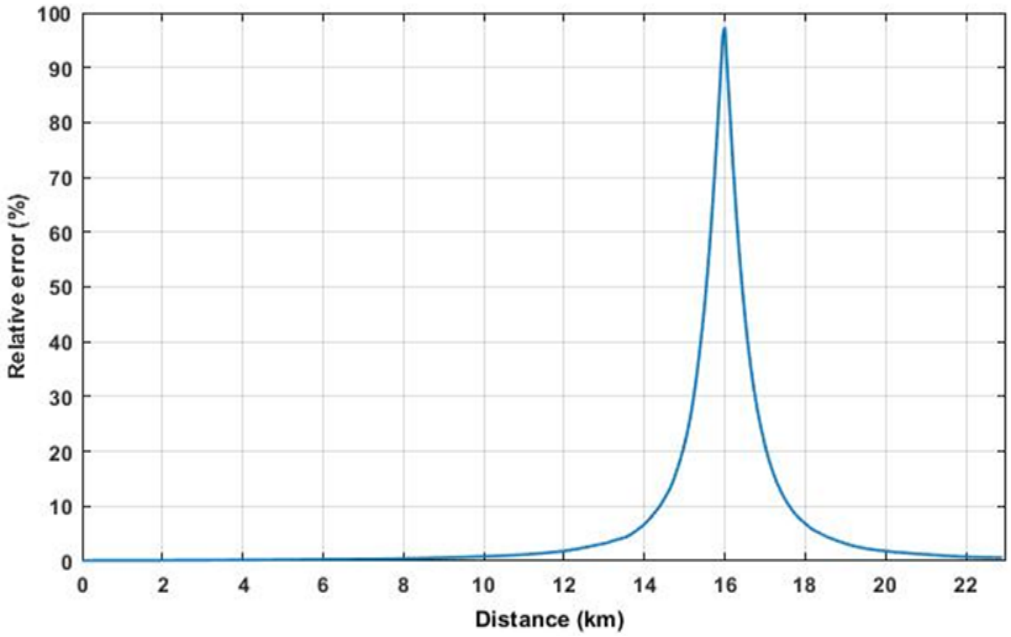

Figure 3.7: The relative error of offset for OBS 7

Since traveltime inversion is a non-linear problem, the algorithm first determines the ray paths in the starting model and then updates the velocity model assuming stationary rays. The starting velocity model was created based on the stack section of MCS line BSRstar8 and the velocity information obtained from previous studies which used pre-stack depth migration tool on nearby multichannel seismic line (Loreto et al., 2011 and the references therein). Rays were traced through this model and the travel times are calculated. Then calculated travel times are compared with the observed travel times, assessing the fit statistically within the assigned uncertainties. After initial forward modeling, the model parameters (velocity and depth) were iteratively adjusted to minimize the difference between observed and calculated travel times by using the damped least-squares inversion. Vertical velocity gradients were not allowed within individual model layers. The forward ray-tracing step and inversion step were repeated until a satisfactory fit was achieved, that was, the root-mean-square (RMS) travel time residual was within the assigned picking errors and the normalized $\chi 2$ (chi-square) was close to 1. This is equivalent to saying that the data fit within their estimated error bounds – assuming a Gaussian error distribution. This procedure was applied to all layers in a layer-stripping approach from the top to the bottom. In the forward modeling and

inversion, the refraction was modeled as a pure head wave. In the algorithm of Zelt and Smith (1992), head waves are much easier to use than turning waves and they are reasonable to use because the modeling is based on travel times and not on amplitudes. For small velocity gradients, traveltimes for head waves are nearly equal to traveltimes for turning waves. This is particularly true for OBS data, where the refractions are observed over a small offset range and hence contain little information about velocity gradients.

The velocity model was determined by simultaneous inversion of travel times from wide-angle reflections and refractions on the OBSs, and from reflections recorded on the MCS data. Figure 3.8 shows the ray diagram and travel time fit modeled on OBS 7. The model shows a good agreement between calculated and observed travel times. An RMS travel time residual of 23 ms with a normalized $\chi 2$ of 1.305 was achieved. Table 3.1 shows the inversion results for each phase.

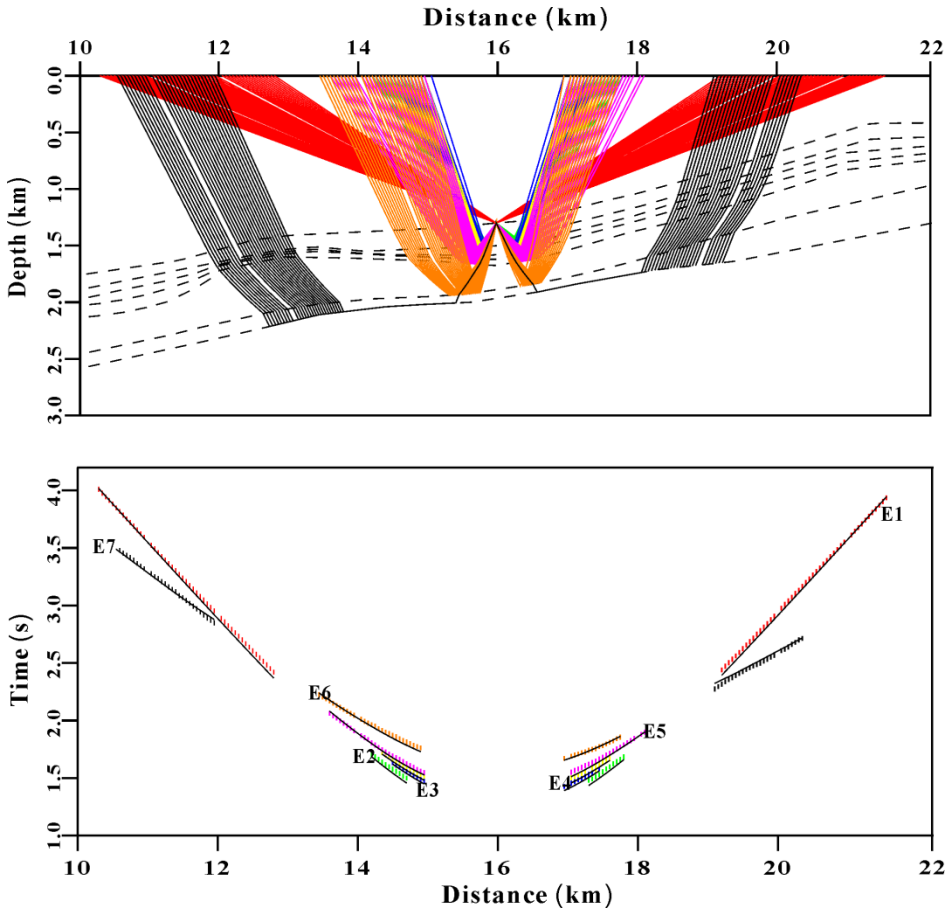

Figure 3.8: Top: P-wave ray diagram modeled on OBS 7; Bottom**:** the fit between calculated (solid lines) and observed (short vertical lines) travel times. The colors of observed travel times are the same as those of corresponding rays.

Table 3.1 The summary of P-wave velocity modeling for OBS 7

Phase	Npts	T_{rms} (s)	$\chi 2$
E1	95	0.027	1.721
E2	22	0.020	0.950
E3	25	0.023	1.432
E4	25	0.026	1.654
E5	48	0.019	0.916
E6	45	0.016	0.669
E7	53	0.024	0.980

3.4 S-wave velocity modeling

3.4.1 Event identification

S-wave velocities were determined by trial and error forward modeling of the travel times of converted S-waves from the inline component of OBS data and by inverting for Poisson's ratio, once a satisfactory P-wave velocity model has been obtained. This required the correlation of converted S-arrivals with their equivalent P-wave arrivals. The correlation is difficult and complicated because they have different time scales and have different reflection strengths. Here, only the PS-wave type was considered (Figure 3.9): P-wave propagates downward and converts to S-wave at a reflector when the energy does not impinge perpendicularly to the surface and then propagates upward as S-wave to the receiver. Other conversions from P- to S-wave may exist during reflection and transmission at intermediate interfaces, but the attenuation is high and they are too weak to be obvious (Kumar, 2005).

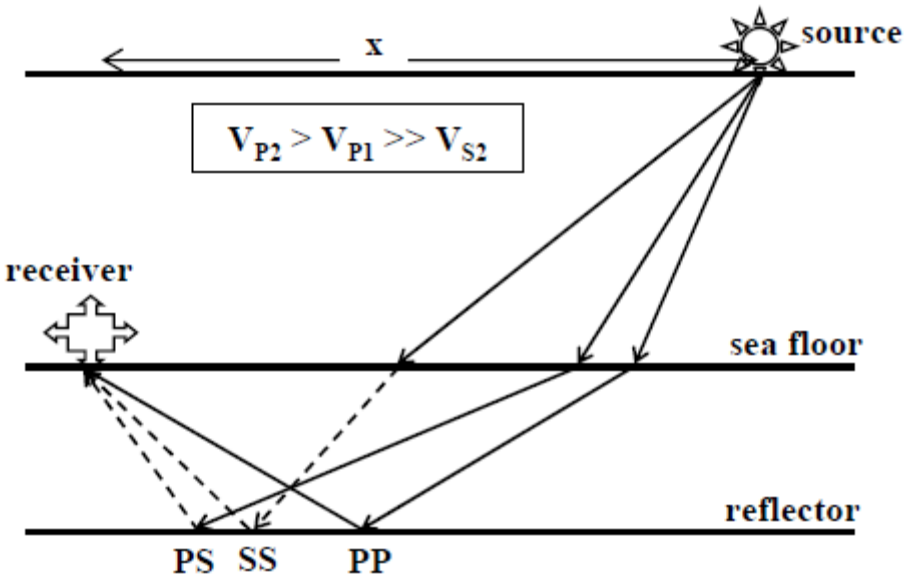

Figure 3.9: Ray paths of PP-, SS- and PS-waves for OBS. The P- and S-wave paths are shown with solid and dashed lines, respectively (from Kumar, 2005).

Because of the possible ambiguity in the correlation between PS-arrivals and corresponding P-arrivals, all the PS events with good signal-to-noise ratio were tested for each layer in order to obtain the event with the optimal fit between calculated and observed travel times. For each possible PS event, RMS travel time residual and chi-square value were calculated for a range of Poisson's ratios. Based on this procedure, the best fitting event and its corresponding Poisson's ratio value for each layer were obtained from the position of the chi-square minimum. A similar method to estimate S-wave velocities from OBS data has been described in several other studies (e.g., Westbrook et al., 2008; Peacock et al., 2010; Exley et al., 2010; Satyavani et al., 2016). Six PS-arrivals were identified and used for modeling. Figure 3.10a shows the picking of PS-arrivals (C2, C3, …, C7) from the inline component of OBS 7. The two events (C6 and C7) at about 2.6 s and 2.8 s at minimum offset were identified as PS-arrivals corresponding to the BSR and BGR, respectively. Considering the uncertainty in the exact arrival times of PS-arrivals, a large picking error was assigned. For the first four PS-arrivals (C2, C3, C4 and C5), an uncertainty of 25 ms was assigned. The events C6 and C7 were assigned a pick uncertainty of 30 ms.

3.4.2 Modeling

S-wave velocities were modeled by using ray-tracing module of Rayinvr (Zelt and Smith, 1992), based on a P-wave velocity model and Poisson's ratio for each layer. During the modeling, the interface depths and P-wave velocities in each layer obtained as described in the previous section were held constant, and the only variable parameter is the Poisson's ratio. The Poisson's ratio was perturbed until a best fit between the observed and calculated PS travel times was obtained. The obtained Poisson's ratio was finally translated into S-wave velocity, combing the P-wave velocity. This procedure was performed on both OBS stations. The PS ray-tracing modeling on OBS 7 is shown in Figure 3.10. An overall normalized $\chi 2$ of 1.086 and an RMS travel time residual of 27 ms were achieved. Table 3.2 shows the inversion results for each phase.

Table 3.2 The summary of S-wave velocity modeling for OBS 7

Phase	**Npts**	**T_{rms} (s)**	**$\chi 2$**
C2	50	0.027	1.160
C3	29	0.025	1.037
C4	47	0.030	1.462
C5	45	0.028	1. 260
C6	59	0.024	0.671
C7	53	0.025	0.689

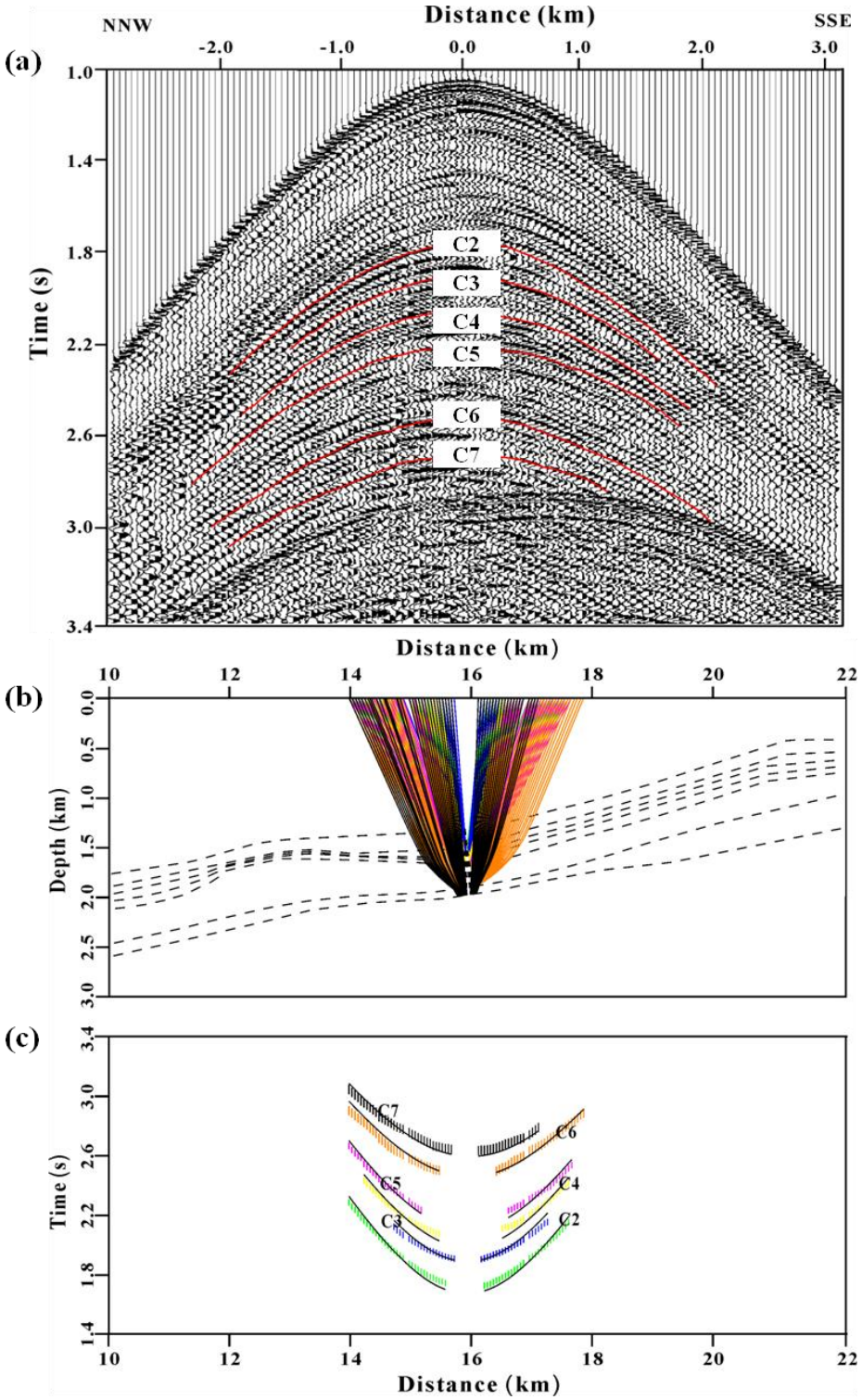

Figure 3.10: **(a)** Inline component of OBS 7 showing travel time picks (red lines) of PS-waves. The horizontal axis is the distance between projected OBS position and shot position. The travel times at minimum offset corresponding to the PS-waves are indicated with the red dots. (**b**) PS-wave ray diagram modeled on OBS 7; (**c**) The fit between calculated (solid lines) and observed (short vertical lines) travel times. The colors of observed travel times are the same as those of corresponding rays in Figure 3.10b.

3.5 Results: velocity model

The P-wave velocity model determined by the joint travel time inversion of reflections and refractions from OBS and MCS data is shown in Figure 3.11. The model indicates that the BSR is nearly parallel to the seafloor at about 510-650 m depth. The P-wave velocity increases gradually with depth down to the BSR. The layer just above the BSR shows a high P-wave velocity of 2.0-2.1 km/s that can be associated with the presence of gas hydrates. The layer below the BSR shows a low P-wave velocity of about 1.4-1.6 km/s that can be related to the presence of free gas. The BGR is identified at the depth varying between 80-160 m below the BSR; a velocity of 2.64-2.71 km/s is observed in the layer just below the BGR from analysis of the critical refractions in OBS data. A lateral variation is observed along the velocity model. In the shallow layer just below the seafloor, the overall trend of P-wave velocity shows a laterally increase from the SSE to NNW. In the layer just above the BSR, OBS 7 yields higher P-wave velocity compared to OBS 6, which results in the highest velocity of 2.1 km/s occurring in the eastern part, while the lowest velocity equal to 2.0 km/s is present in the western part of section. Velocity variations in the free gas layer below the BSR are also observable. The lowest velocity (1.4 km/s) is found in the western part where the BSR is stronger.

Figure 3.12 shows the vertical profiles of P- and S-wave velocities and Poisson's ratio at the location of OBS 7. The S-wave velocity shows a continuous increase with depth and reaches a value of about 840 m/s at the BSR. Beneath the BSR, no significant increase or decrease was found, as the S-wave velocity is insensitive to pore fluid saturation. The Poisson's ratio shows a relatively continuous decrease with depth down to BSR and a strong decrease in the free gas layer below the BSR.

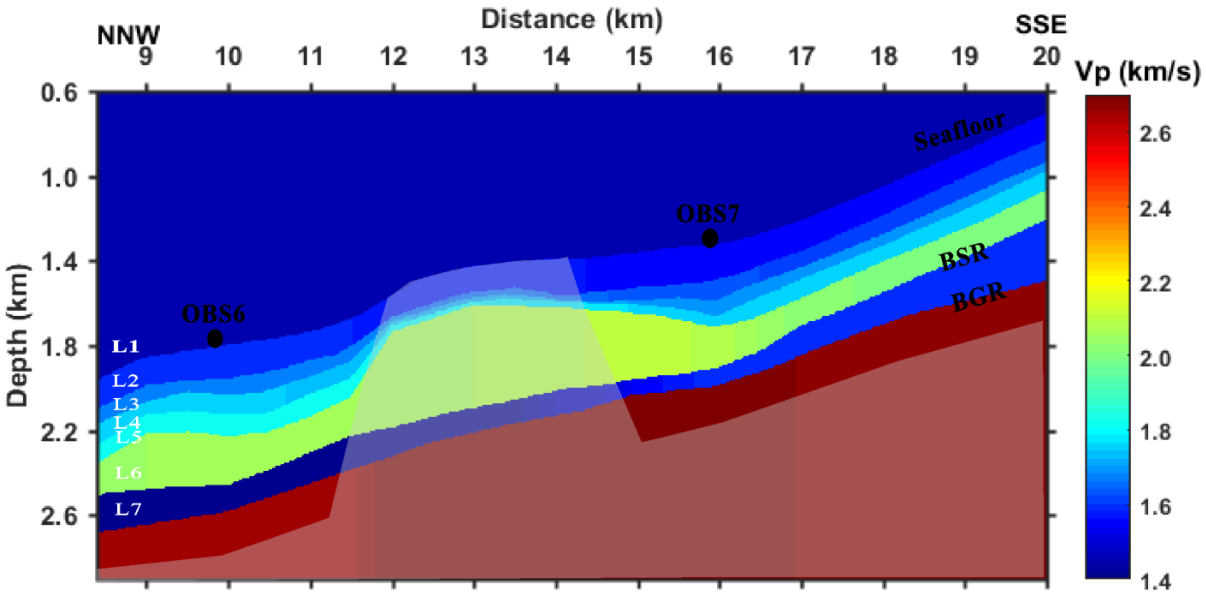

Figure 3.11: P-wave velocity model obtained after joint inversion of MCS and OBS data. The shading indicates the zone with no ray coverage constraints for the P-wave velocity modeling.

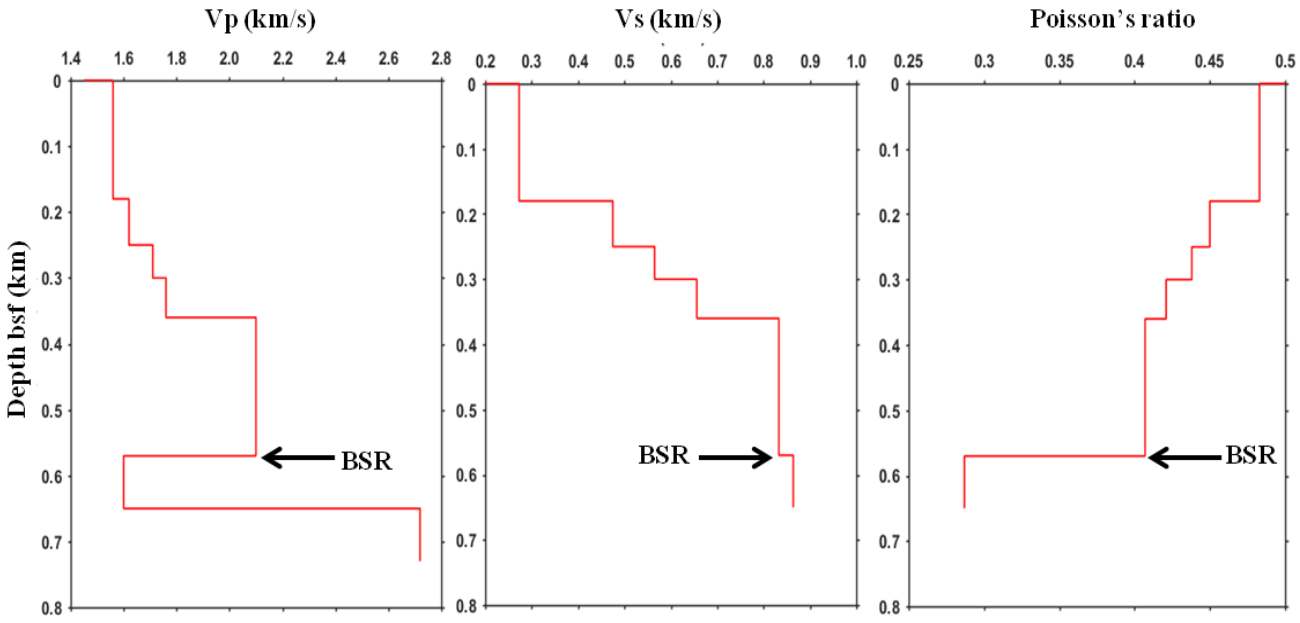

Figure 3.12: P- and S-wave velocity and Poisson's ratio profiles extracted at the location of OBS 7.

3.6 Uncertainty of the velocity model

There are two primary sources of errors in the final velocity model: projection and inversion. The former is caused by the drift of the OBS from the MCS line during placement. The error in P- and S-wave velocity caused by the geometry projection was evaluated by observing the residual between the calculated and observed travel time picked at near offset of the OBS data, using the final velocity model. The percentage error is defined as the ratio between travel time residual and observed travel time. The velocity error from the travel time inversion depends on the number of picked traveltime arrivals and the uncertainty assigned to those picks. In order to estimate the uncertainty in the velocity model from the traveltime inversion, we performed a sensitivity analysis based on the approach as described by Katzman (1994): We perturbed the velocity values of each layer until the RMS travel time residual and normalized $\chi 2$ increased significantly from the values obtained from the final model. Figure 3.13 shows an example of sensitivity analysis applied to the layer just below the seafloor (Layer 2). The uncertainties in S-wave velocity from travel time inversion were obtained through perturbing the Poisson's ratio, following the similar approach as used for the P-wave velocity. For a given layer, we increased and decreased the Poisson's ratio until the RMS traveltime residual and normalized $\chi 2$ value increased significantly from the optimized value, while keeping P-wave velocity and the Poisson's ratio for other layers fixed at their final calculated value. We observed that the shallow layers are more sensitive to the variation of Poisson's ratio than the deep layers. The estimation of uncertainty in P-wave and S-wave velocities was performed for all the layers including the water column (Layer L1) (Table 3.3).

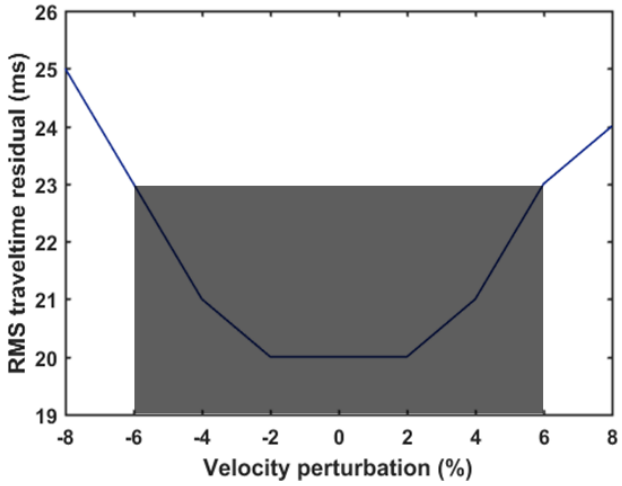

Figure 3.13: An example of sensitivity analysis applied to the velocity of Layer L2. An approximate estimate of the uncertainty is ±6%, as indicated by the shaded box.

Table 3.3 Percentage errors of P-wave and S-wave velocities estimated from the sensitivity analysis

Layer	Error in Vp (%)			Error in Vs (%)		
	Projection error	**Inversion error**	**Total error**	**Projection error**	**Inversion error**	**Total error**
L1	NO	1	1	NO	NO	NO
L2	6	6	12	6	3	9
L3	5	9	14	5	10	15
L4	3	10	13	3	10	13
L5	2	10	12	2	11	13
L6	1	9	10	1	9	10
L7	1	9	10	1	10	11

3.7 Modified velocity model

From the errors in Table 3.3, we observed that the projection errors are high in the shallow layers (L2, L3 and L4) and decrease with the depth; the inversion errors are high in the Layers L3, L4 and L5 for both P- and S-wave velocity, which is related to the small thicknesses of these layers. So, in order to reduce the errors, we did some tests to modify the velocity model. The traveltime picks of

E2 from OBS data was not used in the inversion, and the Layers L3 and L4 in the previous velocity model were removed. Figure 3.14 and Table 3.4 show the modified velocity model and the errors in each layer. Figure 3.15 shows the vertical profiles of P- and S-wave velocities and Poisson's ratio at the OBS locations. As can be seen, the modified model shows a similar velocity trend with the previous one.

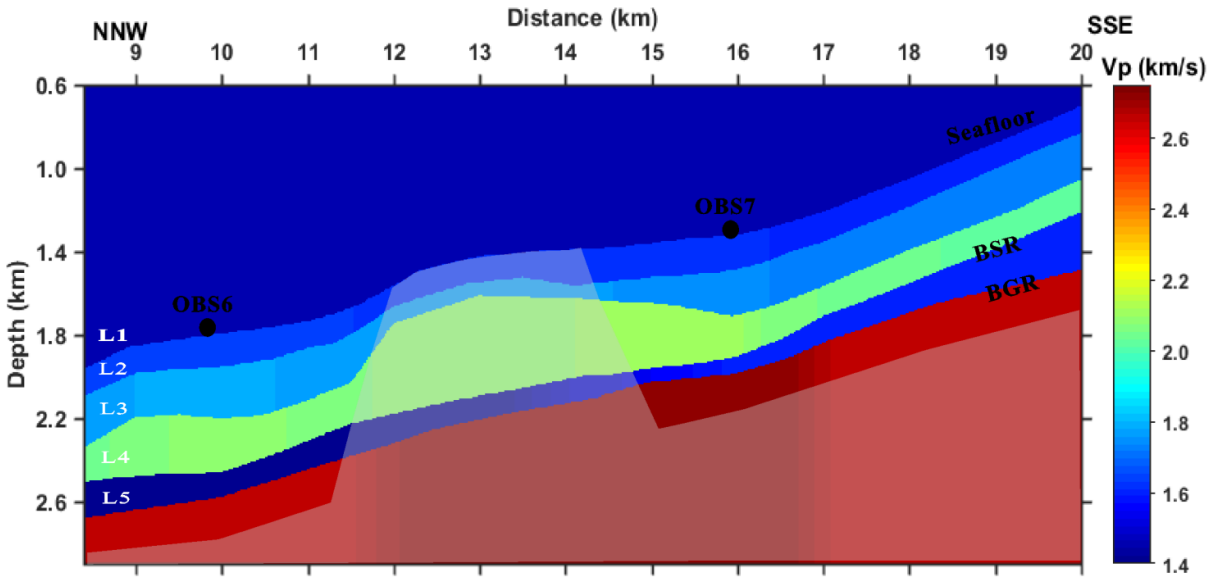

Figure 3.14: Modified P-wave velocity model.

Table 3.4 Percentage errors of P-wave and S-wave velocities in the modified model.

Layer	Error in Vp (%)			Error in Vs (%)		
	Projection error	**Inversion error**	**Total error**	**Projection error**	**Inversion error**	**Total error**
L1	NO	1	1	NO	NO	NO
L2	NO	6	6	6	3	9
L3	2	6	8	2	6	8
L4	1	7	8	1	7	8
L5	1	7	8	1	9	10

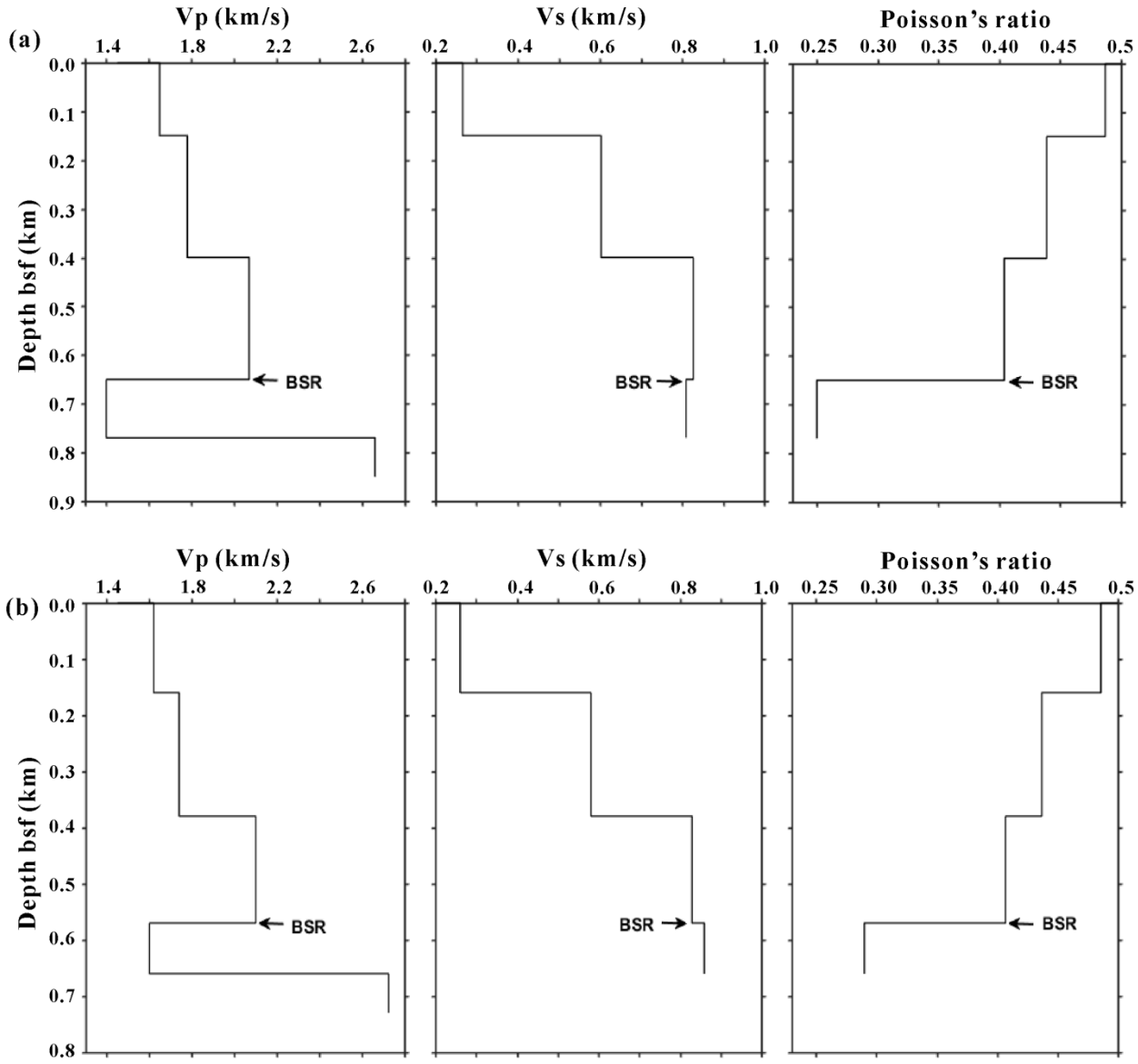

Figure 3.15: The P- and S-wave velocity and Poisson's ratio profile extracted at the locations of OBS 6 (a) and OBS 7 (b).

3.8 Summary

In this chapter, the traveltime inversion algorithm of Zelt and Smith (1992) was applied to OBS and MCS data to determine P- and S-wave velocity fields. By correlating the reflection events of MCS data with those at near offset recorded by the hydrophone component of OBS data, the corresponding horizons were selected and picked. The S-wave velocity was determined by forward

modeling of the travel times of converted S-waves from the inline component of OBS data, which allows us to obtain Poisson's ratio estimates and information concerning the layer below the BSR, which is difficult to obtain from P-wave data because of strong velocity attenuation. At the beginning, six reflections and one refraction were identified and included in the inversion. The high velocity layer observed just above the BSR can be associated with the presence of gas hydrates; the low velocity layer below the BSR can be related to the presence of free gas. The uncertainty analysis of velocity models suggests that the projection error caused by the drift of the OBS from the MCS line is high in the shallow layer, while the inversion error is high in the layer with small thickness. Take into account this analysis, a modified velocity model with lower uncertainty was obtained, which shows a similar velocity trend in the layer just above and below the BSR.

Chapter 4

Estimation of gas hydrate and free gas concentrations

4.1 Introduction

Where no direct measurements are available, detailed P- and/or S-wave velocity distribution in marine sediments is essential for estimating the concentration of gas hydrate and free gas in the pore space (e.g., Lee et al., 1996; Ecker et al., 2000; Jakobsen et al., 2000; Chand et al., 2004). The presence of gas hydrate increases P- and S-wave velocity with respect to the background velocity at full-water saturation, while the presence of free gas the reduces the P-wave velocity. Therefore, the amount of gas hydrate and free gas can be estimated from the velocity discrepancies between observed velocity and background velocity if knowing the relationship between the velocity and gas-phase concentration. Several theoretical methods have been proposed to predict this relationship that can be broadly divided into two categories. One is the empirical relations which are simple and straightforward, such as Wood equation (Wood, 1941), time-average equation (Wyllie et al., 1958), and Weighted-equation (Lee et al., 1996). Another is the rock physics-models, which take into account the pore-scale interaction between gas hydrate and sediment matrix and also account for the porosity reduction (Ecker et al., 1998; Helgerud et al., 1999; Carcione and Tinivella 2000; Jakobsen et al., 2000; Chand et al., 2004).

In this study, we adopted the theoretical model proposed by Tinivella (1999, 2002). This theoretical model is based on a modified Biot-Geerstma-Smit theory and has been successfully applied in this same geographical area (e.g., Loreto et al., 2011). In this chapter, we firstly give a brief overview of the most commonly used theoretical models in literature, including empirical relations such as weighted-equation (WE) (Lee et al., 1996), three-phase effective medium theory (TPEM) (Ecker et al., 1998; Helgerud et al., 1999; Ecker et al., 2000), an approach using

differential effective-medium theory (DEM) (Jakobsen et al., 2000) and a three-phase Biot theory (TPB) (Carcione and Tinivella, 2000; Gei and Carcione, 2003) and. And then the approximated modified-Biot theory was described in detail and used to estimate the gas hydrate and free gas concentration. The results were also discussed in this chapter.

4.2 Available theories in literature

4.2.1 Empirical relations

The Wood equation is one of the oldest methods used to obtain gas hydrate concentration in situ. It is valid in high porosity media where hydrates are suspended in the pore space. The three-phase Wood's equation for hydrate-bearing sediments can be defined as:

$$\frac{1}{\rho {V_p}^2} = \frac{\emptyset(1-S)}{\rho_w {V_w}^2} + \frac{\emptyset S}{\rho_h {V_h}^2} + \frac{1-\emptyset}{\rho_m {V_m}^2} \tag{4.1}$$

where V_h is the P-wave velocity of the pure hydrate; ρ_h is the density of pure hydrate; ρ is the bulk density of the medium; ρ_w is the density of pore water; ρ_m is the density of rock matrix; and *S* is the concentration of hydrate in the pore space(as a fraction).

Wyllie et al. (1958) considered that the velocity in the version of a whole rock depends on the presence of fluid in the rock matrix in time average equation. Timur (1968) first proposed a three-phase time average equation based on slowness averaging (Wyllie's equation) to relate the porosity and ice saturation with the P-wave velocity in consolidated permafrost sediments. Pearson et al. (1983) applied the equation to hydrate-bearing rock and concluded that it qualitatively explains the known sonic properties of hydrate-bearing sediment in consolidated media. The problem of

transition from “suspension” to “compacted” sediment was treated with combined models. For instance, averaging bulk moduli weighted with the respective porosities [Voigt’s model (Voigt, 1928)] gives a simple model for consolidated sediments, whereas averaging the reciprocal of bulk moduli [Reuss’s model (Reuss, 1929)] accounts for unconsolidated media. Wyllie’s equation is an empirical equation which was established based on consolidated rocks, and is not suitable for high-porosity unconsolidated sediments. Kuster and Toksöz (1974) suggest that unconsolidated permafrost sandstone could be modeled by spherical inclusion of water and ice caged in an aggregation of spherical quartz grains. Based on the two-phase theory developed by Kuster and Toksöz, Zimmerman and King (1986) first computed the effective elastic moduli of the ice-water mixture, with water playing the role of inclusion, yielding a homogeneous medium where the sand grains are the inclusion.

In the time-average equation, the velocity was calculated from the weighted sum of various constituents. The three-phase time-average equation is defined as follows:

$$\frac{1}{V_P} = \frac{\emptyset(1-S)}{V_w} + \frac{\emptyset S}{V_h} + \frac{1-\emptyset}{V_m} \tag{4.2}$$

where V_P, V_h, V_w, V_m is the P-wave velocity of hydrate-bearing sediment, pure hydrate, fluid, and sediment matrix; $\emptyset$ is the porosity and S is the hydrate concentration in the pore space.

The time-average equations were not always consistent unless an artificially low matrix velocity was used. Wyllie’s time-average equation is more suitable in less porosity media if hydrates cement grain contacts. Lee et al. (1996) proposed a weighted mean of the three-phase Wood equation and the three-phase time-average equation to estimate the P-wave velocity of hydrate-bearing marine sediment. The weighted equation is defined as follows:

$$\frac{1}{V_P} = \frac{W\emptyset(1-S)^n}{V_{P1}} + \frac{1-W\emptyset(1-S)^n}{V_{P2}} \tag{4.3}$$

where V_{P1} is the P-wave velocity calculated from the Wood equation and V_{P2} is P-wave velocity calculated from the time-average equation, *W* is a weighted factor and *n* is a constant simulating the rate of lithification with hydrate concentration. The weight *W* is derived from regression analysis of P-wave velocity and porosity in no-hydrate-bearing sediment and the n is determined from regression analysis of P-wave velocity and gas hydrate concentration. A value of $W > 1$ and low n favours the Wood equation and a value of $W < 1$ and high *n* favours the time-average equation.

The weighted equation is simple and straightforward to implement and the parameters can be adjusted to fit the given data, but it lacks physical meaning and the weighted factor requires substantial data to be constrained. Moreover, the model can be applied only to the settings that have the similar type of sediment because of the parameters are derived empirically. S-wave velocity is normally estimated from P-wave velocity based on an empirical relation, so it does not account for the change in S-wave velocity when hydrate starts contributing to the strength of the sediment frame.

The advantage of empirical relations is that they are based on actual observations and very simple to implement. However, empirical relationships are not necessarily valid in all geological settings or for rock properties different from where they were formulated.

4.2.2 Three-phase effective-medium theory (TPEM)

Helgerud et al. (1999) proposed a first-principle-based effective medium model which can be used to model the elastic-wave velocity in unconsolidated, high porosity, ocean bottom sediments containing gas hydrate, based on the model of Dvorkin et al. (1999). Rock-physics models take into account the pore-scale internal structure of hydrate-bearing sediments. These methods can effectively consider two cases of hydrate morphology: “cementation model” (gas hydrates are supposed to cement either at the grain boundaries or wrap around the grains) and “contact model” (hydrate is considered as a part of pore fluid or as a part of solid sediment) (Ecker et al., 1998,

2000). The cementation model predicts the normal and shear stiffness of a two-grain combination with elastic cement at the contact, based on the theory of Dvorkin et al. (1991, 1994), Dvorkin and Nur (1996). The grain contact model calculates the initial dry rock moduli at critical porosity using Hertz–Mindlin theory (Mindlin, 1949). The dry sediment moduli at all porosities are then calculated from modified Hashin–Shtrikman (H–S) bounds (Dvorkin and Nur, 1996). Therefore, the dry rock moduli depend on porosity, elastic moduli of the solid phase, effective pressure, Poisson ratio of the composite sediment and the average number of contacts per grain in sphere pack.

If hydrate is a part of the pore fluid, it does not affect the stiffness of the dry frame and the bulk modulus is calculated by using the Reuss average of the pore fluid and hydrate bulk moduli. If hydrate is a part of solid, both bulk and shear moduli are calculated from the Reuss average of the bulk moduli of sediment, hydrate and pore fluid, and the Reuss average of the shear moduli of sediment and hydrate. In the case of mixed mineralogy, the bulk moduli of sediment matrix are computed by Voigt-Reuss-Hill average. Once the dry rock moduli have been determined, the Gassmann equation is used to estimate the saturated rock moduli (Gassmann, 1951).

4.2.3 Differential effective-medium theory (DEM)

Jakobsen et al. (2000) proposed a theory to model clay-rich hydrate-bearing sediment, based on a combination of a self-consistent approximation (SCA) (Willis, 1977), a differential effective medium theory (DEM) (Nishizawa, 1982), and a method of smoothing for crystalline aggregates (Bonilla and Keller, 1985). In this theory, the elastic properties of sediments are related to porosity, mineralogy, microstructure, clay particle anisotropy and hydrate saturation. The self-consistent approximation theory is used to create a bi-connected effective microstructure between porosity of 40% and 60%, and the DEM theory is used to adjust the component to that of the sediment. Since the DEM theory preserves the connectivity of the background phases (Sheng, 1990), this approach produces the sediment that is bi-connected at all porosities. The limitations of this theory are that

the weaker bonding and greater compliance likely to exist at the edges of the individual domains of preferential particle alignment and the pressure effects are not considered.

4.2.4 Three-phase Biot-theory (TPB)

A three-phase theory for frozen porous media was developed by Leclaire et al. (1994) and it assumes that there is no direct contact between solid grains and ice. It predicts three compressional waves and two shear waves, and it can be applied to unconsolidated and consolidated media. This theory has been confirmed with laboratory experiments (Leclaire et al., 1995). On the basis of the theory of Leclaire et al. (1994), Carcione and Tinivella (2000) have included the contributions to the potential and kinetic energies due to the contact between the solid grains and the hydrates, and the stiffening of the skeleton due to grain cementation. Unlike previous theories that simply based on slowness and/or moduli averaging or two-phase models, the three-phase Biot-theory (TPB) considers the existence of two solids (grains and gas hydrate) and a fluid. The TPB theory includes viscoelastic and viscodynamic effects to describe the observed wave loss from seismic to ultrasonic frequencies. Besides, it predicts the velocity dispersion from low to high frequencies and the velocity and Q-factor decrease with decreasing effective pressure. Gei and Carcione (2003) further generalized this theory to include the effects of pore pressure, partial saturation (gas and water), and different kinds of loss mechanisms. The resulting P-wave dispersion relation constitutes a generalization of Gassmann equation for two frames and one fluid, assuming that hydrate fills the pore space and shows interconnection. Carcione and Gei (2004) considered the low-frequency limit of the theory, thus neglected dissipation. At this limit, grains, hydrate and water were in the isostrain state, and the equations had a simplified form. The dry rock moduli were obtained from sonic log data at full-water saturation, and the moduli of the hydrate frame were obtained from the theory of Kuster and Toksöz (1974).

Lee (2002) proposed a similar method to predicted elastic wave velocities of unconsolidated

hydrate-bearing sediment based on theories of Biot and Gassmann. The method assumed that the S to P-wave velocity ratio of the sediment was proportional to that of the matrix and its porosity. In this method, the Biot coefficient was calculated from the weighted equation or effective medium theory. Gassmann's theory provided the relationship between the bulk modulus of the formation and bulk modulus of the matrix and Biot coefficient.

Lee and Waite (2008) modeled the sonic velocities of hydrate-bearing sediment by using the TPB theory. But the simplified method was different from that of Carcione's. Bulk and shear moduli for both the sediment and hydrate framework were derived from the expressions proposed by Lee (2005) for a dry framework. A consolidation parameter was proposed in the method, which accounted for sediment stiffening due to consolidation. In addition, a constant that accounted for the reduced impact of hydrate formation relative to compaction in terms of stiffening the host sediment framework was proposed.

4.3 Approximated modified-Biot theory

The final velocity field obtained from travel time inversion can be used to estimate the concentrations of gas hydrate and free gas in the pore space. In this study, we adopted the theoretical model proposed by Tinivella (1999, 2002) to quantify the amounts of gas hydrate and free gas by converting the velocity anomalies with respect to the reference velocities at full-water saturation. Positive velocity anomalies are considered as an indication for the presence of gas hydrates, while negative velocity anomalies are considered as caused by free gas. This theoretical model is based on a modified Biot-Geerstma-Smit theory and was successfully tested by using sonic log data and indirect hydrate concentration from chloride content in core logs (Tinivella, 1999). The theory includes an explicit dependence on differential pressure and depth, and considers the effects of grain cementation at high concentration of gas hydrates on the shear modulus of the sediment matrix. It models the coexistence of two solid phases (grains and clathrates), and two fluid

phases (water and free gas). The method gives the equations of both P- and S-wave velocities as functions of some physical parameters, such as porosity, compressibility, rigidity, density and frequency dependence. These parameters can be determined from available lithostratigraphic information and experimental data sets (Hamilton's curves (Hamilton, 1976, 1979)).

The compressional and shear wave velocities are expressed as (see symbols and variations of these equations in Table 4.1):

$$V_P = \left\{ \left[\left(\frac{1}{C_m} + \frac{4}{3}\mu \right) + \frac{\frac{\emptyset_{eff}}{k}\frac{\rho_m}{\rho_f} + \left(1-\beta-2\cdot\frac{\emptyset_{eff}}{k}\right)\cdot(1-\beta)}{(1-\emptyset_{eff}-\beta)C_b + \emptyset_{eff}C_f} \right] \cdot \frac{1}{\rho_m\left(1-\frac{\emptyset_{eff}}{k}\frac{\rho_f}{\rho_m}\right)} \right\}^{1/2} \tag{4.4}$$

$$V_s = \left[\frac{\mu}{\rho_m\left(1-\frac{\emptyset_{eff}}{k}\frac{\rho_m}{\rho_f}\right)} \right]^{1/2} \tag{4.5}$$

This theoretical model can be applied in three different situations: (1) full water saturation; (2) water and gas hydrates in the pore space; and (3) water and free gas in the pore space. The effect of grain cementation at high concentrations of gas hydrate is considered by using a percolation model (Leclaire 1992), which describes the transition of a two-phase system from a continuous (grain completely cementation) to a discontinuous (uncemented grains) state. Finally, it is worth mentioning that the coupling factor k describes the degree of coupling between pore fluid and solid frame. Numerically, it ranges from one (no coupling) to infinity (perfect coupling) and is a function of the frequency of the elastic wave considered. Note that the velocities are independent of frequency when the coupling factor is infinity (zero-frequency case).

The theoretical model has been compared with the three-phase Biot theory and the comparison shows that the two models are in very good agreement (Figure 4.1). The theory indicates an

increase of both Vp and Vs in the presence of gas hydrates, and shows a sudden decrease of Vp and an increase of Vs in the presence of the free gas. Note that the velocities increase significantly at high hydrate concentration, while a small amount of free gas reduces drastically the Vp. The theory has been applied to verify the model and to estimate the gas hydrate and the free gas concentrations in three different areas: South Shetland margin (Tinivella and Accaino, 2000; Lodolo et al., 2002; Tinivella et al., 2002; Tinivella et al., 2009; Loreto et al., 2011), Blake Ridge (Tinivella, 1999; Tinivella and Lodolo, 2000), and Cascadia margin (Tinivella and Carcione, 2001).

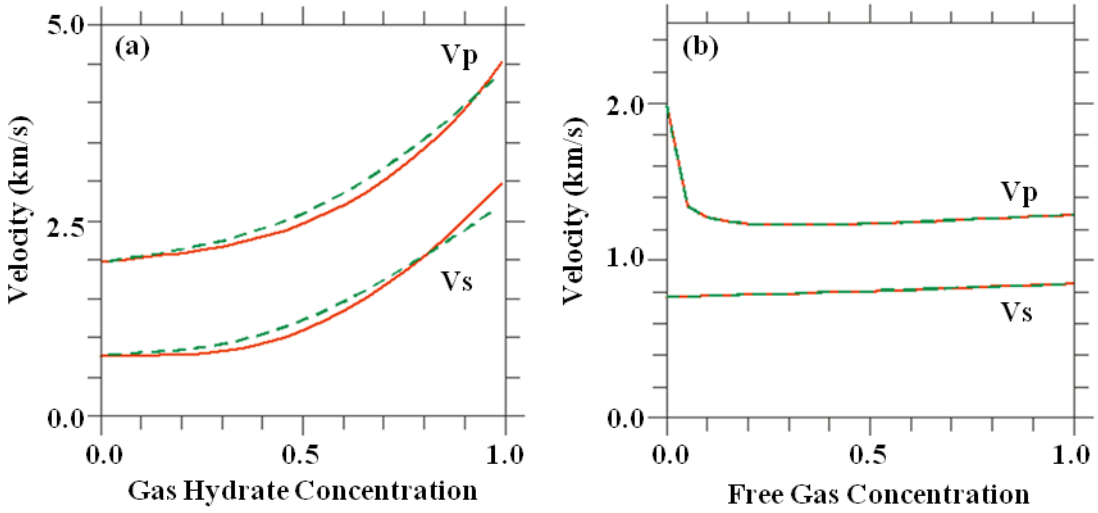

Figure 4.1: Comparison between the three-phase Biot theory (solid red lines) and the approximation for seismic frequency (green dashed lines). Seismic compressional (Vp) and shear (Vs) velocity versus gas hydrate (a) and free gas concentration (b), assuming a uniform distribution. (modified after Tinivella and Giustiniani, 2012).

Two main free gas distributions in the pore space can be modeled in this theoretical model: uniform–saturation distribution (i.e., gas and water in pore space, hereafter called case I) and patchy-saturation distribution (i.e., all water is concentrated in fully saturated patches, and gas is concentrated in patches without water, hereafter called case II). The fluid compressibility in the case of free gas uniformly distributed is given by

$$C_f = s_w \cdot C_w + s_g \cdot C_g \tag{4.6}$$

and in the free gas patchily distributed by

$$C_f{}^{-1} = \frac{4}{3}\mu\left\{\left[\frac{s_w}{1+(4/3\mu\cdot C_w)^{-1}} + \frac{s_g}{1+(4/3\mu\cdot C_g)^{-1}}\right]^{-1} - 1\right\} \tag{4.7}$$

Figures 4.2 and 4.3 show the compressional wave velocity and Poisson's ratio versus free gas saturation calculated in the case of uniform-saturation model (solid line) and patchy-saturation model (broken line). The decrease in velocity and Poisson's ration is more pronounced in the patchy-saturation model.

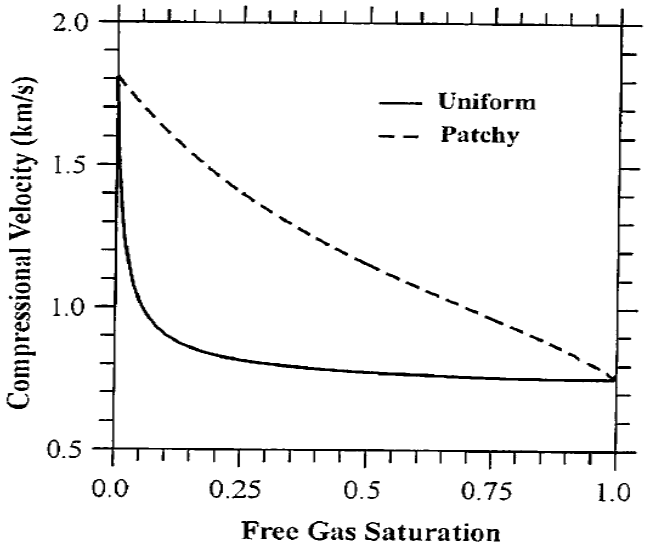

Figure 4.2: Compressional velocity versus free-gas saturation calculated with the uniform-saturation model (solid line) and the patchy-saturation model (broken line) (from Tinivella, 2002).

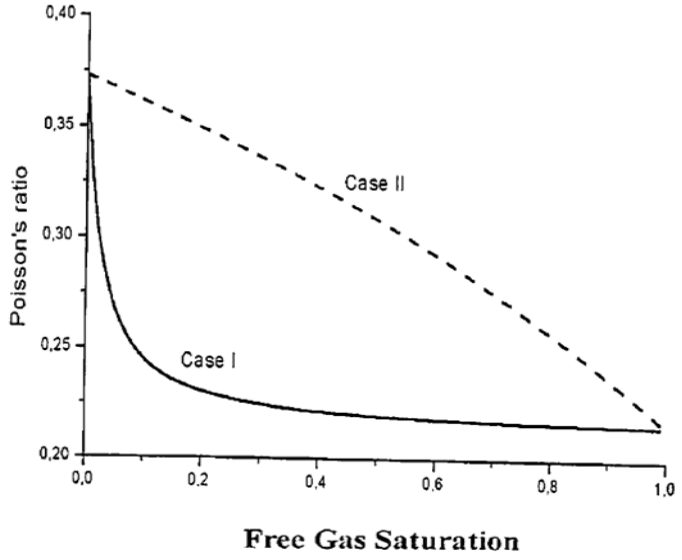

Figure 4.3: Poisson's ratio versus free-gas saturation calculated with the uniform-saturation model (solid line) and the patchy-saturation model (broken line) (from Tinivella, 2002).

Table 4.1 List of parameters and variation of material properties versus depth (after Tinivella, 1999)

$\emptyset$	Porosity
$\emptyset_s$	Solid proportion
$\emptyset_h$	Gas hydrate proportion
$\emptyset_w$	Water proportion
$\emptyset_g$	Free gas proportion
$\emptyset_s + \emptyset_w + \emptyset_g = 1$	
$\emptyset_s + \emptyset_h + \emptyset_w = 1$	
$c_h = \emptyset_h/(\emptyset_h + \emptyset_w)$	Gas hydrate concentration
$s_s = \emptyset_s/(\emptyset_s + \emptyset_h)$	Grain saturation
$s_h = \emptyset_h/(\emptyset_h + \emptyset_s)$	Gas hydrate saturation
$s_w = \emptyset_w/(\emptyset_w + \emptyset_g)$	Water saturation
$s_g = \emptyset_g/(\emptyset_w + \emptyset_g)$	Free gas saturation
$\emptyset_{eff} = (1 - c_h)\emptyset$	Effective porosity
C_s	Grain compressibility
C_h	Gas hydrate compressibility
C_w	Water compressibility
C_g	Free gas compressibility
C_b	Compressibility of the solid phase
C_f	Compressibility of the fluid phase
$C_p = (1 - \emptyset/\emptyset_0)/\ \mathrm{P_d}$	Pore compressibility
$\emptyset_0$	Porosity at the sea bottom
$\mathrm{P_d}$	Differential pressure
$C_m = (1 - \emptyset_{\mathrm{eff}})C_b + \emptyset_{\mathrm{eff}}C_p$	Compressibility of the matrix
$\beta = C_b/C_m$	
ρ_s	Grain density
ρ_h	Gas hydrate density
ρ_w	Water density
ρ_g	Gas density
$\rho_b = s_s\rho_s + s_h\rho_h$	Density of the solid phase
$\rho_f = s_w\rho_w + s_g\rho_g$	Density of the fluid phase
$\rho_m = (1 - \emptyset_{\mathrm{eff}})\rho_b + \emptyset_{\mathrm{eff}}\rho_f$	Average density
μ_{sm0}	Solid matrix shear modulus (no cementation)
μ_{smKT}	Kuster and Toksöz's shear modulus (Kuster and Toksöz, 1974)
μ_s	Grain rigidity
μ_h	Gas hydrate rigidity
$\mu_{sm} = (\mu_{smKT} - \mu_{sm0})[\emptyset_h/(1 - \emptyset_s)]^{3.8} + \mu_{sm0}$	Solid matrix shear modulus (percolation theory)
$\mu = (\emptyset_s + \emptyset_h)(\emptyset_s s_s/\mu_{sm} + s_h/\mu_h)^{-1}$	Average rigidity of the skeleton
k	Coupling factor

In order to estimate gas hydrate and free gas concentration, porosity and background velocity at full-water saturation should be known. In this study area, since no direct measurements for gas hydrate or free gas concentrations are available, it is difficult to determine the background velocity. Tinivella et al. (1998) compared the seismic velocity profiles in the area where the BSR is not present with the Hamilton (1976) velocities for normally compacted terrigenous sediments, and the comparison shows a good agreement. Therefore, the parameters versus depth (porosity, density, and compressibility) used to evaluate background velocity were taken from for Hamilton's dataset for terrigenous sediments (e.g., Tinivella and Accaino, 2000; Tinivella et al., 2002; Loreto et al., 2011).

The uncertainty in concentration estimation is mainly assessed in relation to the uncertainty in the seismic velocities, but also the errors in estimating the physical parameters used to calculate the reference velocities. Previous sensitivity tests performed in this area suggested that porosity is the most important parameter in the estimation of gas hydrate and free gas concentration, as a variation of ±5% in porosity can be translated into a variation of ±20% and ±7% of gas hydrate and free gas concentration, respectively (Tinivella et al., 2002).

4.4 Estimation of gas hydrate and free gas concentrations

4.4.1 Porosity estimation

The migrated section of line BSRstar8 shows an almost continuous BSR (see Figure 2.4) and we could not obtain velocity information in the region without BSR to compare with Hamilton's velocity. Moreover, the absence of BSR does not necessarily imply the absence of hydrates in the sediments. Thus, in order to have an idea about the region where gas hydrates may occur before concentration estimation and determine a more reasonable background velocity, we estimated porosity from the inverted P- and S-wave velocity fields considering the velocity errors, assuming no hydrate presence in the sediments, i.e. considering the regions where hydrate presence is not

expected. Then the estimated porosity profiles were compared with those calculated using Hamilton's equation for normally consolidated terrigenous sediments (Hamilton, 1976). If the maximum value of estimated porosity in the given layer is lower than Hamilton's porosity, this porosity difference is caused by the presence of gas hydrate in that layer. Figure 4.4 shows examples of comparison between the range of inverted porosity profiles and Hamilton's porosity profiles at the positions of two OBSs considering the velocity errors. The comparison indicates that the maximum values of inverted porosity in the first layer below the seafloor and the layer just above the BSR are still lower than Hamilton's porosity. This implies that gas hydrates may be present in the two layers. However, the maximum porosity of the middle layer shows higher value with respect to Hamilton's porosity, which may indicate no hydrate occurrence in this layer. Nevertheless, there is no evidence in the seismic data that supports the occurrence of gas hydrate in the layer just below the seafloor. Moreover, the velocity in the first layer is lower than Hamilton's velocity in normally consolidated terrigenous sediments (Hamilton 1976, 1979). So we suppose that there is also no presence of gas hydrate or free gas in the first layer below the seafloor. Based on the inverted porosity in the two layers below the seafloor, we extracted a porosity trend as a function of depth below the seafloor using a second-order polynomial fitting method. And then we used this trend to extrapolate the porosity for the layer just above and below the BSR. Figure 4.5 shows the porosity section that used to evaluate background velocity. The values of main parameters used to evaluate the velocity are shown in Table 4.2.

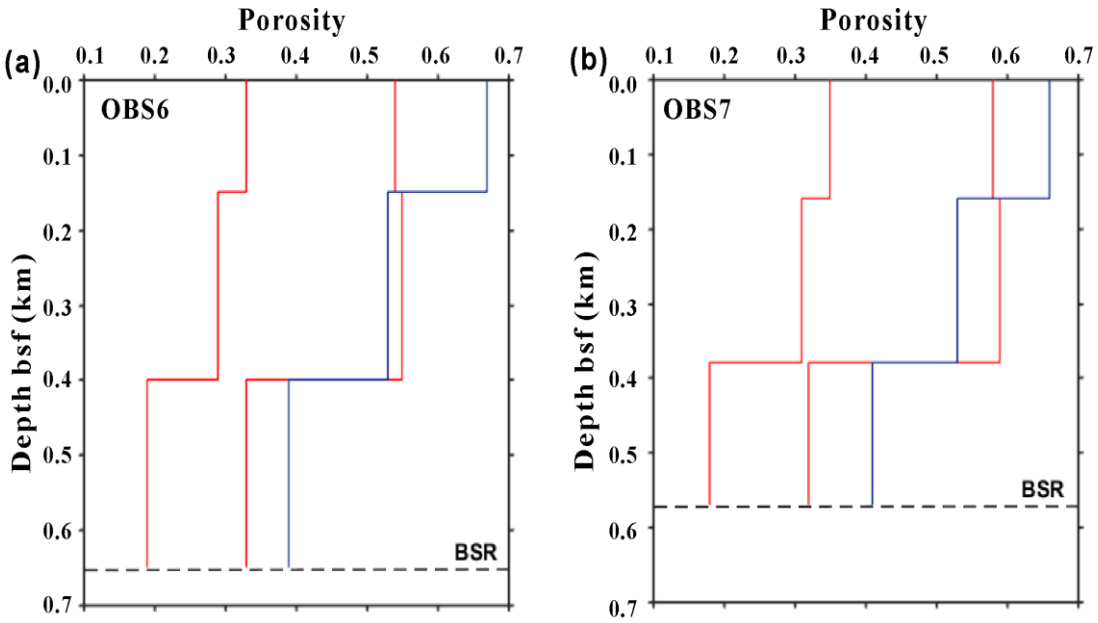

Figure 4.4: The porosity profiles extracted at the locations of OBS 6 (a) and OBS 7 (b). The two red lines indicate the range of porosity estimated from velocity fields. Hamilton porosity profiles are also shown (blue lines).

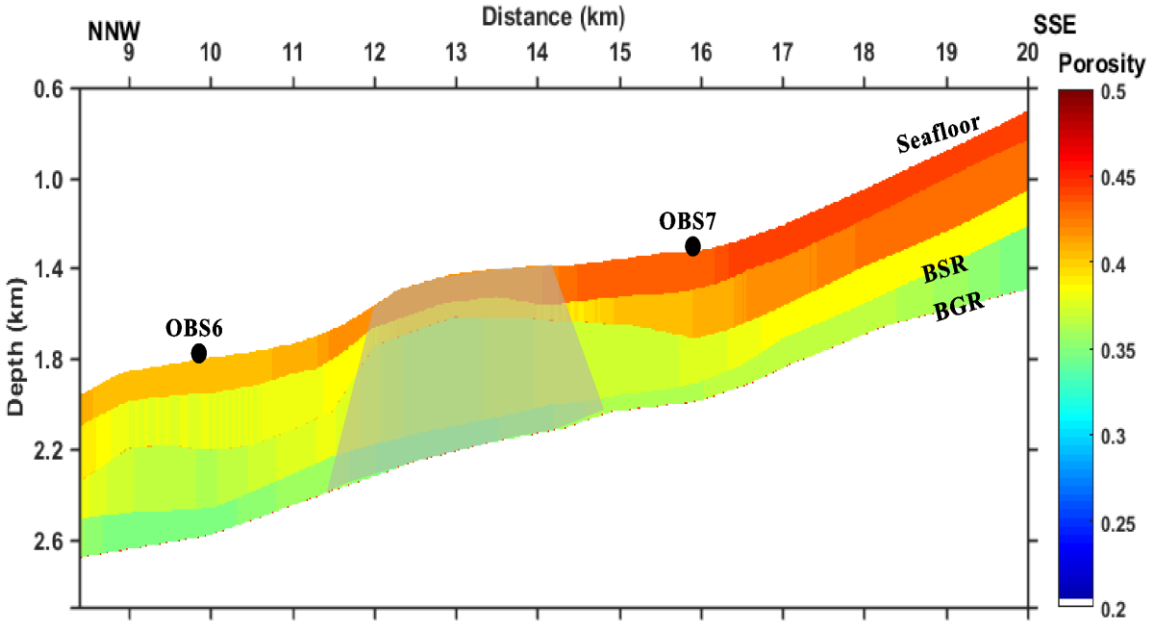

Figure 4.5: The porosity section determined by velocity fields.

Table 4.2 Values of main parameters used in equations (4.4) and (4.5) (from Tinivella et al., 2002)

C_s	0.027 $(Gpa)^{-1}$
C_h	0.119 $(Gpa)^{-1}$
C_w	0.44 $(Gpa)^{-1}$
C_g	42.4 $(Gpa)^{-1}$
ρ_h	920 kg/m^3
ρ_w	1040 kg/m^3
ρ_g	88.48 kg/m^3
μ_h	3.7 Gpa
k	150

4.4.2 Concentration estimation by using inverted porosity

The Poisson's ratio obtained from travel time inversion of converted S-waves was used to evaluate the rigidity of the sediments in each layer according to the following equation:

$$\mu = \rho {V_p}^2 (2\nu - 1)/(2\nu - 2) \tag{4.8}$$

where ρ is density, V_p is the reference velocity, and ν is the Poisson's ratio. Low P-wave velocity and low Poisson's ratio indicate that free gas is uniformly distributed in the pore space (Tinivella, 2002). A quantitative estimation was obtained by increasing the parameters in the theoretical model related to concentrations until the seismic velocity obtained from travel time inversion fitting the reference velocity (Figure 4.6). The gas hydrate and free gas concentration is shown in Figure 4.7; positive values are gas hydrate concentration, while the negative values are free gas concentration. The concentration was considered by percentage of total volume instead of pore space, which can provide information about the real gas amount due to its dependence on porosity (i.e. depth). The result shows that the gas hydrate concentration varies from 9% to 13% of total volume, and free gas

concentration is estimated in the range of 0.3% to 0.8% of total volume assuming a uniform distribution in the pore space.

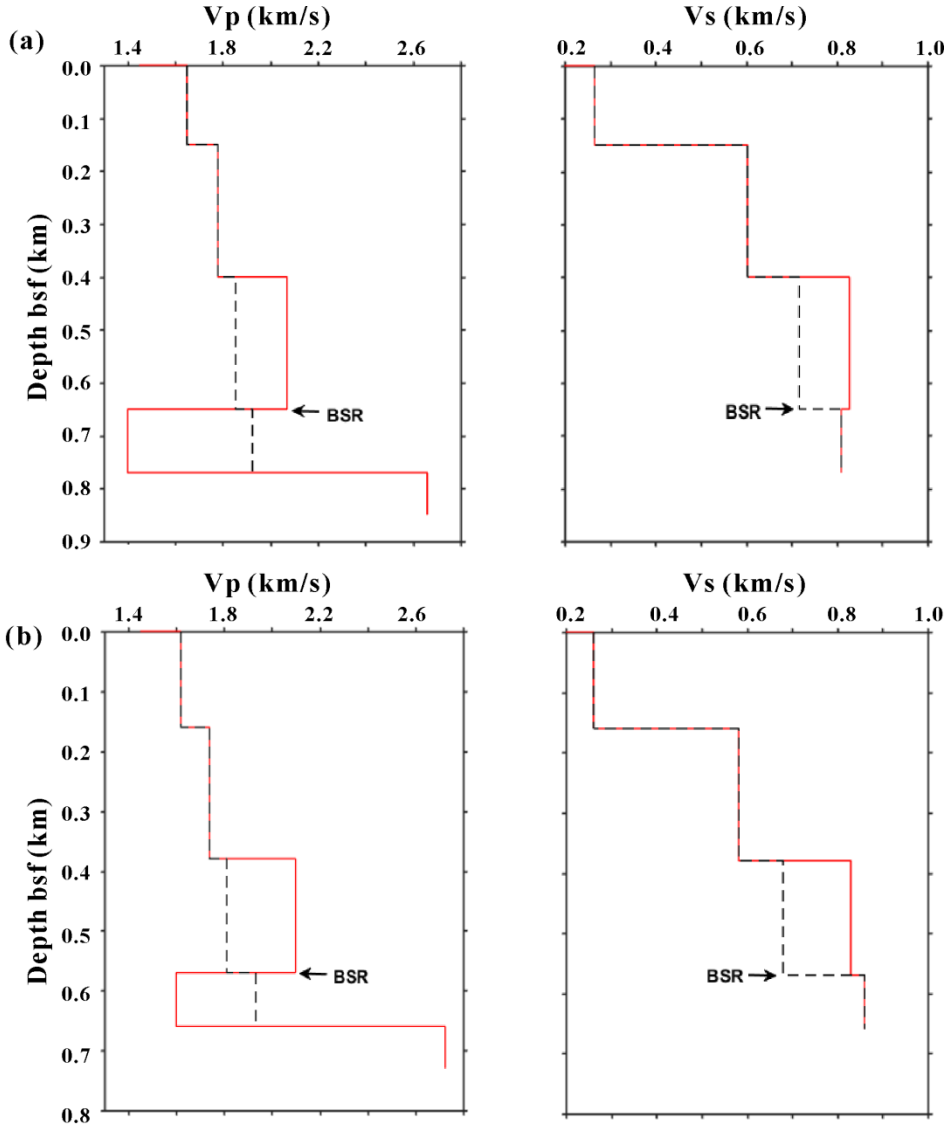

Figure 4.6: The seismic velocity profiles (red lines) after inversion and reference velocity curves (black dotted lines) extracted at the locations of OBS 6 (a) and OBS 7 (b).

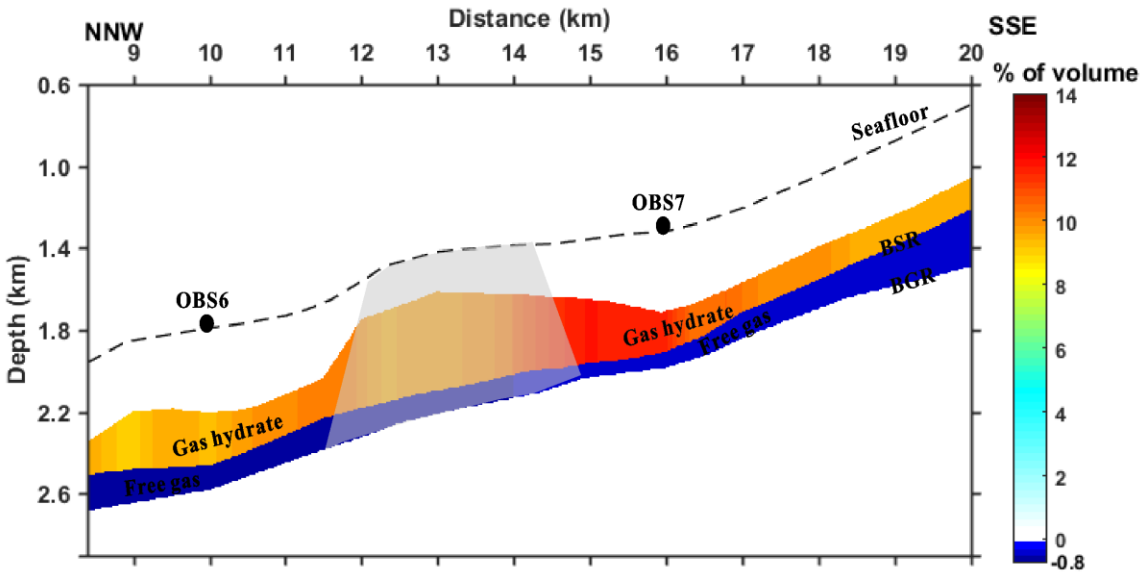

Figure 4.7: Concentration section of gas hydrate (positive values) and free gas (negative values) based on estimated porosity.

4.4.3 Concentration estimation by using Hamilton's porosity

The P-wave velocity in the first layer was obtained only from MCS data, which can provide a clear structural image but has limited source-receiver offsets and thus cannot provide accurate velocity information. Considering this, we deleted the first layer in the modified model (see Figure 3.14) and obtained a final velocity model that including two layers between the seafloor and the BSR (Figure 4.8). The first layer in the final P-wave model shows a velocity of 1.68-1.73 km/s and the layer just above the BSR has a high velocity of 2.0-2.1 km/s. Figure 4.9 shows the vertical profiles of P- and S-wave velocities and Poisson's ratio at the OBS locations. The S-wave velocity shows a continuous increase with depth and reaches a value of about 825 m/s at the BSR. Beneath the BSR, no significant increase or decrease was found, as the S-wave velocity is insensitive to pore fluid saturation. For each OBS, the Poisson's ratio shows a relatively continuous decrease with depth down to BSR and a strong decrease in the free gas layer below the BSR. Moreover, the Poisson's ratio is similar within each layer. In the layer just above the BSR, a value of 0.405 ±

0.012 and 0.409 $\pm$0.012 was observed at the OBS 6 and OBS 7 respectively; in the free gas layer, a Poisson's ratio equal to 0.25 $\pm$0.04 and 0.29 $\pm$0.04 was obtained, respectively.

Considering the high uncertainty in the porosity estimation, the physical parameters (porosity, density, compressibility) adopted for evaluating the reference velocities were taken from Hamilton's dataset for normally compacted terrigenous sediments. Figure 4.10 shows the gas hydrate and free gas concentration estimated by comparing the P-wave and S-wave velocity anomalies with the reference velocities. The gas hydrate concentration varies from 3% to 7% of volume in the first layer below the seafloor, while it is in the range of 10% to 15% of volume in the layer just above the BSR. The free gas concentration is estimated in the range of 0.3% to 0.8% of volume. The high concentration value was observed behind in the range of OBS 7 and this trend shows the same trend as the velocity model. The main sources of error in the estimated concentration of gas hydrate and free gas are related to the velocity errors and the errors of the physical parameters used to calculate the theoretical velocities. Because the relationship between velocity and gas-phase concentration is not linear, we recalculated the gas hydrate and free gas concentration based on the estimated errors in the P- and S-wave velocity. Considering the errors related to assumed physical parameters (Tinivella et al., 2002) and the estimated velocity errors (Table 4.3), we can suppose the errors in the estimation of gas hydrate and free gas concentration are about 5% and 0.3% of total volume, respectively.

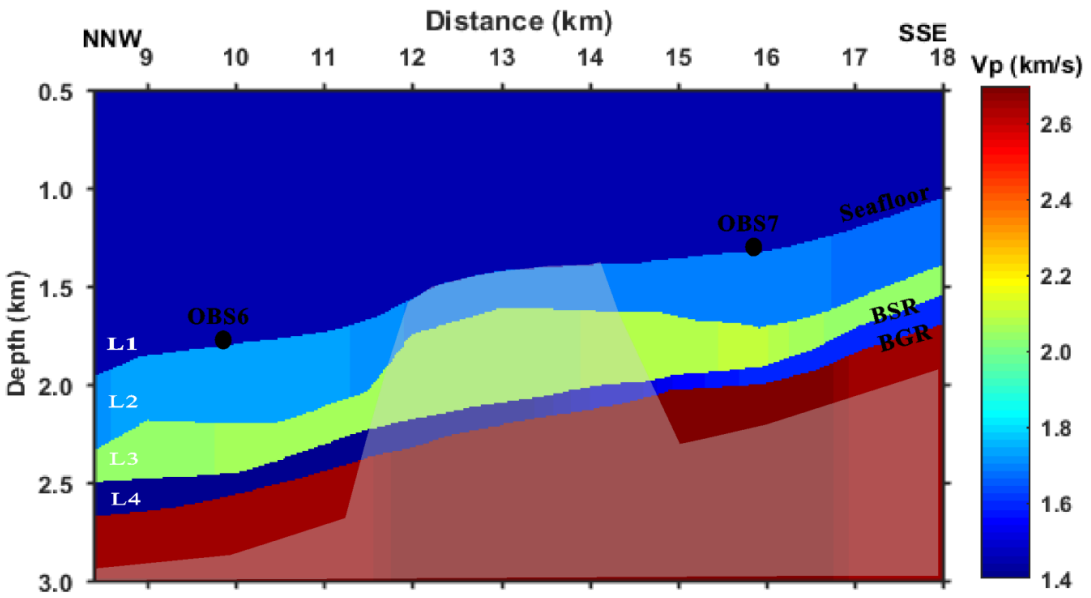

Figure 4.8: The final P-wave velocity model obtained after travel time inversion of MCS and OBS data.

Table 4.3 Percentage errors of P-wave and S-wave velocities in the final model

Layer	Error in Vp (%)			Error in Vs (%)		
	Projection error	**Inversion error**	**Total error**	**Projection error**	**Inversion error**	**Total error**
L1	NO	1	1	NO	NO	NO
L2	2	5	7	2	4	6
L3	1	7	8	1	7	8
L4	1	7	8	1	9	10

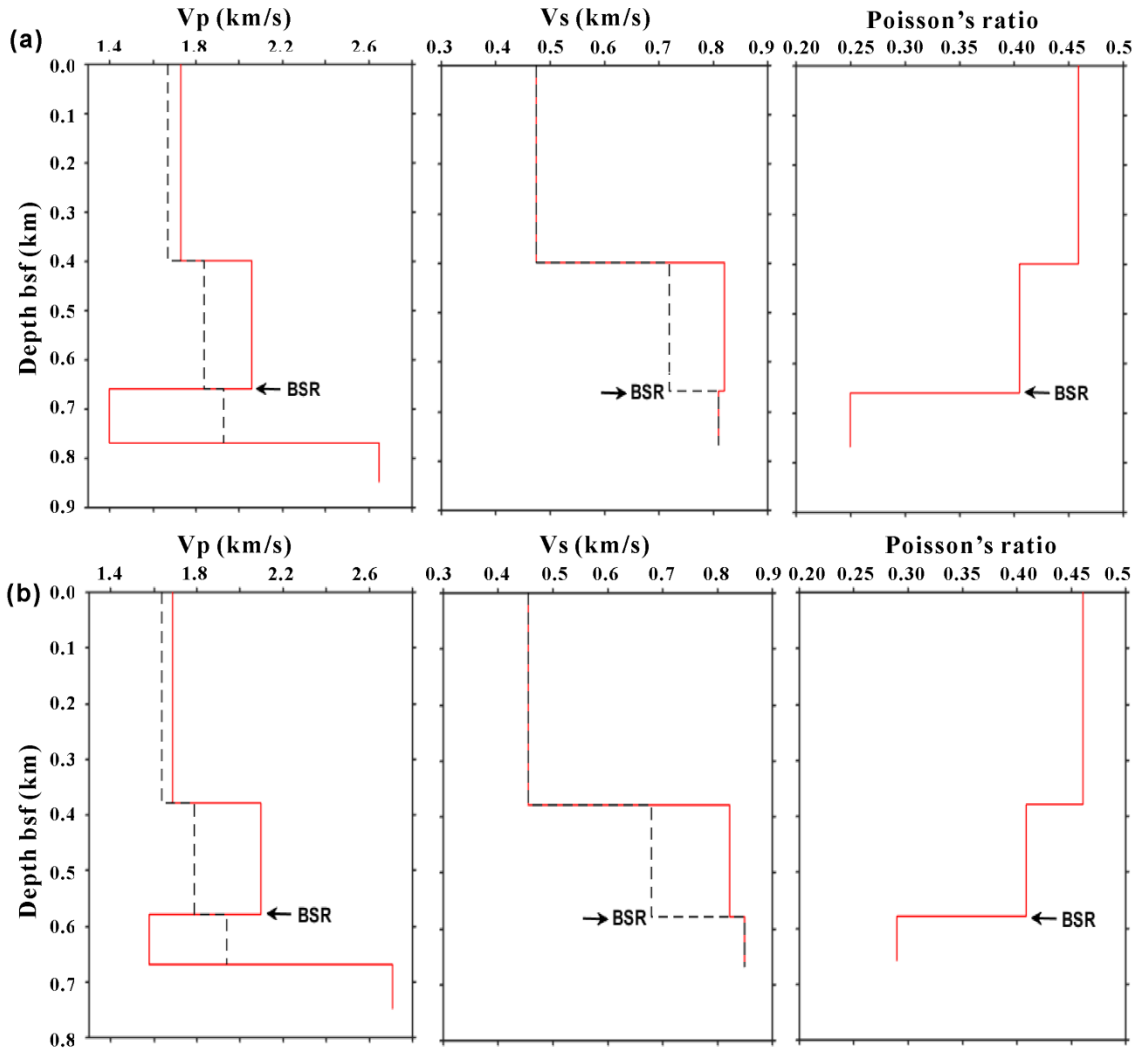

Figure 4.9: The final seismic velocity profiles (red lines) after inversion and reference velocity curves (black dotted lines) and Poisson's ratio profiles extracted at the locations of OBS 6 (a) and OBS 7 (b).

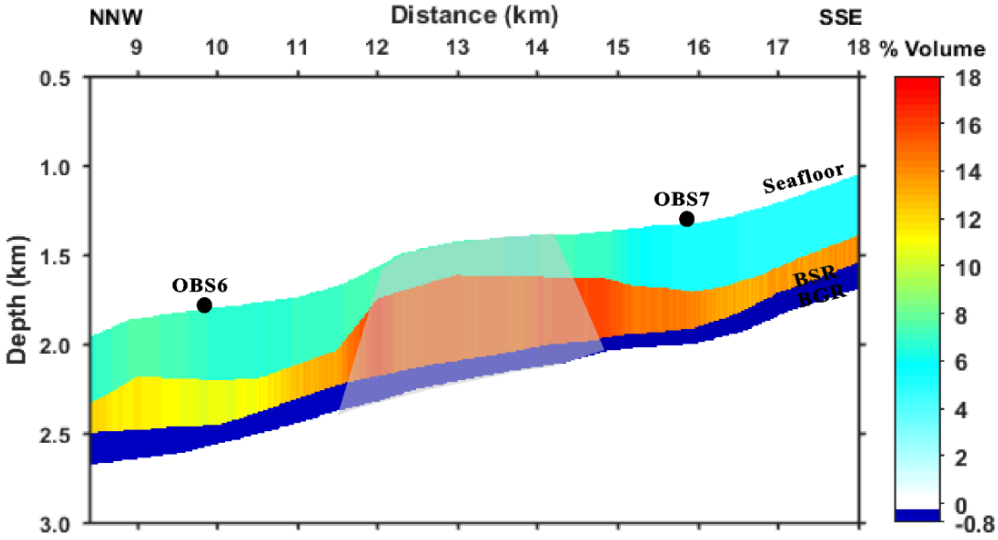

Figure 4.10: Concentration section of gas hydrate (positive values) and free gas (negative values) based on Hamilton's porosity.

4.5 Summary

The P- and S-wave velocity fields obtained from travel time inversion were used to estimate gas hydrate and free gas concentrations based on a modified Biot-Geerstma-Smit theory. As no direct measurements are available, in order to determine more reasonable reference velocities, we tested two porosity models. One is estimated from inverted velocity fields assuming no hydrate presence in the sediments, and another is Hamilton's porosity for normally consolidated terrigenous sediments. The two porosity models produced similar concentration in the layer just above and below the BSR. Considering the high uncertainty in the shallow layer of velocity model and thus estimated porosity model, finally, the Hamilton's porosity was chosen and the final velocity model including two layers above the BSR, and one layer below the BSR, was obtained.

Chapter 5

Discussion

5.1 BSR analysis

Around Antarctica, the presence of BSRs related to diagenetic alteration of biogenic silica, in particular, Opal-A to Opal-CT, has been recognized in the South Orkney microcontinent (e.g., Lonsdale, 1990), the sedimentary drifts of the Antarctic Peninsula continental rise (e.g., Rebesco et al., 1996; Volpi et al., 2003), the Prydz Bay continental slope (e.g., Claypool et al., 2003) and the central and southern Scotia Sea (e.g., Somoza et al., 2014).

As mentioned in section 2.2, the migrated section of MCS line BSRstar8 shows that the BSR mimics the seafloor topography and has the reverse polarity with respect to the seafloor reflection; the BSR's cross-cutting behavior is especially clear towards the northwestern part of MCS line. The BSR becomes deeper to the NNW with increasing water depth. Its depth is about 510-650 m below the seafloor (Figure 4.8). Moreover, the low velocity is observed in the layer below the BSR. These characters suggest that the BSR is related to a gas hydrate reservoir rather than the opal transformation.

To verify this interpretation, we also calculated the theoretical depth of the base of gas hydrate stability zone. Previous studies indicate that the regional geothermal gradient in this study area is about 37.5 ℃/km (Loreto et al., 2011). The theoretical BSR depth was calculated using phase boundary diagram of Sloan (1998) based on the following information: sea water depth from the bathymetry, sea bottom temperature equal to 0.4 ℃ from CTD data (Giustiniani et al., 2008), geothermal gradient, and gas composition (90% methane, 5% ethane and 5% propane) as indicated by core analysis (Tinivella et al., 2008). The BSR depth obtained from the velocity model along MCS line BSRstar8 matched well with the theoretical BSR depth considering a constant geothermal gradient (Figure 5.1). It is comparable to the depth (about 600 m below the seafloor) of BSR in a

similar water-depth dependence, which was the firstly identified BSR produced by the presence of gas hydrates in the South Shetland margin (Lodolo, 1993; Tinivella et al., 1998).

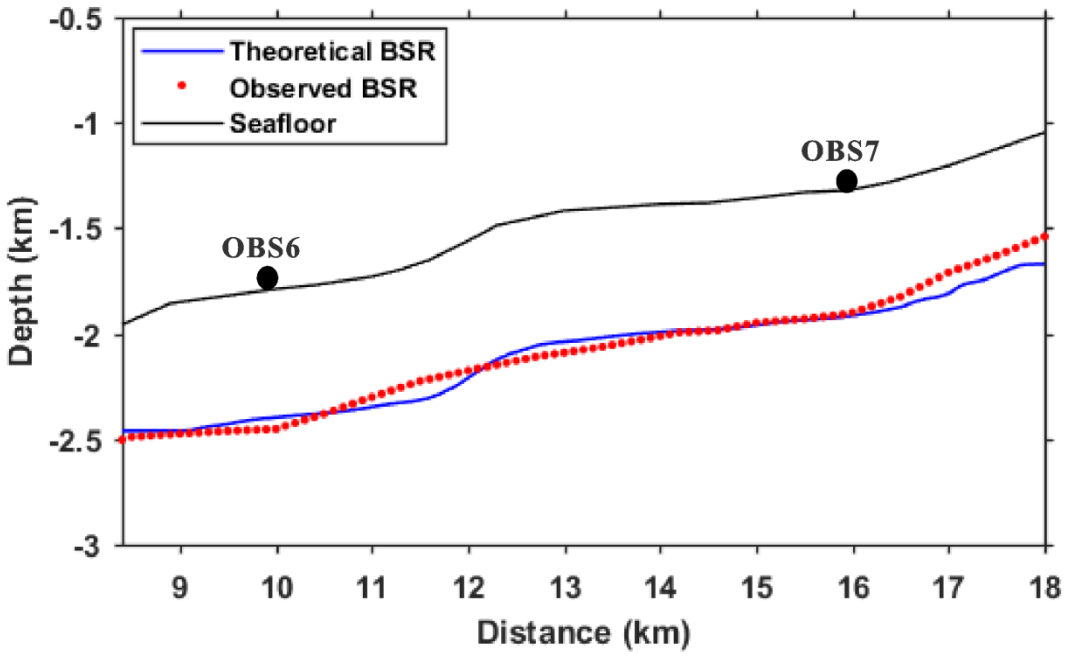

Figure 5.1: The theoretical (blue line) and observed (red dotted line) BSR depths. The theoretical BSR depth was calculated using a geothermal gradient of 37.5 ℃/km.

Generally, the opal-A/CT BSR is at greater depth than the hydrate-related BSR because it develops at high temperature of about 35-50 ℃. We also estimated the temperature of BSR assuming a geothermal gradient of 37.5 ℃/km. For a given geothermal gradient, the temperature T at depth z is given by $T(z) = (dT/dz)z$. The sea bottom temperature equal to 0.4 ℃ was adopted. The estimated temperature range for the BSR varies between 19 ℃ and 25 ℃. This low temperature implies that the BSR is too shallow to be interpreted as produced by opal-A/CT transition and excludes a diagenetic origin.

Considering a geothermal gradient of 37.5 ℃/km, if the Opal-A/Opal-CT occurs, it would be located at deeper than 920 m below the seafloor. Several reflections with normal polarity can be observed below the BSR on the MCS seismic section (Figure 2.4), but they do not show clear, continuous, and cross-cutting characters. In addition, their amplitudes are weaker compared to the BSR and they could not be identified on the OBS data. Considering the complex geological setting

of this study area and lack of enough information, at this stage, we could not provide a conclusive answer for the occurrence of diagenesis-related BSR below the gas hydrate stability zone.

5.2 Comparison with previous results

5.2.1 Velocity model

The final velocity model obtained from the travel time inversion of OBS data is comparable with previous study performed on another OBS station (Tinivella and Accaino, 2000) that was deployed more than 40 km far from the analyzed OBSs (see the location in Figure 2.1). Previous velocity model shows a P-wave velocity of 2.0-2.3 km/s in the gas hydrate layer and 1.2-1.5 km/s in the free gas layer. The Poisson's ratio is also in good agreement with the previous result, indicating a Poisson's ratio of 0.405 in the hydrate-bearing sediments and 0.25 in gas-bearing sediments. This agreement implies that the Poisson's ratio is fairly uniform and the gas hydrate reservoir does not show significant variations in this study area.

The P-wave velocity field is also comparable with other studies in this area performed on multichannel seismic data by travel time inversion or pre-stack depth migration tool. For example, Tinivella et al. (2002) obtained an interval velocity of 2.0-2.25 km/s and 1.6 km/s in gas hydrate and free gas layer respectively, in the accretionary prism sediments.

5.2.2 Gas hydrate and free gas concentrations

(1) Concentrations in the upmost layer

The positive velocity anomalies in the upmost layer (layer L2) below the seafloor yielded the gas hydrate concentration of about 3% - 7% of total volume. It is comparable with the previous studies of Tinivella et al. (2009), who obtained an average hydrate concentration 5.8% $\pm$ 1.2% of total volume in the first 250 m below the seafloor, supposing that high velocity is related to the presence of gas hydrates. They also suggested another possible explanation: shallow high velocity is related to the presence of biogenic silica (Opal-A) in low concentration. Considering the error (~5%) of gas hydrate concentration, our concentration in the first layer below seafloor may be close to 0, which means that gas hydrates probably are not present, or we can consider the presence of biogenic silica in the sediments. Therefore, we suppose that there is no hydrates occurrence in the layer just below the seafloor. This result also agrees with other studies (e.g., Tinivella et al., 2002; Loreto and Tinivella, 2012).

In order to further verify the absence of gas hydrates near the seafloor, we calculated the seafloor reflection coefficients using chirp data that produce high-resolution images of near-surface. The analysis of seafloor reflection coefficients is useful tool for investigating the spatial variation of acoustic properties for the sediment immediately below the seafloor, and can be used to identify slides and fluid expulsions related to gas hydrate dissociation. Figure 5.2 shows the location of chirp profiles. We extracted amplitude information of seafloor along all the chirp profiles. The reflection coefficients were calculated based on the amplitudes of the seafloor multiple and the seafloor primary reflection using the following equation (Bull et al., 1998):

$$R_{SF} = \frac{TWT_m}{TWT_p} \cdot \frac{A_m}{A_p} \tag{5.1}$$

where R_{SF} is seafloor reflection coefficient, A_m and A_p are the amplitudes of the first seafloor multiple and seafloor primary, and TWT_m and TWT_p are the corresponding two-way times.

Since the chirp data are noisy, the calculated reflection coefficients were smoothed based on a moving-average method in order to extract the normal trend. Figures 5.3 and 5.4 show examples of two chirp profiles and their reflection coefficients. Then the reflection coefficients obtained along all the chirp profiles were interpolated by using the Surfer software in order to create a 3D seafloor reflectivity map (Figure 5.5). The interpolation was based on the Inverse Distance Weighted (IDW) method and the output map has a cell grid size of 400 m × 400 m.

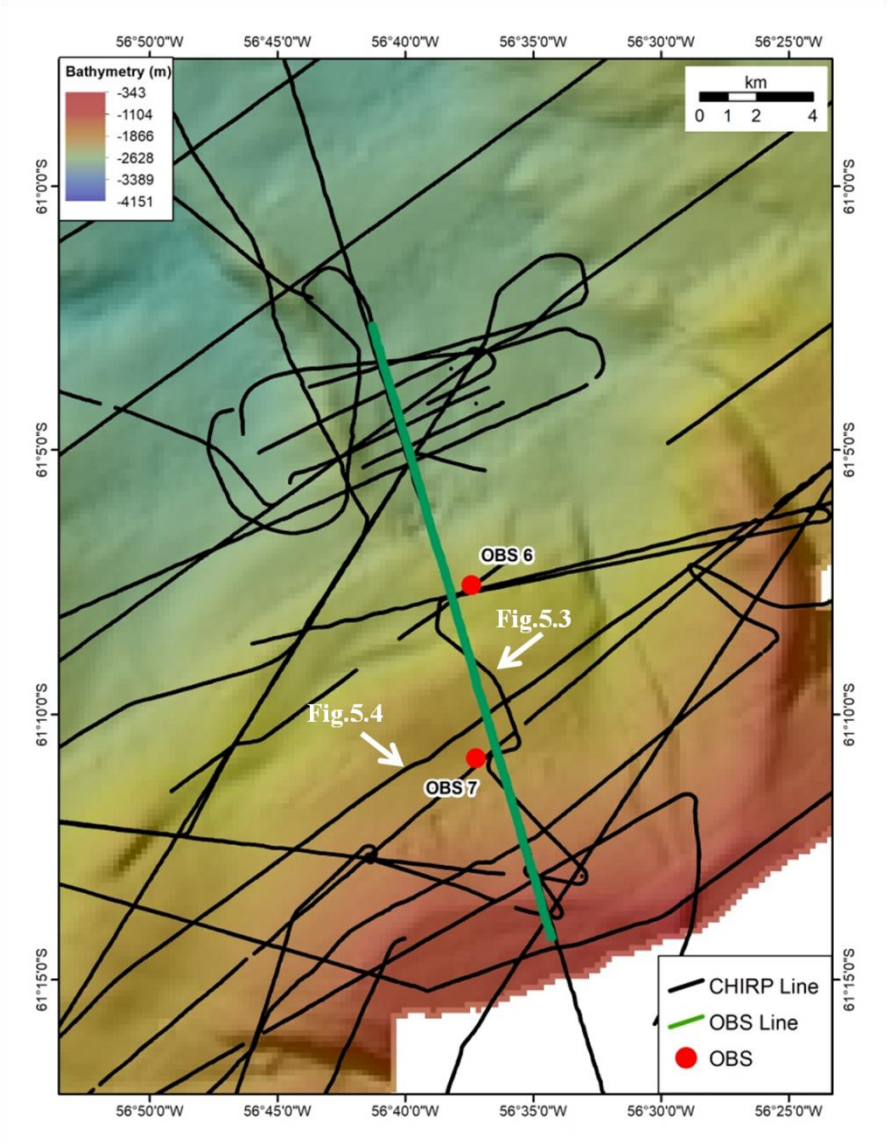

Figure 5.2: Bathymetric map showing the locations of chirp profiles (black lines). The red circles indicate the locations of two OBSs; the green line marks the shot line of OBSs. The white arrows indicate the locations of chirp profiles shown in Figures 5.3 and 5.4.

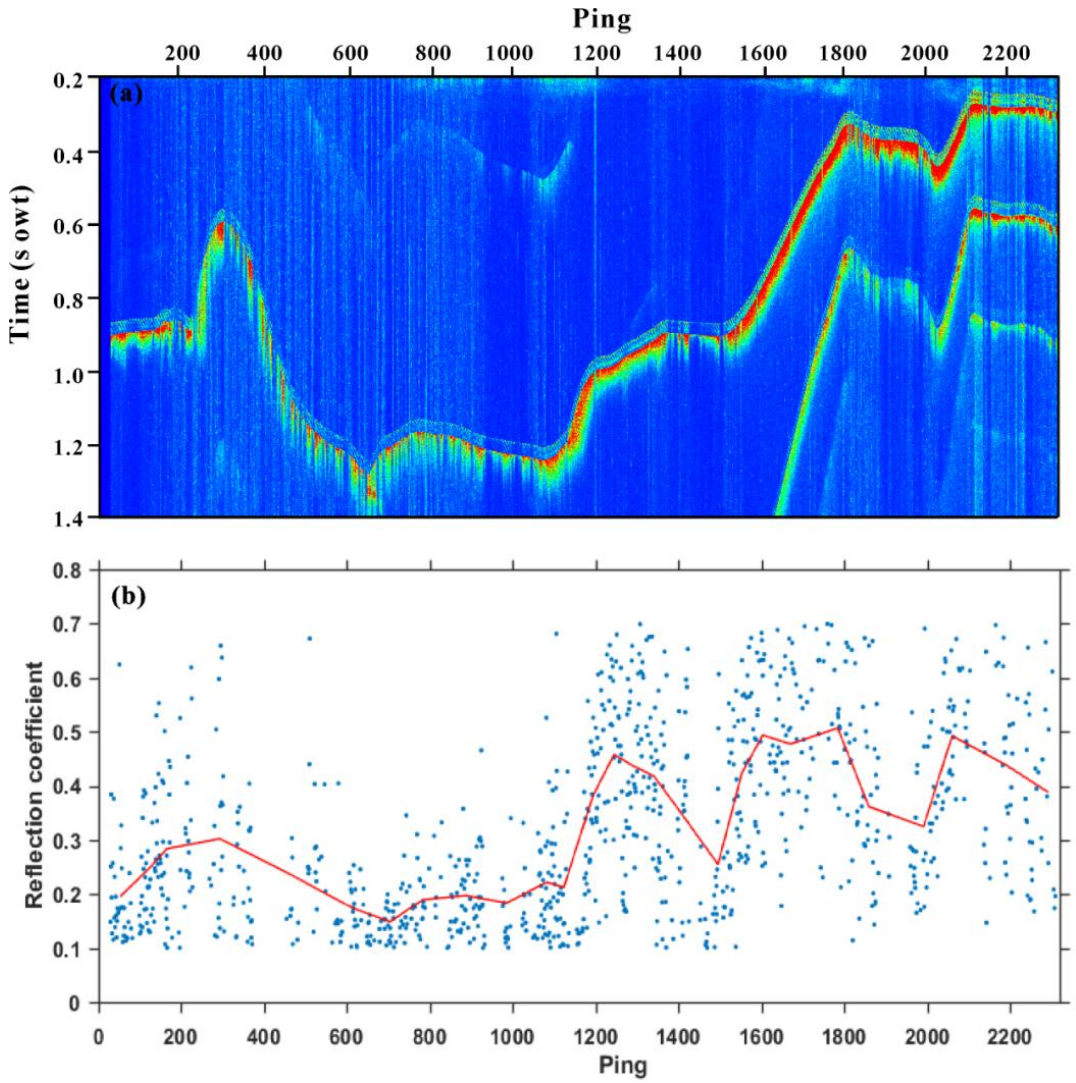

Figure 5.3: (a) Example of chirp profile 43. The location of this profile is indicated in Figure 5.2; (b) Seafloor reflection coefficient (blue dots) obtained from this chirp profile. The red line indicates the trend of reflection coefficient after smoothing.

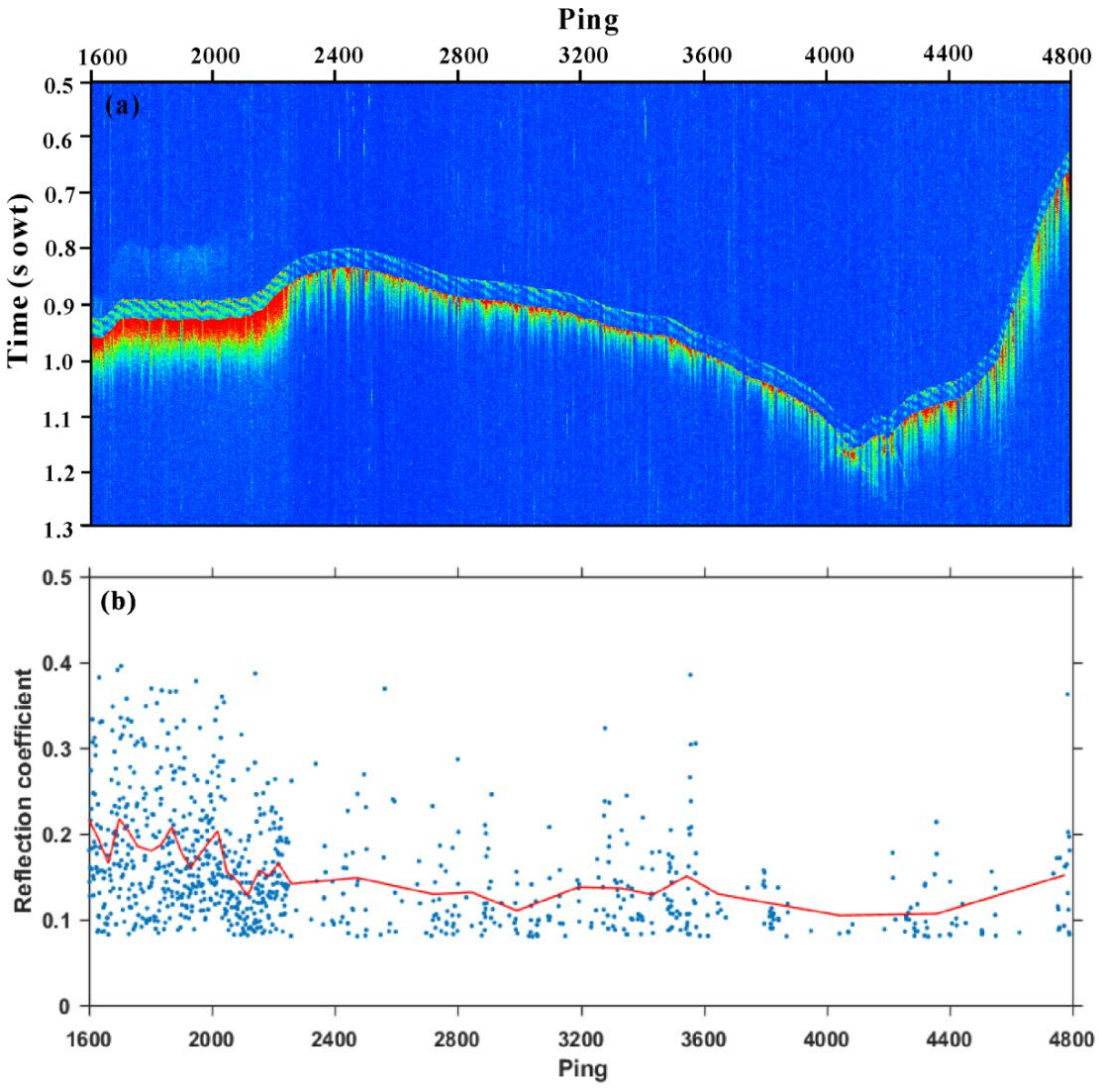

Figure 5.4: (a) Example of chirp profile 29. The location of this profile is indicated in Figure 5.2; (b) Seafloor reflection coefficient (blue dots) obtained from this chirp profile. The red line indicates the trend of reflection coefficient after smoothing.

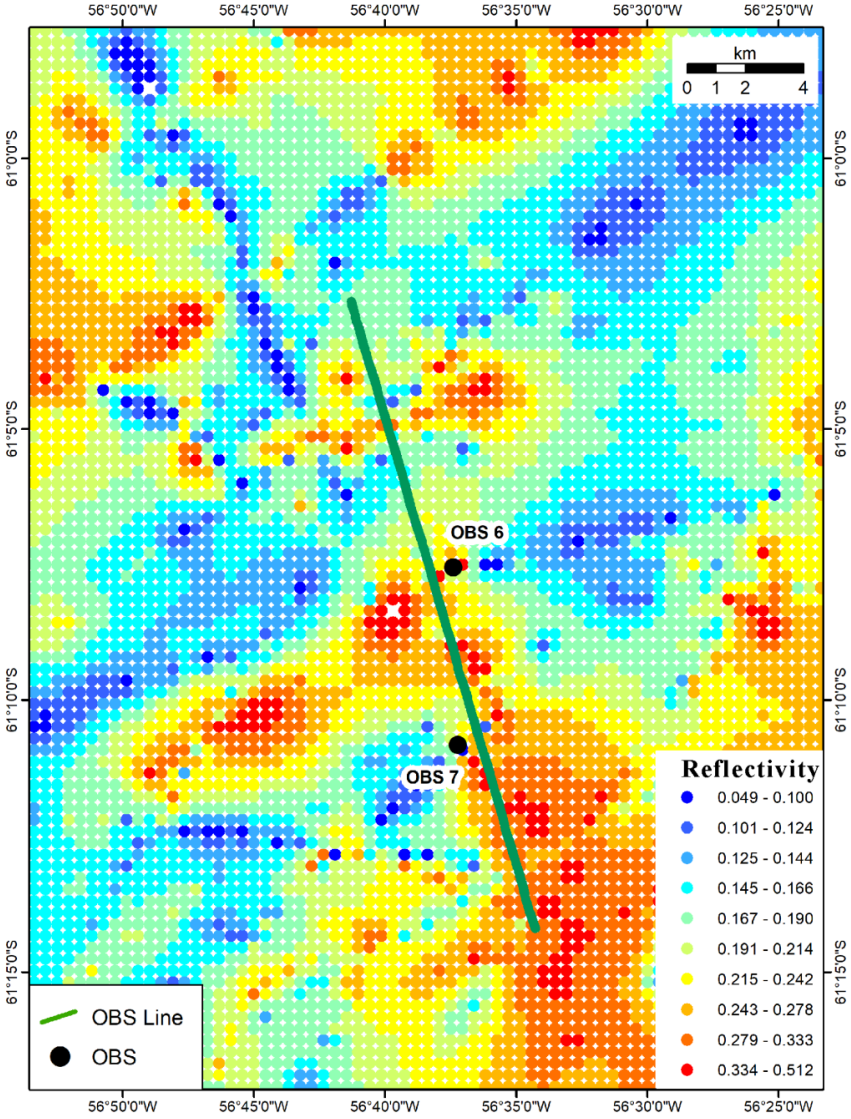

Figure 5.5: Seafloor reflectivity map derived from chirp data.

We also determined seafloor reflection coefficients using data from two OBSs. The maximum absolute amplitudes of the direct wave and the seafloor multiple were plotted against shot, and then the ratio of amplitudes for each shot was calculated separately (Warner, 1990). A spherical divergence correction was applied to OBS data before this calculation. In order to compare the reflection coefficients obtained from OBS data with those obtained from chirp data, we extracted the values of reflection coefficient from the interpolated reflectivity map along the OBS shot line and plotted them in one figure (Figure 5.6). Table 5.1 shows the average value of reflection coefficient and standard deviation. The reflection coefficient obtained from OBS data seems show

the variation on the left and right side of OBS, but this is believed to be related to the quality of the data. If we consider the reflection coefficients at near offset of OBSs, a similar trend with that from chirp data can be seen. The average reflection coefficient was calculated from chirp data to be 0.23 with a standard deviation of 0.051.

The seafloor reflection coefficient does not show significant variation along the shot line of OBSs, which can indicate that there is probably no presence of gas hydrates or free gas at the seafloor. But the analysis of seafloor reflection coefficients is not enough to confirm this possibility. Other information such as fluid-flux measurements are needed, which are not available in this area.

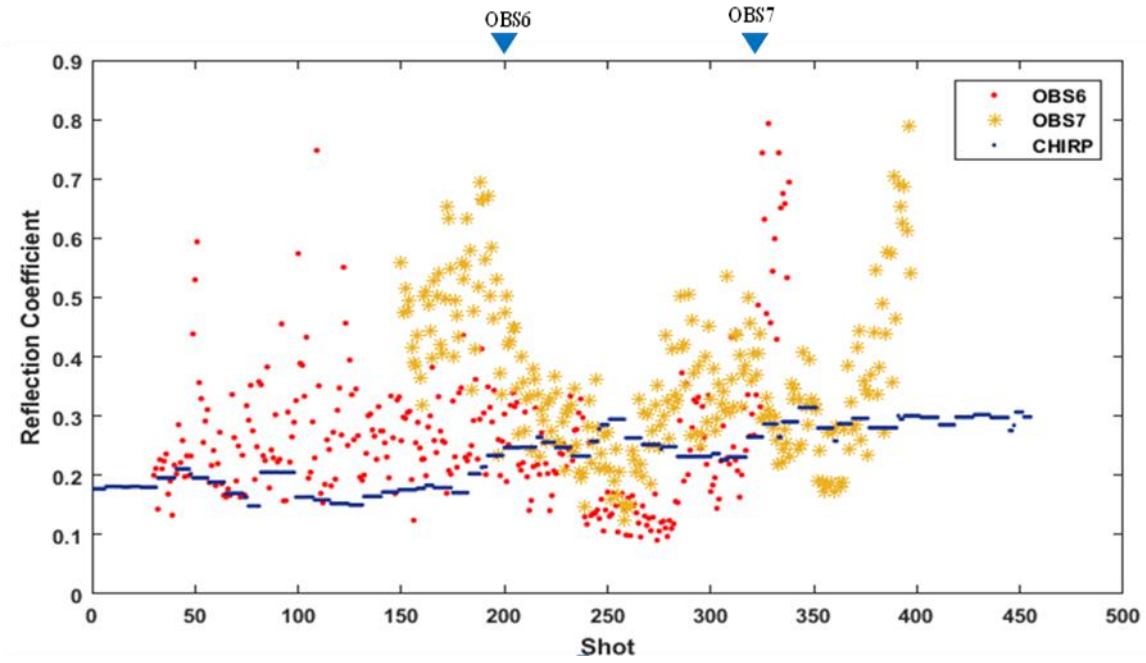

Figure 5.6: Seafloor reflection coefficients obtained from OBS 6 (red dots), OBS 7 (yellow stars), and chirp data (blue bars). The projected positions of two OBSs on the shot line were indicated as triangles.

Table 5.1 Average reflection coefficient at the seafloor obtained from chirp and OBS data

	OBS6	**OBS7**	**Chirp**
Average R_{SF}	0.26 ± 0.120	0.34 ± 0.129	0.23 ± 0.051

(2) Concentrations in the layer just above and below BSR

The estimated gas concentration is in the range of 10% to 15% (±5%) of total volume in the layer just above the BSR, and free gas concentration is estimated in the range of 0.3% to 0.8% (±0.3%) of total volume assuming a uniform distribution in the pore space. Our estimates are comparable with previous studies in this area by other authors. For example, recent studies of Loreto and Tinivella (2012) estimated maximum hydrate concentration of 16% of total volume along the syncline structure. Tinivella et al. (2009) obtained an average concentration of 17.7% and 0.3% of total volume in the case of gas hydrate and free gas respectively from MCS data analysis. In an earlier study, an average hydrate concentration of 6.0% ± 1.2% of total volume was estimated in the accretionary prismby based on MCS data (Tinivella et al., 2002). If we consider the gas hydrate concentration in percentage of pore space, it is equal to about 23% to 35% of pore space, which agrees with the value (23% of pore space) obtained from another OBS analysis by Tinivella and Accaino (2000).

5.3 Implications of the study

In this thesis, the detailed processing and analysis of multi-component OBS data were presented, in particular, OBS preprocessing, P- and S-wave velocity modeling, velocity error analysis, and concentration estimation, which can be considered as useful approach for the geophysical characterization of gas hydrate systems. The results of this study contribute to a better understanding of the gas hydrate system in the South Shetland margin, particularly on the aspect of petrophysical properties. The analysis of OBS data has enabled to obtain the information of both P- and S-wave velocity fields of the subsurface and it provides new insights into the distribution and quantification of gas hydrate and free gas in marine sediments in the South Shetland margin. The relatively uniform Poisson's ratio of gas hydrate reservoir can provide an additional clue for

evaluating the rigidity of sediment and thus a reliable concentration when no well data are available. The high concentrations of gas hydrate and free gas suggest that they could be considered as future energy source. This study can also provide a valuable contribution to the investigation of relationship between gas hydrate stability and climate change as the polar areas are the most sensitive to global change.

Chapter 6

Conclusions

This thesis presents a characterization of gas hydrate systems in the South Shetland margin based on the integrated analysis of geophysical data, including multichannel seismic, wide-angle OBS, bathymetry and sub-bottom chirp data acquired in 2004. The main focus is to define distribution and concentration of gas hydrate and free gas and to investigate petrophysical properties of gas hydrate systems in this study area. Travel time inversion performed on OBS data provides detailed P- and S-wave velocity information of the subsurface allowing obtaining a reliable estimate of gas hydrate and free gas concentrations. The estimated concentrations based on a modified Biot theory are comparable with previous studies in the study area (Song et al., 2018; Appendix 1).

The main conclusions from this study are summarized as follows:

(1) Velocity model obtained from travel time inversion indicates that the BSR is located at the depth of 510-650 m below the seafloor, which matches well with the theoretical BSR depth.

(2) We observe a high P-wave velocity layer of 2.0-2.1 km/s just above the BSR, which can be associated to the presence of gas hydrates. The gas hydrate concentration in this layer is about 10% to 15% of total volume.

(3) We observe a low velocity layer at 1.4-1.6 km/s (P-wave velocity) below the BSR, which indicates the presence of free gas. The base of free gas layer occurs at a depth varying between 80-160 m below the BSR. The free gas concentration is estimated in the range of 0.3% to 0.8% of total volume, assuming a uniform distribution of free gas in the pore space.

(4) The Poisson's ratio obtained by forward modeling of converted S-waves from OBS data is in good agreement with previous study performed in this area. This comparison allows us to conclude that the gas hydrate reservoir in this study area shows no significant regional variations from a petrophysical point of view.

References

Andreassen, K., Berteussen, K.A., Sognnes, H., Henneberg, K., Langhammer, J., Mienert, J., 2003. Multicomponent ocean bottom cable data in gas hydrate investigation offshore of Norway. J. Geophys. Res. 108(B8), 2399.

Archer, D., Buffett, B., Brovkin, V., 2009. Ocean methane hydrates as a slow tipping point in the global carbon cycle. Proc. Natl Acad. Sci. USA. 106 (49), 20596–20601.

Berndt, C., Bünz, S., Clayton, T., Mienert, J., Saunders, M., 2004. Seismic character of bottom simulating reflectors: Examples from the mid-Norwegian margin. Mar. Petrol. Geol. 21 (6), 723–733.

Bonilla, L.L., Keller, J.B., 1985. Acoustic elastic effect and wave propagation in heterogeneous weakly anisotropic materials. J. Mech. Phys. Solids. 33, 241–261.

Boswell, R., Collett, T.S., 2011. Current perspectives on gas hydrate resources. Energy Environ. Sci. 4, 1206–1215.

Botz, R., Bohrmann, G., 1991. Low-temperature opal-CT precipitation in Antarctic deep-sea sediments: evidence from oxygen isotopes. Earth Planet. Sc. Lett. 107(3-4), 612–617.

Brooks, J.M., Cox, H.B., Bryant, W.R., Kennicutt, M.C., Mann, R.G., Mc Donald, T.J., 1986. Association of gas hydrates and oil seepage in the Gulf of Mexico. Org. Geochem. 10, 221–234.

Bünz, S., Mienert, J., Vanneste, M., Andreassen, K., 2005. Gas hydrates at the Storegga Slide: constraints from an analysis of multi-component, wide-angle seismic data. Geophysics, 70, B19–B34.

Bull, J.M., Quinn, R., Dix, J.K., 1998. Reflection coefficient calculation from marine high resolution seismic reflection (Chirp) Data and application to an archaeological case study. Mar. Geophys. Res. 20, 1–11.

Carcione, J.M., Tinivella, U., 2000. Bottom-simulating reflectors: Seismic velocities and AVO effects. Geophysics, 65 (1), 54–67.

Carcione, J.M., Gei, D., 2004. Gas hydrate concentration estimated from P- and S-wave velocities at the Mallik 2L-38 research well, Mackenzie Delta, Canada. J. Appl. Geophys. 56 (1), 73–78.

Cerveny, V., Molotkov, I., Psencik, I., 1977. Ray Method in Seismology. University of Karlova, Prague.

Chamley, H., 1997. Clay mineral sedimentation in the ocean. In: Paquet, H., Clauer, N. (Eds.), Soils and Sediments, Mineralogy and Geochemistry, Springer, Berlin, p. 269–302.

Chand, S., Minshull, T.A., Gei, D., Carcione, J., 2004. Elastic velocity models for gas-hydrate-bearing sediments— a comparison. Geophys. J. Int. 159, 573–590.

Claypool, G.E., Lorenson, T.D., Johnson, C.A., 2003. Authigenic carbonates, methane generation, and oxidation in conti-nental rise and shelf sediments, ODP Leg188 Sites 1165 and 1166, Offshore Antarc-tica (Prydz Bay). Proc. Ocean Drill. Program Sci. Results, 188, 15 pp.

Cohen, J.K., Stockwell, J.W., 2008. CWP/SU: Seismic Unix Release 4.0: A free Package for Seismic Research and Processing; Center for Wave Phenomena, Colorado School of Mines: Golden, CO, USA, pp. 1–153.

Collett, T., Riedel, M., Cochran, J., Boswell, R., Presley, R., Kumar, P., Sathe, A., Sethi, A., Lall, M., Sibal, V.K. and NGHP Expedition 01 Scientists, 2008. NGHP Expedition 01 (2006), Initial Reports, Directorate General of Hydrocarbons, Noida and Ministry of Petroleum & Natural Gas, India. 4 volumes.

Collett, T.S., Johnson, A.H., Knapp, C.C., Boswell, R., 2009. Natural Gas Hydrates: A Review, in Collett, T., Johnson, A., Knapp, C., Boswell, R. (Eds.), Natural gas hydrates—Energy resource potential and associated geologic hazards. AAPG Mem. 89, pp. 146–219.

Collett, T.S., 2002. Energy resource potential of natural gas hydrates. AAPG Bull. 86(11), 1971–1992.

Crutchley, G.J., Maslen, G., Pecher, I.A., Mountjoy, J.J., 2016. High-resolution seismic velocity analysis as a tool for exploring gas hydrate systems: An example from New Zealand's southern Hikurangi margin. Interpretation, 4(1), SA1–SA12.

Cui, Y., Lu, C., Wu, M., Peng, Y., Yao, Y., Luo, W., 2018. Review of exploration and production technology of natural gas hydrate. Advances in Geo-Energy Research, 2(1), 53–62.

Cygan, R.T., Guggenheim, S., Koster van Groos, F., 2004. Molecular models for the intercalation of methane hydrate complexes in montmorillonite clay. J. Phys. Chem. B. 108, 15141–15149.

Dai, J., Xu, H., Snyder, F., Dutta, N., 2004. Detection and estimation of gas hydrates using rock physics and seismic inversion: Examples from the northern deepwater Gulf of Mexico. Lead. Edge. 23 (1), 60–66.

Dash, R., Spence, G.D., 2011. P-wave and S-wave velocity structure of northern Cascadia margin gas hydrates. Geophys. J. Int. 187, 1363–1377.

Davies, R.J., 2005. Differential compaction and subsidence in sedimentary basins due to silica diagenesis: A case study. Geol. Soc. Am. Bull. 117, 1146–1155.

Dickens, G.R., O'Neil, J.R., Rea, D.K., Owen, R.M., 1995. Dissociation of oceanic methane hydrate as a cause of the carbon isotope excursion at the end of the Paleocene. Paleoceanography, 10, 965–971.

Dietrich, R., Rülke, A., Ihde, J., Lindner, K., Miller, H., Niemeier, W., Schenke, H.W., Seeber, G., 2004. Plate kinematics and deformation status of the Antarctic Peninsula based on GPS. Global. Planet. Change, 42, 313–321.

Domenico, S.N., 1977. Elastic properties of unconsolidated porous sand reservoirs. Geophysics, 42, 1339–1368.

Dvorkin, J., Prasad, M., Sakai, A., Lavoie, D., 1999. Elasticity of marine sediments: Rock physics modeling. Geophys. Res. Lett. 26(12), 1781–1784.

Dvorkin, J., Mavko, G., Nur, A., 1991. The effect of cementation on the elastic properties of granular material. Mech. Mater. 12, 207–217.

Dvorkin, J., Hoeksema, N.R., Nur, A., 1994. The squirt-flow mechanism: Macroscopic description. Geophysics, 59(3), 428–438.

Dvorkin, J., Nur, A., 1996. Elasticity of high-porosity sandstones: theory for two North Sea data sets. Geophysics, 61, 1363–1378.

Ecker, C., 2001. Seismic characterization of methane hydrate structures. Ph.D. Thesis, Stanford University, California.

Ecker, C., Dvorkin, J., Nur, A., 2000. Estimating the amount of gas hydrate and free gas from marine seismic data. Geophysics, 65(2), 565–573.

Ecker, C., Dvorkin, J., Nur, A., 1998. Sediments with gas hydrates: internal structure from seismic AVO. Geophysics, 63, 1659–1669.

Exley, R.J.K., Westbrook, G.K., Haacke, R.R., Peacock, S., 2010. Detection of Seismic anisotropy using ocean bottom seismometers: a case study from northern headwall of Storegga Slide. Geophys. J. Int. 183, 188–210.

Gaiser, J.E., 1999. Applications for vector coordinate systems of 3-D converted wave data. Lead. Edge. 18, 1290–1300.

Gassmann, F., 1951. Über die elastizität poröser medien. Vierteljahr. Naturforsch. Gesell. Zurich. 96, 1–23.

Gei, D., Carcione, J.M., 2003. Acoustic properties of sediments saturated with gas hydrate, free gas and water. Geophys. Prospect. 51, 141–157.

Geletti, R., Busetti, M., 2011. A double bottom simulating reflector in the western Ross Sea, Antarctica. J. Geophys. Res. 116, B04101.

Grad, M., Guterch, A., Janik, T., 1993. Seismic structure of the lithosphere across the zone of subducted Drake plate under the Antarctic plate, West Antarctica. Geophys. J. Int. 115, 586–600.

Giustiniani, M., Accettella, D., Tinivella, U., Loreto, M.F., Accaino, F., 2008. Geographic information system: an application to gas hydrate reservoir. Adv. Geosci. 18, 213–222.

Hamilton, E.L., 1976. Variations of density and porosity with depth in deep-sea sediments. J. Sediment. Petrol. 46, 280–300.

Hamilton, E.L., 1979. Vp/Vs and Poisson's ratios in marine sediments and rocks. J. Acou. Soc. Am. 66, 1093–1101.

Heimann, M., 2010. How stable is the methane cycle. Science, 327, 1211–1212.

Hein, J.R., Scholl, D.W., Barron, J.A., Jones, M.G., Miller, J.J., 1978. Diagenesis of Late Cenozoic diatomaceous deposits and formation of the bottom simulating reflector in the southern Bering Sea. Sedimentology, 25, 155–181.

Helgerud, M., Dvorkin, J., Nur, A., Sakai, A., Collett, T., 1999. Elastic-wave velocity in marine sediments with gas hydrates: Effective medium modeling. Geophys. Res. Lett. 26(13), 2021–2024.

Holbrook, W.S., Hoskins, H., Wood, W.T., Stephen, R.A., Lizarralde, D., 164. Science Party, 1996. Methane hydrate and free gas on the Blake ridge from vertical seismic profiling. Science, 273, 1840–1843.

Holland, M., Schultheiss, P., Roberts, J., Druce, M., 2008. Observed gas hydrate morphologies in marine sediments. Proceedings of the 6th International Conference on Gas Hydrates, Chevron, Vancouver, B. C., Canada, 6–10 July.

Hornbach, M.J., Holbrook, W.S., Gorman, A.R., Hackwith, K.L., Lizarralde, D., Pecher, I., 2003. Direct seismic detection of methane hydrate on the Blake Ridge. Geophysics, 68 (1), 92–100.

Hyndman, R.D., Spence, G.D., 1992. A seismic study of methane hydrate marine bottom simulating reflectors. J. Geophys. Res. 97, 6683–6698.

Hyndman, R., Spence, G., Chapman, N., Riedel, M., Edwards, N., 2001. Geophysical studies of marine gas hydrate in Northern Cascadia. Geophys. Monogr. Ser. 124, 273–295.

Isaacs, C.M., 1982. Influence of rock composition on kinetics of silica phase changes in the Monterey Formation, Santa Barbara area, California. Geology, 10 (6), 304–308.

Jakobsen, M., Hudson, J.A., Minshull, T.A., Singh, S.C., 2000. Elastic properties of hydrate-bearing sediments using effective-medium theory. J. geophys. Res. 105, 561–577.

Jin, Y.K., Larter, R.D., Kim, Y., Nam, S.H., Kim, K.J., 2002. Post-subduction margin structures along Boyd Strait, Antarctic Peninsula. Tectonophysics, 346, 187–200.

Johnson, A., 2011. Global resource potential of gas hydrate—A new calculation. Fire Ice, Dep. Energy, Nat. Energy Technol. Lab. Newsl. 11, 1–4.

Kastner, M., Keene, J.B., Gieskes, J.M., 1977. Diagenesis of siliceous oozes–I. Chemical controls on the rate of opal-A to opal-CT transformation an experimental study. Geochim. Cosmochim. Ac. 41, 1041–1059.

Katzman, R., Holbrook, W.S., Paull, C.K., 1994. Combined vertical-incidence and wide-angle seismic study of a gas hydrate zone, Blake ridge. J. Geophys. Res. 99, 17975–17995.

Keller, M.A., Isaacs, C.M., 1985. An evaluation of temperature scales for silica diagenesis in diatomaceous sequences including a new approach based on the Miocene Monterey Formation, California. Geo-Mar. Lett. 5, 31– 35.

Kennett, J.P., Cannariato, K.G., Hendy, L.L., Behl, R. J., 2002. Methane Hydrates in Quaternary Climate Change: The Clathrate Gun Hypothesis. Spec. Publ., 54, AGU, Washington, D. C.

Kennett, J. P., Cannariato, K.G., Hendy, I. L., Behl, R.J., 2007. Carbon isotopic evidence for methane hydrate stability during Quaternary Interstadials. Science, 288, 128–133.

Kim, Y., Kim, H.S., Larter, R.D., Camerlenghi, A., Gamb ôa, L.A.P., Rudowski, S., 1995. Tectonic deformation in the upper crust and sediments at the South Shetland Trench. In: Cooper, A.K., Barker, P.T., Brancolini, G. (Eds.), Geology and Seismic Stratigraphy of the Atlantic Margin. American Geophysical Union: Washington, DC, USA, 68, pp. 157–166.

Kirchner, M.T., Boese, R., Billups, W.E., Norman, L.R., 2004. Gas hydrate single-crystal structure analyses. J. Am. Chem. Soc., 126 (30), 9407–9412.

Korenaga, J., Holbrook, W.S., Singh, S.C., Minshull, T.A., 1997. Natural gas hydrates on the southeast US margin: Constraints from full waveform and travel time inversions of wide-angle seismic data. J. Geophys. Res. 102, 15345–15365.

Kumar, D., Sen, M.K., Bangs, N.L., 2007. Gas hydrate concentration and characteristics within Hydrate Ridge inferred from multicomponent seismic reflection data. J. Geophys. Res. 112, B12306.

Kumar, D., 2005. Analysis of multicomponent seismic data from the Hydrate Ridge, Offshore Oregon. Ph.D. Thesis, The University of Texas at Austin.

Kuramoto, S., Tamaki, K., Langseth, M.G., Nobes, D.C., Tokuyama, H., Pisciotto, K.A., Taira, A., 1992. Can opalA/opalCT BSR be an indicator of the thermal structure of the Yamamoto basin. Japan Sea? Proc. Ocean Drill. Program Sci. Results, 127–128.

Kuster, G. T., Toksöz, M.N., 1974. Velocity and attenuation of seismic waves in two-phase media: Part I. Theoretical formulations. Geophysics, 39, 587–606.

Kvenvolden, K.A., 1988. Methane hydrate —a major reservoir of carbon in the shallow geosphere? Chem. Geol. 71, 41–51.

Kvenvolden, K.A., 1998. A primer on the geological occurrence of gas hydrate. Geol. Soc. Spec. Publ. 137, 9–30.

Kvenvolden, K.A., 1993. Gas hydrates-geological perspective and global change. Rev. Geophys. 31, 173–187.

Kvenvolden, K.A., 1999. Potential effects of gas hydrate on human welfare. Proc. Natl. Acad. Sci. U. S. A. 96, 3420–3426.

Kvenvolden, K.A., 2000. Gas hydrate and humans. Ann. Ny. Acad. Sci. 912, 17–22.

Larter, R.D., Barker, P.F., 1991. Effects of ridge crest-trench interaction on Antarctic-Phoenix spreading: Forces on a young subducting plate. J. Geophys. Res. 96, 19583–19607.

Leclaire, P., 1992. Propagation acoustique dans les milieux poreux soumis au gel-Modélisation et expérience. Ph.D. Thesis. Université Paris, Paris, France, 7.

Leclaire, P., Cohen-Tenoudji, F., Aguirre-Puente, J., 1994. Extension of Biot's theory of wave propagation to frozen porous media. J. Acoust. Soc. Am. 96(6), 3753–3768.

Leclaire, P., Cohen-Tenoudji, F., Aguirre-Puente, J., 1995. Observation of two longitudinal and two transverse waves in a frozen porous medium. J. Acoust. Soc. Am. 97(4), 2052–2055.

Lee, M.W., Hutchinson, D.R., Collett, T.S., Dillon, W.P., 1996. Seismic velocities for hydrate-bearing sediments using weighted equation. J. geophys. Res. 101, 20347–20358.

Lee, M.W., Waite, W.F., 2008. Estimating pore-space gas hydrate saturations from well log acoustic data. Geochem. Geophys. Geosyst. 9, Q07008.

Lee, M.W., 2005. Proposed moduli of dry rock and their application to predicting elastic velocities of sandstones, report no. 2005–5119. U.S. Geol. Surv. Sci. Invest.

Lee, M.W., 2002. Biot–Gassmann theory for velocities of gas hydrate-bearing sediments. Geophysics, 67, 1711–1719.

Lee, M.W., Collett, T.S., 2006. Gas hydrate and free gas saturations estimated from velocity logs on hydrate ridge, offshore Oregon, USA. In A.M. Trehu, G. Bohrmann, M.E. Torres, and F.S. Colwell, eds., Proc. ODP, Sci. Results, 204: College Station, TX (Ocean Drilling Program), 1–25.

Lodolo, E., Camerlenghi, A., Brancolini, G., 1993. A bottom simulating reflector on the South Shetland margin, Antarctic Peninsula. Antarct. Sci. 5, 207–210.

Lodolo, E., Camerlenghi, A., Madrussani, G., Tinivella, U., Rossi, G., 2002. Assessment of gas hydrate and free gas distribution on the South Shetland margin (Antarctica) based on multichannel seismic reflection data. Geophys. J. Int. 148, 103–119.

Lonsdale, M.J., 1990. The relationship between silica diagenesis, methane, and seismic reflections on the South Orkney microcontinent. Proc. Ocean Drill. Program Sci. Results, 113, 27–36.

Loreto, M.F., Della Vedova, B., Accaino, F., Tinivella, U., Accettella, D., 2006. Shallow geological structures of the South Shetland trench, Antarctic Peninsula. Ofioliti, 31(2), 151–159.

Loreto, M.F., Tinivella, U., Accaino, F., Giustiniani, M., 2011. Gas hydrate reservoir characterization by geophysical data analysis (offshore Antarctic Peninsula). Energies, 4, 39–56.

Loreto, M.F., Tinivella, U., 2012. Gas hydrate versus geological features: The South Shetland case study. Mar. Pet. Geol. 36, 164–171.

Lynne, B.Y., Campbell, K.A., 2004. Morphologic and mineralogic transitions from opal-A to opal-CT in low-temperature siliceous sinter diagenesis, Taupo Volcanic Zone, New Zealand. J. Sediment. Res. 74(4), 561.

MacDonald, J.G., 1990. Role of methane clathrates in past and future climates. Clim. Change, 16, 247–281.

Maldonado, A., Larter, R.D., Aldaya, F., 1994. Forearc tectonic evolution of the South Shetland Margin, Antarctic Peninsula. Tectonics, 13, 1345–1370.

Malone, R., 1985. Gas hydrates topical report. Tech. Rep. DOE/METC/SP-218 (DE85001986). Department of Energy, Morgantown Energy Technology Center, USA.

Marín-Moreno, H., Giustiniani, M., Tinivella, U., 2015. The potential response of the hydrate reservoir in the South Shetland Margin, Antarctic Peninsula, to ocean warming over the 21st century. Polar. Res. 34, 27443.

Marsset, B., Menut, E., Ker, S., Thomas, Y., Regnault, J.P., Leon, P., Martinossi, H., Artzner, L., Chenot, D., Dentrecolas, S., Spychalski, B., Mellier, G., Sultan, N., 2014. Deep-towed High Resolution multichannel seismic imaging. Deep Sea Research Part I: Oceanographic Research Papers, 93, 83–90.

Martos-Villa, R., Guggenheim, S., Pilar Mata, M., Ignacio Sainz-Díaz, C., Nieto, F., 2014. Interaction of methane hydrate complexes with smectites: Experimental results compared to molecular models. Am. Mineral. 99(2–3), 401–414.

Mestdagh, T., Jeffrey P., Marc, D.B., 2017. The sensitivity of gas hydrate reservoirs to climate change : perspectives from a new combined model for permafrost-related and marine settings. Earth-Sci. Rev. 169, 104–131.

Mienert, J., Vanneste, M., Bünz, S., Andreassen, K., Haflidason, H., Sejrup, H.P., 2005. Ocean warming and gas hydrate stability on the mid-Norwegian margin at the Storegga Slide. Mar. Pet. Geol. 22, 233–244.

Milkov, A.V., 2004. Global estimates of hydrate-bound gas in marine sediments: how much is really out there? Earth Sci. Rev. 66, 183–197.

Mindlin, R.D., 1949. Compliance of elastic bodies in contact. J. Appl. Mech., 16, 259–268.

Neagu R.C., Tinivella U., Volpi V., Rebesco M., Camerlenghi A., 2009. Estimation of biogenic silica contents in marine sediments using seismic and well log data: Sediment Drift 7, Antarctica. Int. J. Earth. Sci. 98, 839–848.

Nisbet, E.G., 2002. Have sudden large releases of methane from geological reservoirs occurred since the Last Glacial Maximum, and could such releases occur again? Philosophical Transactions of the Royal Society of London Series A-Mathematical Physical and Engineering Sciences, 360 (1793), 581–607.

Nishizawa, O., 1982. Seismic velocity anisotropy in a medium containing oriented cracks: transversely isotropic case. J. Phys. Earth, 30, 331–347.

Nouzé, H., Cosquer, E., Collot, J., Foucher, J.P., Frauke, F., Lafoy, Y., Louis, G., 2009. Geophysical characterization of bottom simulating reflectors in the Fairway Basin (off New Caledonia, Southwest Pacific), based on high resolution seismic profiles and heat flow data. Mar. Geol. 266(1–4), 80–90.

Ojha, M., Sain, k., Minshull, T.A., 2010. Assessment of gas-hydrate saturations in the Makran accretionary prism using the offset dependence of seismic amplitudes. Geophysics, 75(2), C1–C6.

Paull, C.K., Matsumoto, R., Wallace, P.J., and et al., 1996. Proceedings ODP, Initial Reports, Leg164, Tech. rep., College Station, TX (Ocean Drilling Program).

Peacock, S., Westbrook, G.K., Bais, G., 2010. S-wave velocities and anisotropy in sediments entering the Nankai subduction zone, offshore Japan. Geophys. J. Int. 180, 743–758.

Pearson, C.F., Halleck, P.M., McGulre, P.L., Hermes, R., Mathews, M., 1983. Natural gas hydrates deposits: a review of in situ properties. J. Phys. Chem. 87, 4180–4185.

Pecher, I.A., Kukowski, N., Ranero, C.R., Huene, R.V., 2001. Gas hydrates along the Peru and Middle America trench systems. In: Paull, C.K., Dillon, W.P. (Eds.), Natural gas hydrates:

occurrence, distribution and detection. Washington, D.C.: American Geophysical Union, pp. 257–271.

Petersen, C.J., Papenberg, C., Klaeschen, D., 2007. Local seismic quantification of gas hydrates and BSR characterization from multi-frequency OBS data at northern Hydrate Ridge. Earth planet. Sci. Lett. 255, 414–431.

Petersen, C.J., Bünz, S., Hustoft, S., Mienert, J., Klaeschen, D., 2010. High-resolution P-Cable 3D seismic imaging of gas chimney structures in gas hydrated sediments of an Arctic sediment drift. Mar. Petrol. Geol. 27(9), 1981–1994.

Piñero, E., Marquardt, M., Hensen, C., Haeckel, M., Wallmann, K., 2013. Estimation of the global inventory of methane hydrates in marine sediments using transfer functions. Biogeosciences, 10, 959–975.

Reagan, M.T., Moridis, G.J., 2007. Oceanic gas hydrate instability and dissociation under climate change scenarios. Geophys. Res. Lett. 34, L22709.

Rebesco, M., Larter, R.D., Camerlenghi, A., Barker, P.F., 1996. Giant sediment drifts on the continental rise west of the Antarctic Peninsula. Geo-Mar. Lett. 16, 65–75.

Reuss, A., 1929. Berechnung der Fleissgrenze von Mischkristalen auf Grund der Plastizitätsbelingung für ein Kristalle, Z. Angew. Math. Mech. 9, 49–58.

Rossi, G., Gei, D., Böhm, G., Madrussani, G., Carcione, J. M., 2007. Attenuation tomography: An application to gas-hydrate and free-gas detection. Geophys. Prospect. 55, 655–669.

Ruppel, C., 2011. Methane hydrates and the future of natural gas. Supplementary Paper #4, The Future of Natural Gas, MIT Energy Initiative study, pp. 25.

Ruppel, C.D., 2011. Methane hydrates and contemporary climate change. Nature Education Knowledge, 3(10), 29.

Ruppel, C.D., Kessler, J.D., 2017. The interaction of climate change and methane hydrates. Rev. Geophys. 55, 126–168.

Satyavani, N., Sain, K., Gupta, H.K., 2016. Ocean bottom seismometer data modeling to infer gas hydrate saturation in Krishna-Godavari (KG) basin. J. Nat. Gas. Sci. Eng. 33, 908–917.

Severinghaus, J.P., Sowers, T., Brook, E.J., Alley, R.B., Bender, M.L., 1998. Timing of abrupt climate change at the end of the Younger Dryas interval from thermally fractionated gases in polarice. Nature, 391, 141.

Sheng, P., 1990. Effective-medium theory of sedimentary rocks. Phys. Rev. B. 41, 4507–4512.

Shipley, T.H., Houston, M., Buffler, R.T., Shaub, F.J., McMillan, K.J., Ladd, J.W., Worzel, J.L., 1979. Seismic reflection evidence for the wide-spread occurrence of possible gas-hydrate horizons on continental slopes and rises. Am. Assoc. Pet. Geol. Bull. 63, 2204–2213.

Singh, S.C., Minshull, T.A., Spence, G.D., 1993. Velocity structure of a gas hydrate reflector. Science, 260, 104–207.

Singhroha, S., Bünz, S., Plaza-Faverola, A., Chand, S., 2016. Gas hydrate and free gas detection using seismic quality factor estimates from high-resolution P-cable 3D seismic data. Interpretation, 4(1), 39–54.

Sloan, E.D., 1998. Clathrate hydrates of natural gases, 2nd ed.; Marcel Dekker, Inc.: New York, NY, USA, 1–641, ISBN:0824799372.

Sloan, E.D., Koh, C.A., 2008. Clathrate hydrates of natural gases: Boca Raton, CRC, 703 p.

Somoza, L., León R., Medialdea T., Pérez L.F., González F.J., Maldonado A., 2014. Seafloor mounds, craters and depressions linked to seismic chimneys breaching fossilized diagenetic bottom simulating reflectors in the central and southern Scotia Sea, Antarctica. Global. Planet. Change, 123, 359–373.

Song, S., Tinivella, U., Giustiniani, M., Singhroha, S., Bünz, S., Cassiani, G., 2018. OBS data analysis to quantify gas hydrate and free gas in the South Shetland margin (Antarctica). Energies, 11, 3290.

Sposito, G., 1984. The Surface Chemistry of Soils. Oxford Univ. Press, New York.

Stewart, R.R., Gaiser, J.E., Brown, R.J., Lawton, D.C., 2002. Converted-wave seismic exploration: Methods. Geophysics, 67, 1348–1363.

Sutton, R., Sposito, G., 2001. Molecular Simulation of Interlayer Structure and Dynamics in 12.4 Å Cs-Smectite Hydrates. J. Colloid. Interf. Sci. 237, 174–184.

Thein, J., von Rad, U., 1987. Silica diagenesis in continental rise and slope sediments off eastern North America (Sites 603 and 605, Leg 93; Sites 612 and 613, Leg 95). Initial Reports of the Deep Sea Drilling Project, 95, Washington (U.S. Govt. Printing Office).

Thomas, C., Livermore, R., Pollitz, F., 2003. Motion of the Scotia Sea Plates. Geophys. J. Int. 155, 789–804.

Timur, A., 1968. Velocity of compressional waves in porous media at permafrost temperatures. Geophysics, 33, 584–595.

Tinivella, U., Loreto, M.F., Accaino, F., 2009. Regional versus detailed velocity analysis to quantify hydrate and free gas in marine sediments: The south Shetland margin target study. Geol. Soc. Spec. Publ. 319, 103–119.

Tinivella, U., Accaino, F., Camerlenghi, A., 2002. Gas hydrate and free gas distribution form inversion of seismic data on the South Shetland margin (Antarctica). Mar. Geophys. Res. 23, 109–123.

Tinivella, U., Accaino, F., Della Vedova, B., 2008. Gas hydrates and active mud volcanism on the South Shetland continental margin, Antarctic Peninsula. Geo-Mar. Lett. 28, 97–106.

Tinivella, U., Lodolo, E., Camerlenghi, A., Boehm, G., 1998. Seismic tomography study of a bottom simulating reflector off the South Shetland Margin (Antarctica). In: Henriet, J.-P., Mienert, J. (Eds.), Gas Hydrates: Relevance to World Margin Stability and Climate Change. Geol. Soc. Spec. Publ. 137, pp. 141–151.

Tinivella, U., Accaino, F., 2000. Compressional velocity structure and Poisson's ratio in marine sediments with gas hydrate and free gas by inversion of reflected and refracted seismic data (South Shetland Islands, Antarctica). Mar. Geol. 164, 13–27.

Tinivella, U., 1999. A method for estimating gas hydrate and free gas concentrations in marine sediments. Boll. Geofis. Teor. Appl. 40, 19–30.

Tinivella, U., 2002. The seismic response to overpressure versus gas hydrate and free gas concentration. J. Seism. Explor. 11, 283–305.

Tinivella, U., Carcione, J.M., 2001. Estimation of gas-hydrate concentration and free-gas saturation from log and seismic data. Lead. Edge. 20, 200–203.

Tinivella, U., Lodolo, E., 2000. The Blake Ridge BSR transect: Tomographic velocity field and theoretical model to estimate methane hydrate quantities. In: Paull, C.K., Matsumoto, R., Wallace, P.J., Dillon, W.P. (Eds.). Proc. Ocean Drill. Program Sci. Results, 164.

Tinivella, U., Giustiniani, M., 2012. An overview of mud volcanoes associated to gas hydrate system. Chap 6, in Updates in Volcanology—New Advances in Understanding Volcanic Systems, edited by K. Nemeth, pp. 225–267, InTech, Rijeka, Croatia.

Tribble, J.S., Mackenzie, F.T., Urmos, J., O'Brien, D.K., Manghnani, M.H., 1992. Effects of biogenic silica on acoustic and physical properties of clay-rich marine sediments. AAPG Bull. 76, 792–804.

Van der Hilst, R.D., Widiyantoro, S., Engdahl, E.R., 1997. Evidence for deep mantle circulation from global tomography. Nature, 386, 578–584.

Voigt, W., 1928. Lehrbuch der Kristallphysik. B.G. Terbner, Leipzing.

Volpi, V., Camerlenghi, A., Hillenbrand, C.D., Rebesco, M., Ivaldi, R., 2003. Effects of biogenic silica on sediment compaction and slope stability on the Pacific margin of the Antarctic Peninsula. Basin Res. 15, 339–363.

Waite, W.F., Winters, W.J., Mason, D.H., 2004. Methane hydrate formation in partially saturated Ottawa sand. Am. Mineral. 89, 1221–1227.

Waite, W., Helgerud, M.B., Nur, A., Pinksto, J.C., Stern, L., Kirby, S., 2000. Laboratory measurements of compressional and shear wave speeds through methane hydrate. In: Holder, G.D., Bishnoi, P.R. (Eds.), Gas Hydrates: Challenges for the Future. Annual. N. Y. Acad. Sci. 912, pp. 1003–1010.

Warner, M., 1990. Absolute reflection coefficients from deep seismic reflections. Tectonophysics, 173, 15–23.

Westbrook, G.K., Chand, S., Rossi, G., Long, S., Bünz, S., Camerlenghi, A., Carcione, J.M., Dean, S., Foucher, J.P., Flueh, E., Haacke, R.R., Madrussani, G., Mienert, J., Minshull, T.M., Nouzé, H., Peacock, S., Reston, T.J., Vanneste, M., Zillmer, M., 2008. Estimation of gas-hydrate concentration from multi-component seismic data at sites on the continental margins of NW Svalbard and the Storegga region of Norway. Mar. Pet. Geol. 25, 744–758.

Willis, J.R., 1977. Bounds and self-consistent estimates for the overall properties of anisotropic composites. J. Mech. Phys. Solids. 25, 185–202.

Wood, A.B., 1941. A Textbook of Sound. Macmillan, New York.

Wyllie, M.R., Gregory, A.R., Gardener, G.H.P., 1958. An experimental investigation of factors affecting elastic wave velocities in porous media. Geophysics, 23, 459–493.

Yun, T.S., 2005. Mechanical and thermal study of hydrate bearing sediments. Ph.D. thesis, Georgia Institute of Technology.

Zelt, C.A., Smith, R.B., 1992. Seismic travel time inversion for 2-D crustal velocity structure. Geophys. J. Int. 108, 16–34.

Zelt, B.C., Ellis, R.M., Clowes, R.M., Hole, J.A., 1996. Inversion of three-dimensional wide-angle seismic data from the Southwestern Canadian Cordillera. J. Geophys Res. 101, 8503–8529.

Zelt, C.A., 1999. Modelling strategies and model assessment for wide-angle seismic traveltime data. Geophys. J. Int. 139, 183–204.

Zimmerman, R.W., King, M.S., 1986. The effect of the extent of freezing on seismic velocities in unconsolidated permafrost. Geophysics, 39, 587–606.

Appendix 1

energies

MDPI

Article

OBS Data Analysis to Quantify Gas Hydrate and Free Gas in the South Shetland Margin (Antarctica)

Sha Song [1,*], Umberta Tinivella [2], Michela Giustiniani [2], Sunny Singhroha [3], Stefan Bünz [3] and Giorgio Cassiani [1]

1 Department of Geosciences, University of Padova, Via Gradenigo 6, 35131 Padova, Italy; giorgio.cassiani@unipd.it
2 Istituto Nazionale di Oceanografia e di Geofisica Sperimentale—OGS, 34010 Sgonico, Italy; utinivella@inogs.it (U.T.); mgiustiniani@inogs.it (M.G.)
3 CAGE—Centre for Arctic Gas Hydrate, Environment and Climate, Department of Geosciences, UiT The Arctic University of Norway, Dramsveien 201, 9010 Tromsø, Norway; sunny.singhroha@uit.no (S.S.); stefan.buenz@uit.no (S.B.)
* Correspondence: sha.song@studenti.unipd.it; Tel.: +39-377-845-7699

Received: 6 October 2018; Accepted: 21 November 2018; Published: 25 November 2018

Abstract: The presence of a gas hydrate reservoir and free gas layer along the South Shetland margin (offshore Antarctic Peninsula) has been well documented in recent years. In order to better characterize gas hydrate reservoirs, with a particular focus on the quantification of gas hydrate and free gas and the petrophysical properties of the subsurface, we performed travel time inversion of ocean-bottom seismometer data in order to obtain detailed P- and S-wave velocity estimates of the sediments. The P-wave velocity field is determined by the inversion of P-wave refractions and reflections, while the S-wave velocity field is obtained from converted-wave reflections received on the horizontal components of ocean-bottom seismometer data. The resulting velocity fields are used to estimate gas hydrate and free gas concentrations using a modified Biot-Geertsma-Smit theory. The results show that hydrate concentration ranges from 10% to 15% of total volume and free gas concentration is approximately 0.3% to 0.8% of total volume. The comparison of Poisson's ratio with previous studies in this area indicates that the gas hydrate reservoir shows no significant regional variations.

Keywords: gas hydrate; free gas; ocean-bottom seismometer; PS-converted wave; travel time tomography; South Shetland margin

1. Introduction

Gas hydrates are ice-like crystalline solids composed of water and low-molecular-weight gases (mostly methane), which form under conditions of high pressure, low temperature, and sufficient gas concentration [1]. Hydrates are widespread in the shallow marine sediments along continental margins and in permafrost areas [2]. Gas hydrates in the marine sediments have commonly been inferred on the basis of seismic reflection profiles from the presence of a so-called bottom simulating reflection (BSR) that marks the base of the gas hydrate stability zone [3]. A BSR is generated due to the strong impedance contrast between hydrate-bearing sediments above and underlying free gas-bearing sediments. During the last few decades, much effort has been expended on the study of gas hydrates because of their economic potential as a future energy source [4,5] and their potential role in geohazards [6–8] and global climate change [9–15].

In the majority of situations, where no direct measurements are available, the analysis of seismic velocity provides an efficient way to identify and characterize the distribution of gas hydrates and

free gas in marine sediments [7,16–20]. Gas hydrate-bearing sediments show higher P-wave velocity (V_P) compared to water-saturated sediments whereas the presence of free gas reduces the P-wave velocity with respect to water-saturated sediments [17]. The effect of gas hydrates on S-wave velocity (V_S) is different because it depends on the micro-scale distribution of hydrates within the sediments, i.e., as pore fluid components or cementing grain contacts (e.g., References [20–23]). Therefore, the measurement of S-wave velocity is crucial, and it can help to understand the distribution of gas hydrates within the pore space and provide additional constraints in estimating hydrate concentration [3,12,23]. The analysis of shear waves can be achieved by deploying multi-component ocean-bottom seismometer (OBS) on the seafloor which allows recording of converted PS-wave reflections, in addition to wide-angle P-wave reflections and refractions.

OBS data have been used successfully in the characterization of gas hydrate reservoirs by combined analysis of P- and S-waves, and the importance of S-wave velocity has been pointed out [23–25]. In the South Shetland margin (offshore Antarctic Peninsula), very few studies have been performed to estimate hydrate concentration utilizing OBS data. For example, in the last 20 years, only one OBS deployed during the 1996/97 cruise was analyzed by Reference [3]: the P-wave velocity structure and Poisson's ratio in the marine sediments were estimated by travel time inversion of reflections and refractions and then were used to quantify the amounts of gas hydrate and free gas. The Poisson's ratio obtained from the analysis of this OBS has been used by several authors to evaluate the shear modulus of sediment in the same area [26–28].

The occurrence of a potential gas hydrate reservoir has been demonstrated from the analysis of seismic data acquired during three Italian Antarctic cruises in 1989/1990, 1996/1997, and 2003/2004, onboard the R/V OGS Explora (e.g., References [3,29–31]). The South Shetland margin is located in the northeastern tip of the Pacific margin of the Antarctic Peninsula, which is characterized by the subduction of the Antarctic and the former Phoenix plates beneath the South Shetland micro-continental block. Along the continental margin, a trench-accretionary prism-fore-arc basin sequence can be recognized [32,33]. The Phoenix plate started to subduct beneath the Antarctic plate from late Paleozoic time [34] and progressed from the southwest to the northeast along the margin. Active spreading at the Antarctic Phoenix ridge ceased at about 4 Ma ago [35], when the last ridge-crest segment of the Phoenix plate reached the south margin of the Hero Fracture Zone (HFZ). The subduction process is presently believed to take place as a result of sinking and roll-back of the oceanic plate coupled with the extension of the Bransfield Strait marginal basin [33,35–37]. The Phoenix plate is bordered by the Shackleton Fracture Zone to the northeastern side, while by the HFZ to the southwestern side, which intersect the continental lithosphere.

Long-term ocean warming could induce the dissociation of gas hydrates in this area and the release of methane may contribute to climate change (i.e., Reference [38]). Therefore, it is very important to enhance existing knowledge on the gas hydrate reservoir located in the South Shetland margin. In order to investigate the possible change of petrophysical properties in the gas hydrate reservoir, here we present the analysis of data from two OBSs deployed during the 2003/2004 cruise, as shown in Figure 1.

The objectives of this study are: (a) to obtain a more reliable estimate of distribution and concentration of gas hydrate and free gas within the sediments and (b) investigate the change of petrophysical properties in the gas hydrate reservoir. The P- and S-wave velocity fields are determined by travel time inversion and ray-tracing forward modeling using multi-component OBS data. A theoretical model is then applied to estimate gas hydrate and free gas concentration using P- and S-wave velocities.

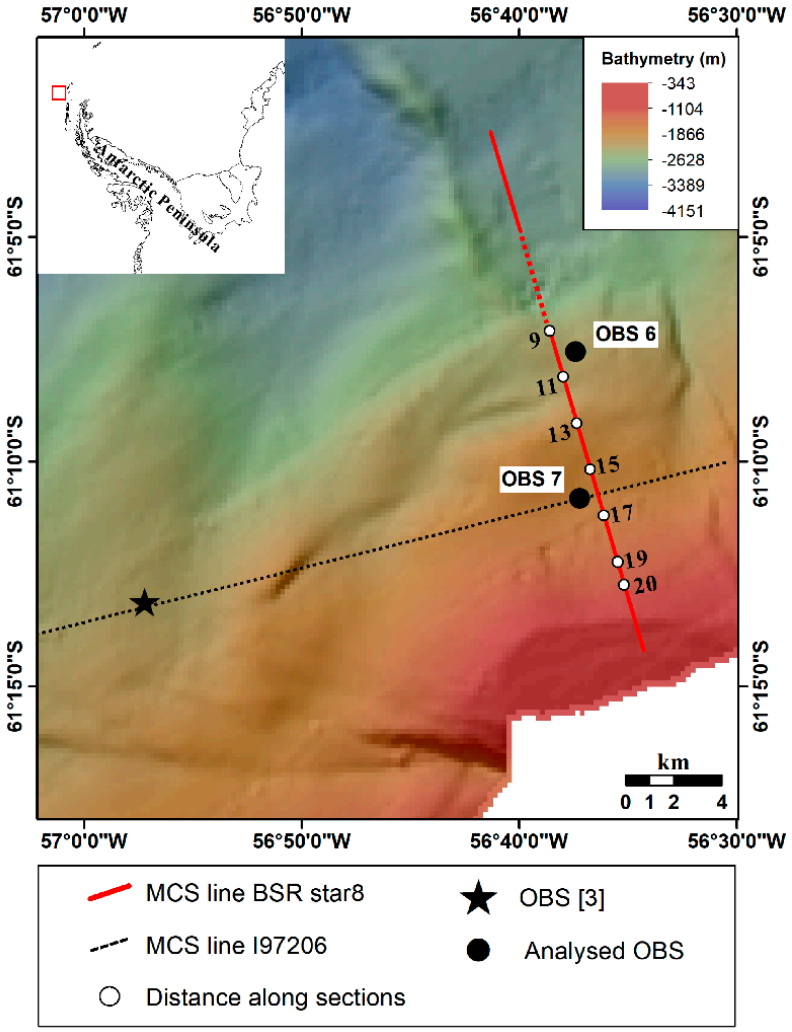

Figure 1. Bathymetric map of the study area (modified after References [27,28]), indicating the locations of seismic lines and ocean bottom seismometers (OBSs). The black circles indicate the positions of OBSs. The red line indicates the multi-channel seismic (MCS) line shown in Figure 2; the red dotted line indicates the gap for the MCS line; the white circles and numbers show the corresponding distances along sections. The star and dashed line mark the OBS and seismic line analyzed in the study by Reference [3].

2. Data and Methods

2.1. Seismic Data Acquisition and Processing

The seismic data analyzed in this study were acquired during the austral summer of 2003–2004 onboard the R/V OGS Explora, in the frame of a project supported by the Italian National Antarctic Program (PNRA). Two four-component (one hydrophone and three orthogonally orientated geophones) OBSs were deployed along the multi-channel seismic (MCS) line BSRstar8 where the BSR appears to be particularly strong, as shown in Figures 1 and 2. The seismic source was two generator-injector (GI) air guns with a total volume of 3.5 L firing every 50 m, while for MCS acquisition, a 600-m-long streamer with 48 channels was used. The sampling interval of OBS data was 2 ms.

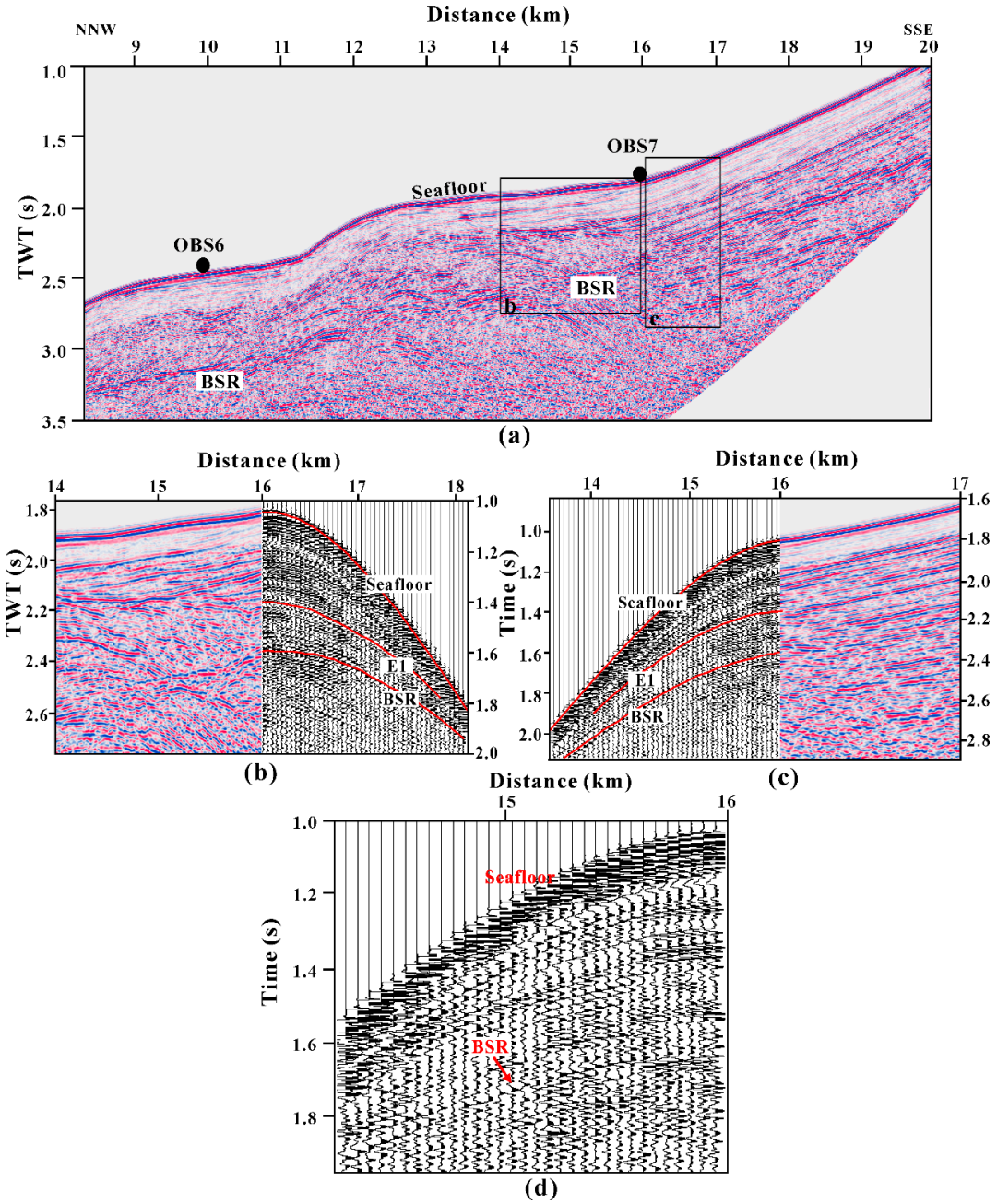

Figure 2. (**a**) Time migrated section of part of MCS line BSRstar8. An automatic gain control (AGC) with a time window of 400 ms was applied to better image the bottom simulating reflection (BSR). The solid circles indicate the OBS locations projected on the MCS line. The boxes indicate the portion of the seismic line shown in panels (**b**) and (**c**); panels (**b**) and (**c**) report the correlation between the hydrophone component of OBS 7 and the MCS seismic section. Note that the two datasets have a different time axis due to the spatial drift of the OBS from the MCS line during the sinking. The travel time picks of P-wave reflections (Seafloor, E1, BSR) on the hydrophone data are shown as red lines on the OBS panels. See text for details; panel (**d**) close-up view of OBS panel (**c**) showing the BSR. TWT: two-way time.

Data processing was performed using the Seismic Unix software package [39]. The main processing steps applied to the MCS line BSRstar8 included trace editing, spherical divergence amplitude correction, band-pass filtering, spiking deconvolution, normal moveout correction, stack, time–variant filtering, and Kirchhoff post-stack time migration. The migration section shows a

remarkable high-amplitude reflector at a two-way time (TWT) of about 550–650 ms below the seafloor as shown in Figure 2a, characterized by reverse polarity with respect to the seafloor reflection, and nearly parallel to the seafloor, interpreted as BSR.

The exact locations of OBSs on the seafloor were determined using the arrival times of direct waves from the shots through the ocean water column, assuming a constant water velocity of 1450 m/s, while the seafloor depth was extracted from bathymetric data. The relocation result showed that both OBSs drifted about 750 m away, perpendicular from the shot line, in a water depth of 1790 m and 1320 m, respectively; this could be related to strong seawater currents [23]. In order to orient the horizontal components, the converted S-wave arrivals were used to estimate the angle by particle motion plots. Then this angle was adopted to rotate the two horizontal components into inline and crossline components [40]. After rotation, the inline component contained much more energy than the crossline component and this facilitated the identification of S-wave arrivals. The hydrophone component was chosen to identify P-wave reflections and refractions when compared with the vertical component. Actually, the ringing due to the effect of coupling between the instrument and the seafloor is prominent on the vertical component of OBS data, while it is absent from the hydrophone component. In order to improve the signal to noise ratio and enhance the phase identification, a spherical divergence amplitude correction and a 10–100 Hz band-pass filter were applied to the hydrophone component. The seismic processing of the inline component included: amplitude correction, predictive deconvolution (180 ms operator length and 50 ms lag), and band-pass filtering (14–100 Hz).

2.2. Travel Time Inversion

2.2.1. P-Wave Velocity Modeling

In order to obtain a reliable P-wave velocity model, we applied a 2D travel time inversion of reflected and refracted arrivals following the approach by Reference [41]. The MCS data provide a clear structural image but have limited source-receiver offsets (maximum offset is 710 m) and thus cannot provide accurate velocity information. On the other hand, the wide-angle OBS data provide relatively accurate velocity estimates but rather poor constraints on the structural image in comparison with that produced by MCS data. By combining the two datasets in the travel time inversion, the velocity model can be better constructed. The MCS data provided a basis for building the initial model. By correlating the reflection events of MCS data with those at near offset recorded by the hydrophone component of OBS data, the corresponding horizons were selected and picked, as shown in Figure 2b,c. Three reflections were picked: the seafloor, the BSR, one reflection (E1) between seafloor and BSR. Below the BSR, the picking was not performed because no clear reflectors were recognized on either OBS or MCS data due to the poor quality of the data. Note that the BSR is a strong reflector, and it thus masks structural features underneath. Refractions were observed in both OBSs; different phases can be identified and associated with the corresponding layers in the MCS by comparing their apparent velocities and depths. The modeling of refractions from OBS data allowed us to determine the base of the free gas layer (BGR) and obtain the velocity information of the layer below BGR (for a comparison, see Reference [3]). An example of picked refraction from OBS 7 is shown in Figure 3.

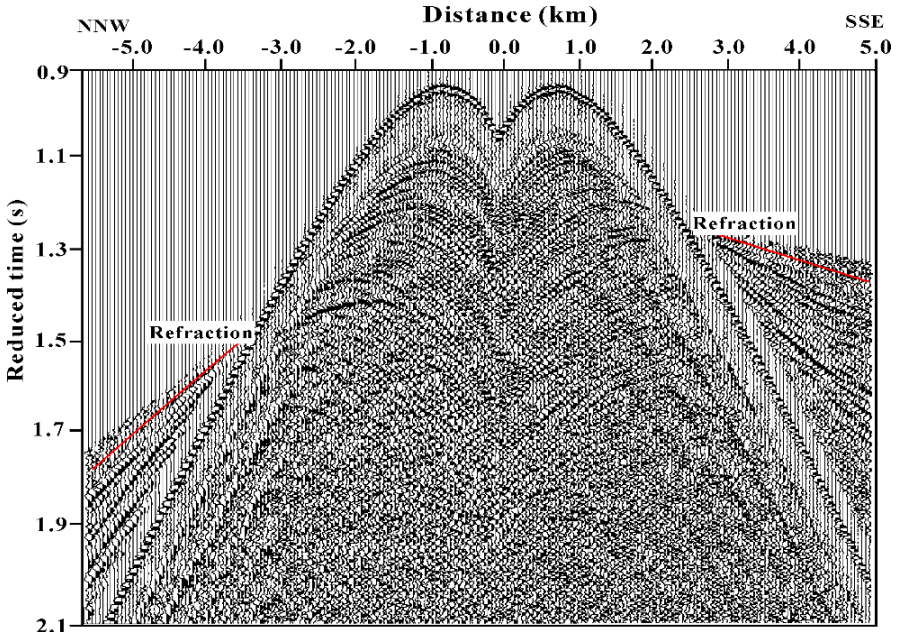

Figure 3. Hydrophone component of OBS 7 showing travel time picks (red lines) of refraction. The signal above the refraction is noise. The horizontal axis is the distance between projected OBS position and shot position. The time is reduced with a velocity of 3.2 km/s.

To satisfy the requirement of a 2D ray-tracing model, the OBS locations were projected onto the shooting line. A drift correction could not be applied to our data due to the large drift (about 750 m) of OBSs from the shooting line (e.g., Reference [42]). Thus, taking into account the relative error of offset caused by projection, the OBS reflections at near offset were excluded and MCS data were included during the inversion in order to constrain the geometrical model. Figure 4a shows an example of picked reflections from OBS 7 used for the inversion; note that the seafloor was picked at large offset (>3 km) and the picking is not shown. The arrival times of MCS data were picked on the common shot gathers; the picking was done at every shot at near offset (1 km on either side) of OBS locations, while every third shot with a spacing of 150 m at large offset.

The travel time inversion was accomplished with the same program (RayInvr [41]) as used by Reference [3]. The initial velocity-depth model was created based on the stack section of MCS line BSRstar8 and the velocity information obtained from previous studies (Reference [27] and the references therein). The model was parameterized into a layered, irregular network of trapezoids in which boundary nodes and upper and lower velocity points were connected by linear interpolation. Rays were traced through the model, and travel times were calculated and compared with the observed travel times. A damped least-squares inversion was used to update the model parameters by minimizing the misfit between the observed and the calculated travel times [41]. The forward ray-tracing and inversion steps were repeated until a satisfactory fit was achieved; that was, the root-mean-square (RMS) travel time residual was within the assigned picking errors and the normalized χ^2 was close to 1. This is equivalent to saying that the data fit within their estimated error bounds—assuming a Gaussian error distribution. This procedure was applied to all layers in a layer-stripping approach from the top to the bottom. Figure 4b,c show the ray diagram and travel time fit modeled on OBS 7. With the assigned pick uncertainty of 20 ms, an overall normalized χ^2 of 0.979 and an RMS travel time residual of 20 ms were achieved for this OBS.

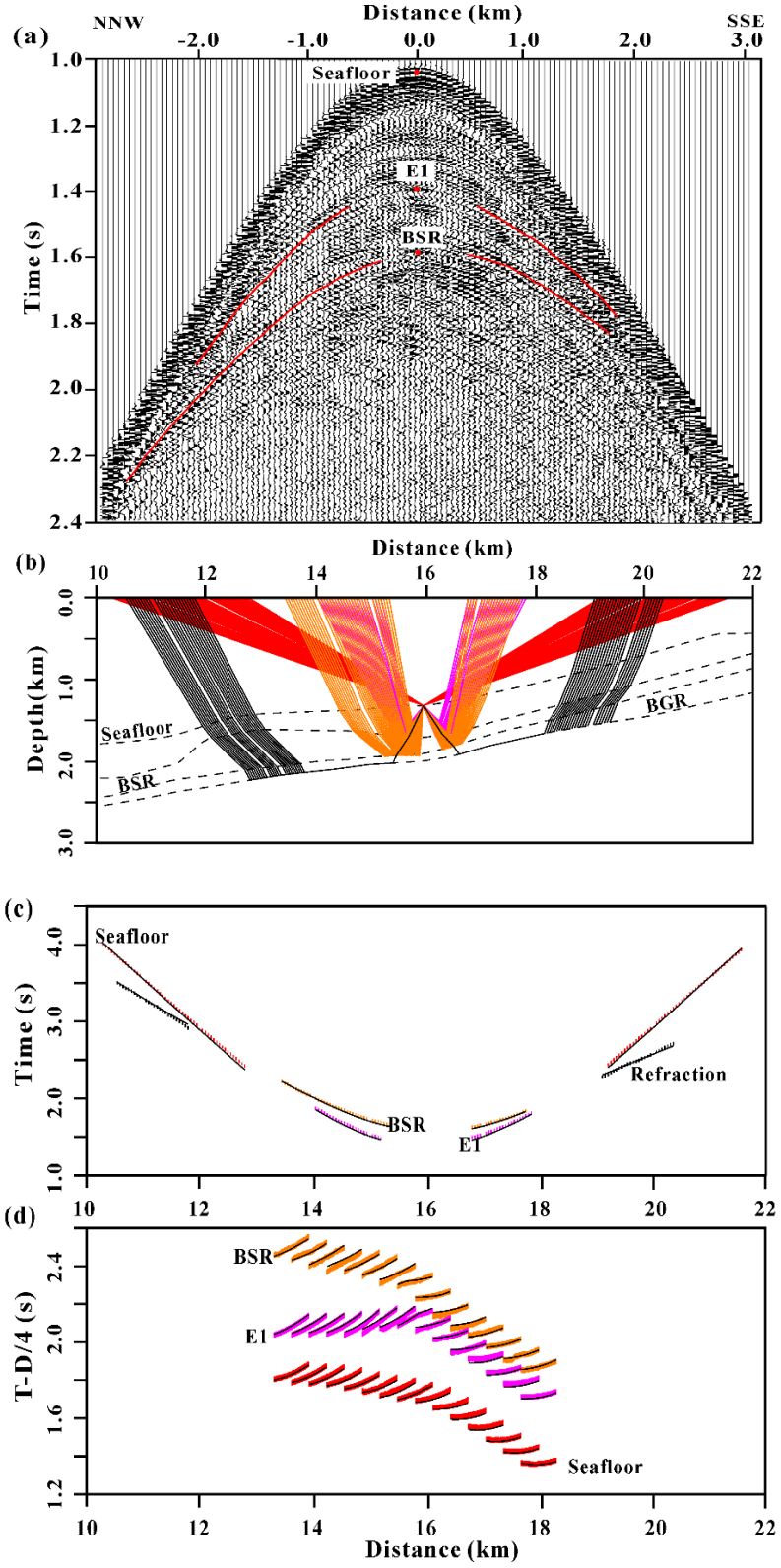

Figure 4. (**a**) Hydrophone component of OBS 7 showing travel time picks (red lines) of P-wave reflections used in the inversion. The horizontal axis is the distance between projected OBS position and shot position. The travel times at minimum offset corresponding to the reflections (Seafloor, E1, BSR) are indicated with the red dots; (**b**) P-wave ray diagram modeled on OBS 7. For clarity, rays modeled on MCS data are not shown; (**c**) the fit between calculated (solid lines) and observed (short

vertical lines) travel times for OBS 7; (**d**) the fit between calculated (solid lines) and observed (short vertical lines) travel times for MCS data. For better visibility, every sixth shot is shown. The MCS time is reduced with a velocity of 4 km/s. The colors of observed travel times are the same as those of corresponding rays in panel (**b**). BGR: base of the free gas layer.

2.2.2. S-Wave Velocity Modeling

S-wave velocities were determined by trial and error forward modeling of the travel times of converted S-waves from the inline component of OBS data. Here, only the PS-wave type was considered. A part of the P-wave energy converts to S-wave energy at a reflector when the energy does not impinge perpendicularly to the reflecting surface, and then propagates back upwards as an S-wave to the receiver. The interface depths and P-wave velocities obtained as described in the previous section were held constant, and the S-wave velocities were modeled by inverting for Poisson's ratio in each layer to have the best fit between the observed and calculated PS travel times. This required the correlation of PS arrivals from the inline component with their equivalent P arrivals from the hydrophone component. Because of the possible ambiguity in this correlation, all the PS events with good signal-to-noise ratio were tested for each layer in order to obtain the event with the optimal fit between calculated and observed travel times. A similar method to estimate S-wave velocities from OBS data has been described in several other studies (e.g., References [43–46]). This procedure was performed on both OBS stations. Figure 5 shows the picking of PS-wave arrivals from the inline component of OBS 7. The inset shows a plot with particle motion and indicates that the energy is mainly horizontal. The two events at about 2.6 s and 2.8 s at minimum offset were identified as PS arrivals corresponding to the BSR and BGR, respectively. A good fit between calculated and observed PS arrivals was obtained, as shown in Figure 5b,c.

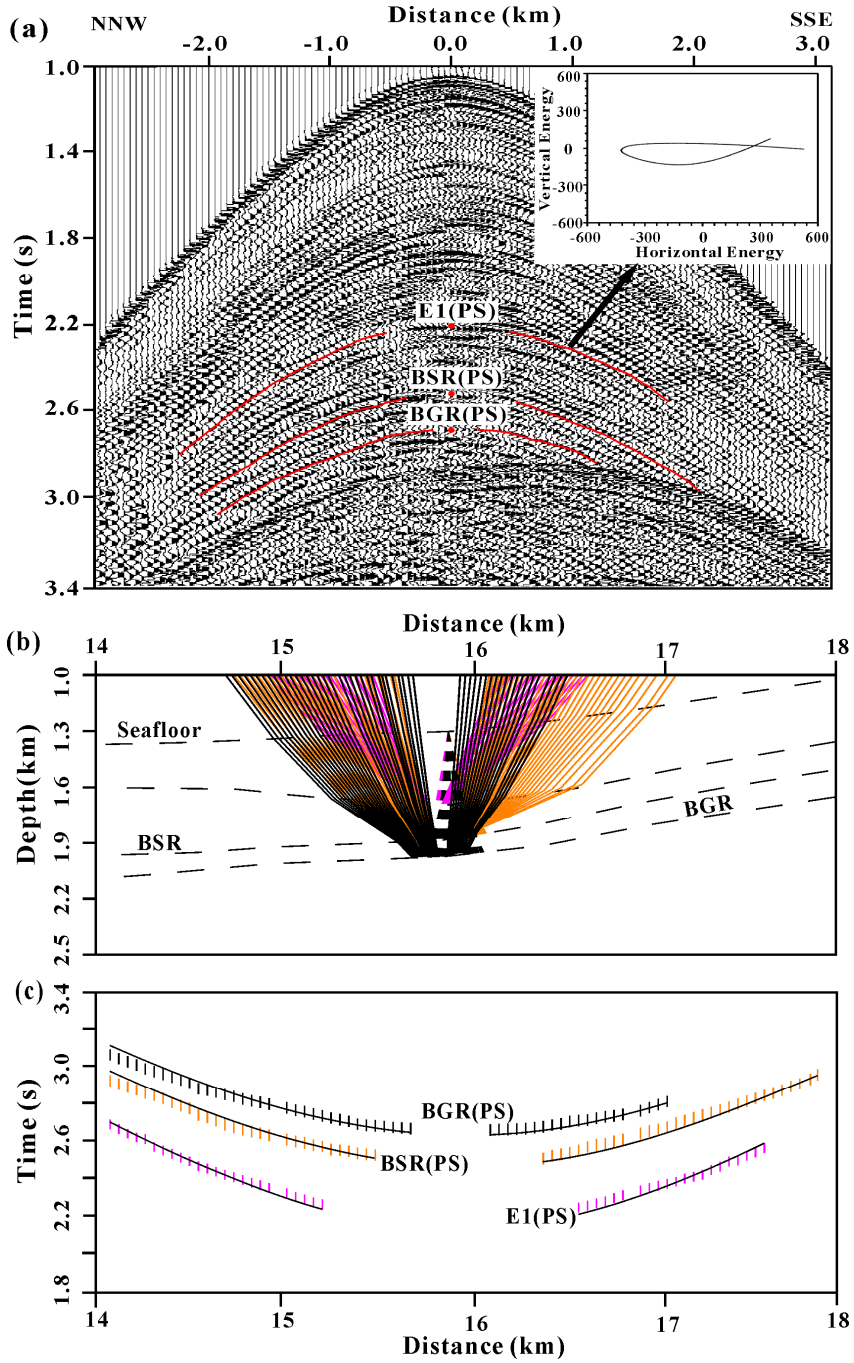

Figure 5. (**a**) Inline component of OBS 7 showing travel time picks (red lines) of PS-waves. The horizontal axis is the distance between projected OBS position and shot position. The travel times at minimum offset corresponding to the PS-waves are indicated with the red dots. The inset shows the particle motion plot for the E1 (PS) event; (**b**) PS-wave ray diagram modeled on OBS 7; (**c**) the fit between calculated (solid lines) and observed (short vertical lines) travel times. The colors of observed travel times are the same as those of corresponding rays in panel (**b**).

2.2.3. Uncertainty of the Velocity Model

There are two primary sources of errors in the final velocity model: projection and travel time inversion. The former is caused by the drift of the OBS from the MCS line during the placement (see Section 2.1). The error in P- and S-wave velocity caused by the geometry projection was evaluated by observing the residual between the calculated and observed travel time picked at near offset of

the OBS data, using the final velocity model. The percentage error is defined as the ratio between travel time residual and observed travel time. In order to estimate the uncertainties of travel time inversion, we performed a sensitivity analysis based on the approach as described in the literature [18]: we perturbed the velocity values of each layer until the RMS travel time residual and normalized χ^2 increased significantly from the values obtained from the final model. The uncertainties in S-wave velocity from travel time inversion were obtained through perturbing the Poisson's ratio, following the similar approach as used for the P-wave velocity. We observed that, as expected, the shallow layers are more sensitive to the variation of Poisson's ratio than the deep layers. In particular, the error in Poisson's ratio in the layer just above and below the BSR is about 0.012 and 0.04, respectively. The estimation of uncertainty in P-wave and S-wave velocities was performed for all the layers including the water column (Layer 1), as shown in Table 1.

Table 1. Percentage errors of P-wave and S-wave velocities estimated from the sensitivity analysis.

Layer	Error in P-Wave Velocity			Error in S-Wave Velocity		
	Projection Error (%)	Inversion Error (%)	Final Error (%)	Projection Error (%)	Inversion Error (%)	Final Error (%)
1	NO	1	1	NO	NO	NO
2	2	5	7	2	4	6
3	1	7	8	1	7	8
4	1	7	8	1	9	10

2.3. Estimation of Gas Hydrate and Free Gas Concentrations

The final velocity field obtained from travel time inversion can be used to estimate the concentrations of gas hydrate and free gas in the pore space. In this study, we adopted the theoretical model proposed by References [30,47] to quantify the amounts of gas hydrate and free gas by converting the velocity anomalies with respect to the reference velocities at full-water saturation. The theoretical model was successfully validated by the Ocean Drilling Program (ODP) data (i.e., Leg 164 [47] and Leg 146 [29]). Positive velocity anomalies are considered as an indication for the presence of gas hydrates, while negative velocity anomalies are considered as caused by free gas. This theoretical model is based on a modified Biot-Geertsma-Smit theory and has been successfully applied in this same geographical area (e.g., Reference [27]). The theory includes an explicit dependence on differential pressure and depth and considers the effects of grain cementation at high concentrations of gas hydrates on the shear modulus of the sediment matrix by using a percolation model [48]. The method gives the equations of both P- and S-wave velocities as functions of some physical parameters, such as porosity, compressibility, rigidity, density, and frequency dependence. These parameters can be determined from experimental datasets (Hamilton's curves [49,50]).

In this study area, no direct measurements for gas hydrate or free gas concentrations are available. The physical parameters (porosity, density, compressibility) adopted for evaluating the reference velocities were taken from Hamilton's dataset for normally compacted terrigenous sediments [49,50]. The Poisson's ratio obtained from travel time inversion of converted S-waves was used to evaluate the rigidity of the sediments in each layer. Low Poisson's ratio and low P-wave velocity indicate that free gas is uniformly distributed in the pore space [30]. A quantitative estimate was obtained by altering the concentration parameters in the theoretical model until modeled seismic velocity matched the theoretical velocity. The uncertainty in concentration estimation is mainly assessed in relation to the uncertainty in the seismic velocities, but also the errors in estimating the physical parameters used to calculate the reference velocities. Previous sensitivity tests performed in this area suggested that porosity is the most important parameter in the estimation of gas hydrate and free gas concentrations, as a variation of $\pm$5% in porosity can be translated into a variation of $\pm$20% and $\pm$7% of gas hydrate and free gas concentrations, respectively [26].

3. Results and Discussion

The final P-wave velocity model determined by the travel time inversion of reflections and refractions from OBS data is shown in Figure 6. The model indicates that the BSR is nearly parallel to the seafloor at about 510–650 m depth below seafloor. The P-wave velocity increases gradually from 1.68 to 1.73 km/s at the seafloor to 2.0 to 2.1 km/s at the BSR. This high P-wave velocity layer with a thickness varying between 150 and300 m just above the BSR can be associated with the presence of gas hydrates. The layer below the BSR shows a low P-wave velocity of about 1.4–1.6 km/s that can be related to the presence of free gas. The BGR occurs at a depth varying between 80 and 160 m below the BSR; in the layer just below the BGR, velocity varies between 2.64 and 2.71 km/s estimated from analysis of the critical refractions in OBS data.

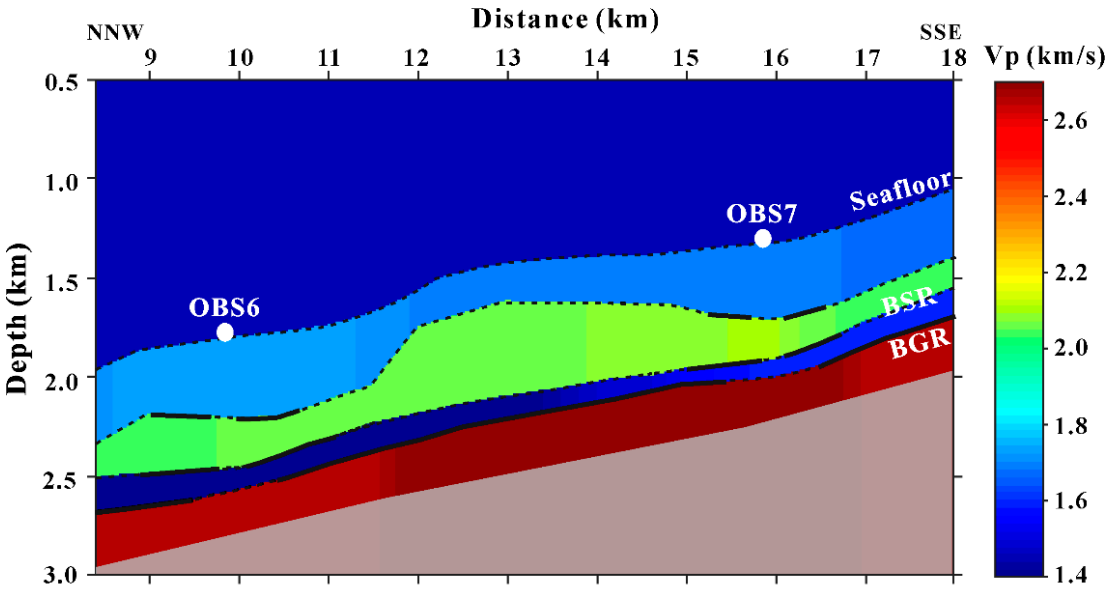

Figure 6. P-wave velocity model determined by inversion of MCS and OBS data. Solid boundary lines indicate the P-wave ray coverage for the different layer interfaces. The grey shading indicates the area with no ray coverage.

A lateral variation is observed along the velocity model. In the shallow layer just below the seafloor, the overall trend of P-wave velocity shows a lateral increase from the SSE to NNW. In the layer just above the BSR, OBS 7 yields higher P-wave velocity compared to OBS 6, which results in the highest velocity of 2.1 km/s occurring in the eastern part, while the lowest velocity equal to 2.0 km/s is present in the western part of section. Velocity also varies in the free gas layer below the BSR. The lowest velocity (1.4 km/s) occurs in the western part where the BSR is stronger. The P-wave velocity field is in general agreement with previous studies in this area [3,27].

Figure 7 shows the vertical profiles of P- and S-wave velocities and Poisson's ratio at the OBS locations. The S-wave velocity shows a continuous increase with depth and reaches a value of about 825 m/s at the BSR. Beneath the BSR, no significant increase or decrease was found, as the S-wave velocity is almost insensitive to pore fluid saturation. For each OBS, the Poisson's ratio shows a relatively continuous decrease with a depth down to BSR and a strong decrease in the free gas layer below the BSR. Moreover, the Poisson's ratio is similar within each layer. In the layer just above the BSR, a value of 0.405 $\pm$ 0.012 and 0.409 $\pm$ 0.012 was observed at OBS 6 and OBS 7, respectively. In the free gas layer, a Poisson's ratio equal to 0.25 $\pm$ 0.04 and 0.29 $\pm$ 0.04 was obtained, respectively. The Poisson's ratio in the gas hydrate and free gas layer presented here are in good agreement with the values obtained from another OBS station as per the location in Figure 1, in the same area analyzed by Reference [3]. Their results show that the Poisson's ratio is 0.405 in the hydrate-bearing sediments

and 0.25 in the gas-bearing sediments. This implies that the Poisson's ratio is fairly uniform, and the gas hydrate reservoir does not show significant variations in this study area.

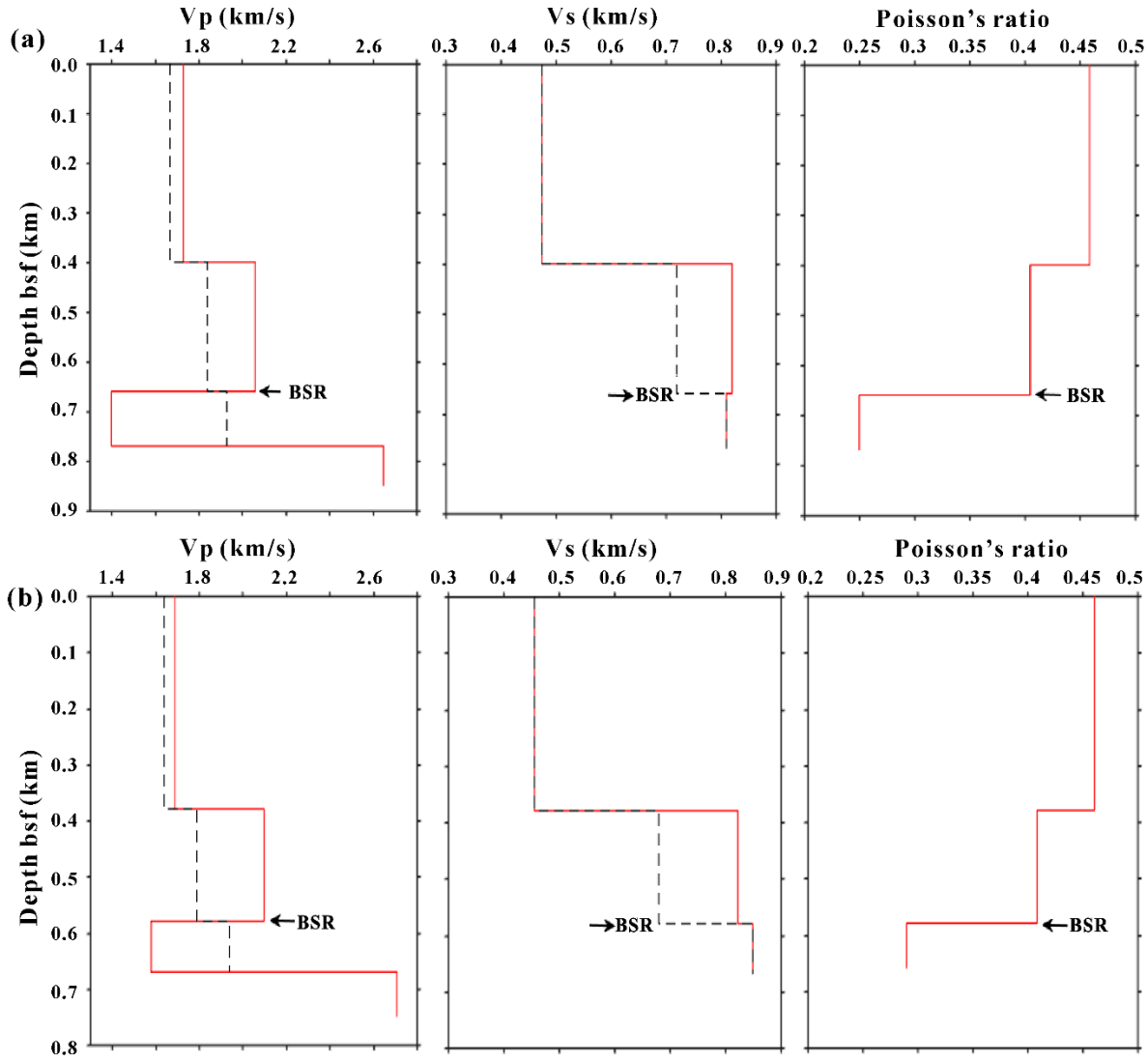

Figure 7. The seismic velocity profiles (red lines) after inversion and reference velocity curves (black dotted lines) and Poisson's ratio profiles extracted at the locations of OBS 6 (**a**) and OBS 7 (**b**). Depth is measured below the seafloor (bsf).

Figure 8 shows the gas hydrate and free gas concentration estimated by comparing the P-wave and S-wave velocity anomalies with the reference velocities. The result indicates that gas hydrate concentration varies from 3% to 7% of total volume in the first layer below the seafloor, while it is in the range of 10% to 15% of total volume in the layer just above the BSR, and free gas concentration is estimated in the range of 0.3% to 0.8% of total volume assuming a uniform distribution in the pore space. Errors related to assumed physical parameters [26] and estimated velocity, as shown in Table 1, correspond to errors in the estimation of gas hydrate and free gas concentrations of about 5% and 0.3% of total volume, respectively. Considering these errors, gas hydrate concentration in the first layer below the seafloor might be close to 0, which means that hydrates probably are not present. Therefore, we suppose that there are water-bearing sediments in the layer just below the seafloor, or, if hydrates are present, the concentration is negligible. This result agrees with previous studies (e.g., References [27,28]). The concentration section does not show any significant lateral variation for gas hydrates or free gas concentrations, respectively. The estimated concentration is comparable

with previous studies in this area by other authors. For example, Reference [51] obtained an average concentration of 17.7 and 0.3 percent of volume in the case of gas hydrate and free gas, respectively. If we consider the gas hydrate concentration as a percentage of pore space, it is equal to about 23% to 35% of pore space, which is consistent with the value (23% of pore space) obtained from another OBS analysis by Reference [3] in the same study area. We also compared the estimated hydrate concentrations with the study in the Chilean margin, where the here adopted theoretical model for estimating concentrations was used (e.g., References [52–55]. The distribution and concentration of gas hydrates along the Chilean margin show strong variation, but comparable concentrations to ours can be observed in some sites [52,54].

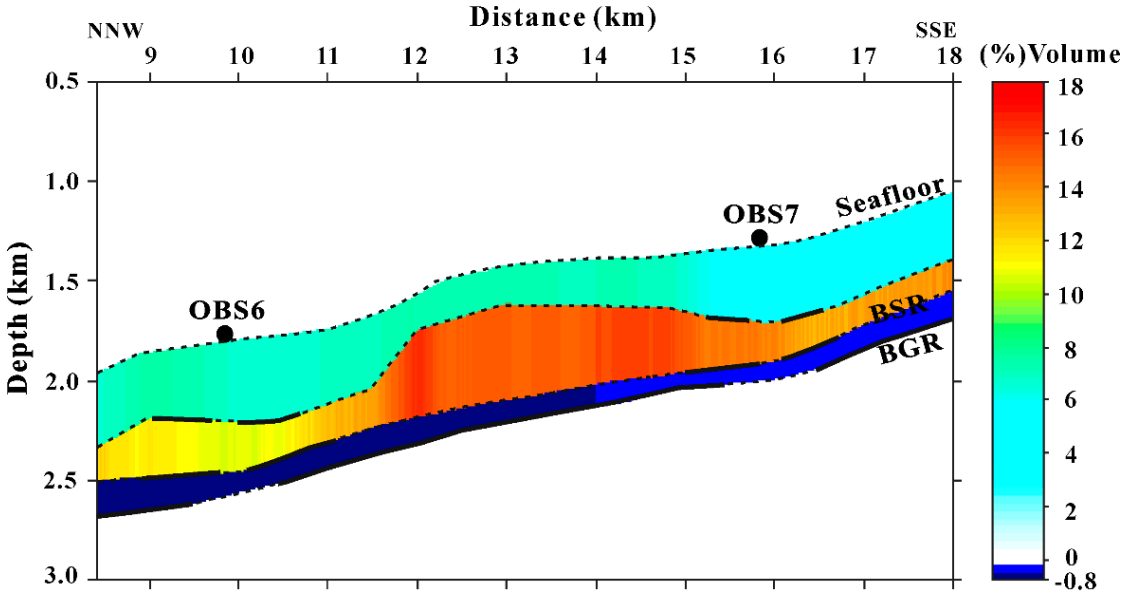

Figure 8. Concentration section of gas hydrate (positive values) and free gas (negative values).

The analysis of OBS data has enabled the obtaining of the information of both P- and S-wave velocity fields and it provides new insights into the distribution and quantification of gas hydrate and free gas in marine sediments in the South Shetland margin. The relatively uniform Poisson's ratio of gas hydrate reservoirs can provide an additional clue for evaluating the rigidity of sediment and thus a reliable concentration when no direct measurements are available. The high concentrations of gas hydrate and free gas suggest that they could be considered as future energy sources. This study can also provide a valuable contribution to the investigation of the relationship between gas hydrate stability and climate change as the polar areas are the most sensitive to global change.

4. Conclusions

The analysis of MCS and OBS data has allowed us to characterize the gas hydrate reservoir in the South Shetland margin. Inversion performed on OBS data provides detailed P- and S-wave velocity information of the subsurface allowing the obtaining of a reliable estimate of gas hydrate and free gas concentrations. The main conclusions of this study are as follows:

(1) We observe a high P-wave velocity layer of 2.0–2.1 km/s just above the BSR, which can be attributed to the presence of gas hydrates. The gas hydrate concentration in this layer is about 10% to 15% of total volume.

(2) We observe a low velocity layer of 1.4–1.6 km/s below the BSR, indicating the presence of free gas. The free gas concentration is about 0.3% to 0.8% of total volume, assuming a uniform distribution of free gas in the pore space.

(3) The Poisson's ratio obtained by forward modeling of converted S-waves shows good agreement with the previous study performed in this area. This comparison allows us to conclude that the gas hydrate reservoir in this study area shows no significant regional variations from a petrophysical point of view.

Author Contributions: Conceptualization and methodology, U.T., M.G., and G.C.; software, S.S. (Sha Song), S.S. (Sunny Singhroha), and S.B.; supervision, G.C.; investigation, writing—original draft preparation, S.S. (Sha Song); writing—review and editing, U.T., M.G., S.S. (Sunny Singhroha), S.B., and G.C.

Funding: This research was partially supported by the Italian Ministry of Education, Universities and Research (Decreto MIUR No. 631 dd. 8 August 2016) under the extraordinary contribution for Italian participation in activities related to the international infrastructure PRACE—The Partnership for Advanced Computing in Europe (www.prace-ri.eu). Sha Song was supported by the China Scholarship Council grant number 201506400061, and her Short Term Scientific Mission at the CAGE—Centre for Arctic Gas Hydrate, Environment and Climate, Department of Geosciences, UiT The Arctic University of Norway was supported by the Management Committee of the COST-MIGRATE Action (reference code ES1405-050317-082155). Sunny Singhroha and Stefan Bünz were supported by the Research Council of Norway through its Centres of Excellence funding scheme grant No. 223259.

Acknowledgments: The geophysical data were acquired in the frame of the project "Gas Hydrates: impact on climate environmental of the sub-Antarctic regions (BSR)" supported by the Italian National Antarctic Program (PNRA). Sunny Singhroha and Stefan Bünz were supported by the Research Council of Norway through its Centres of Excellence funding scheme, project number 223259/F5.

Conflicts of Interest: The authors declare no conflict of interest.

References

1. Sloan, E.D. *Clathrate Hydrates of Natural Gases*, 2nd ed.; Marcel Dekker, Inc.: New York, NY, USA, 1998; pp. 1–641. ISBN 0824799372.
2. Kvenvolden, K.A. Gas hydrates-geological perspective and global change. *Rev. Geophys.* **1993**, *31*, 173–187. [CrossRef]
3. Tinivella, U.; Accaino, F. Compressional velocity structure and Poisson's ratio in marine sediments with gas hydrate and free gas by inversion of reflected and refracted seismic data (South Shetland Islands, Antarctica). *Mar. Geol.* **2000**, *164*, 13–27. [CrossRef]
4. Boswell, R.; Collett, T.S. Current perspectives on gas hydrate resources. *Energy Environ. Sci.* **2011**, *4*, 1206–1215. [CrossRef]
5. Johnson, A. Global resource potential of gas hydrate—A new calculation. *Fire Ice Dep. Energy Nat. Energy Technol. Lab. Newsl.* **2011**, *11*, 1–4.
6. Collett, T.S.; Boswell, R. Resource and hazard implications of gas hydrates in the Northern Gulf of Mexico: Results of the 2009 Joint Industry Project Leg II Drilling Expedition. *Mar. Petrol. Geol.* **2012**, *34*, 1–3. [CrossRef]
7. Yelisetti, S.; Spence, G.D.; Riedel, M. Role of gas hydrates in slope failure on frontal ridge of northern Cascadia margin. *Geophys. J. Int.* **2014**, *199*, 441–458. [CrossRef]
8. Li, A.; Davies, R.J.; Yang, J. Gas trapped below hydrate as a primer for submarine slope failures. *Mar. Geol.* **2016**, *380*, 264–271. [CrossRef]
9. Kvenvolden, K.A. Potential effects of gas hydrate on human welfare. *Proc. Natl. Acad. Sci. USA* **1999**, *96*, 3420–3426. [CrossRef] [PubMed]
10. Kvenvolden, K.A. A primer on the geological occurrence of gas hydrate. In *Gas Hydrates: Relevance to World Margin Stability and Climate Change*; Henniet, J.P., Mienert, J., Eds.; Geological Society: London, UK, 1998; Volume 137, pp. 9–30. [CrossRef]
11. Kennett, J.P.; Cannariato, K.G.; Hendy, I.L.; Behl, R.J. Methane Hydrates in Quaternary Climate Change: The Clathrate Gun Hypothesis. In *Methane Hydrates in Quaternary Climate Change: The Clathrate Gun Hypothesis*; American Geophysical Union: Washington, DC, USA, 2003; Volume 54, pp. 1–217. ISBN 9781118665138.
12. Bünz, S.; Mienert, J.; Vanneste, M.; Andreassen, K. Gas hydrates at the Storegga Slide: Constraints from an analysis of multi-component, wide-angle seismic data. *Geophysics* **2005**, *70*, B19–B34. [CrossRef]
13. Mienert, J.; Vanneste, M.; Bünz, S.; Andreassen, K.; Haflidason, H.; Sejrup, H.P. Ocean warming and gas hydrate stability on the mid-Norwegian margin at the Storegga Slide. *Mar. Pet. Geol.* **2005**, *22*, 233–244. [CrossRef]

14. Ruppel, C.D. Methane Hydrates and Contemporary Climate Change. *Nat. Educ. Knowl.* **2011**, *3*, 29.
15. Ruppel, C.D.; Kessler, J.D. The interaction of climate change and methane hydrates. *Rev. Geophys.* **2017**, *55*, 126–168. [CrossRef]
16. Hyndman, R.D.; Spence, G.D. A seismic study of methane hydrate marine bottom simulating reflectors. *J. Geophys. Res.* **1992**, *97*, 6683–6698. [CrossRef]
17. Singh, S.C.; Minshull, T.A.; Spence, G.D. Velocity structure of a gas hydrate reflector. *Science* **1993**, *260*, 104–207. [CrossRef] [PubMed]
18. Katzman, R.; Holbrook, W.S.; Paull, C.K. Combined vertical-incidence and wide-angle seismic study of a gas hydrate zone, Blake ridge. *J. Geophys. Res.* **1994**, *99*, 17975–17995. [CrossRef]
19. Korenaga, J.; Holbrook, W.S.; Singh, S.C.; Minshull, T.A. Natural gas hydrates on the southeast US margin: Constraints from full waveform and travel time inversions of wide-angle seismic data. *J. Geophys. Res.* **1997**, *102*, 15345–15365. [CrossRef]
20. Kumar, D.; Sen, M.K.; Bangs, N.L. Gas hydrate concentration and characteristics within Hydrate Ridge inferred from multicomponent seismic reflection data. *J. Geophys. Res.* **2007**, *112*. [CrossRef]
21. Helgerud, M.; Dvorkin, J.; Nur, A.; Sakai, A.; Collett, T. Elastic-wave velocity in marine sediments with gas hydrates: Effective medium modeling. *Geophys. Res. Lett.* **1999**, *26*, 2021–2024. [CrossRef]
22. Chand, S.; Minshull, T.A.; Gei, D.; Carcione, J. Elastic velocity models for gas-hydrate-bearing sediments—A comparison. *Geophys. J. Int.* **2004**, *159*, 573–590. [CrossRef]
23. Dash, R.; Spence, G.D. P-wave and S-wave velocity structure of northern Cascadia margin gas hydrates. *Geophys. J. Int.* **2011**, *187*, 1363–1377. [CrossRef]
24. Andreassen, K.; Berteussen, K.A.; Sognnes, H.; Henneberg, K.; Langhammer, J.; Mienert, J. Multicomponent ocean bottom cable data in gas hydrate investigation offshore of Norway. *J. Geophys. Res.* **2003**, *108*, 2399. [CrossRef]
25. Petersen, C.J.; Papenberg, C.; Klaeschen, D. Local seismic quantification of gas hydrates and BSR characterization from multi-frequency OBS data at northern Hydrate Ridge. *Earth Planet Sci. Lett.* **2007**, *255*, 414–431. [CrossRef]
26. Tinivella, U.; Accaino, F.; Camerlenghi, A. Gas hydrate and free gas distribution form inversion of seismic data on the South Shetland margin (Antarctica). *Mar. Geophys. Res.* **2002**, *23*, 109–123. [CrossRef]
27. Loreto, M.F.; Tinivella, U.; Accaino, F.; Giustiniani, M. Gas hydrate reservoir characterization by geophysical data analysis (offshore Antarctic Peninsula). *Energies* **2011**, *4*, 39–56. [CrossRef]
28. Loreto, M.F.; Tinivella, U. Gas hydrate versus geological features: The South Shetland case study. *Mar. Pet. Geol.* **2012**, *36*, 164–171. [CrossRef]
29. Tinivella, U.; Carcione, J.M. Estimation of gas-hydrate concentration and free-gas saturation from log and seismic data. *Lead. Edge* **2001**, *20*, 200–203. [CrossRef]
30. Tinivella, U. The seismic response to overpressure versus gas hydrate and free gas concentration. *J. Seism. Explor.* **2002**, *11*, 283–305.
31. Tinivella, U.; Accaino, F.; Della Vedova, B. Gas hydrates and active mud volcanism on the South Shetland continental margin, Antarctic Peninsula. *Geo-Mar. Lett.* **2008**, *28*, 97–106. [CrossRef]
32. Maldonado, A.; Larter, R.D.; Aldaya, F. Forearc tectonic evolution of the South Shetland Margin, Antarctic Peninsula. *Tectonics* **1994**, *13*, 1345–1370. [CrossRef]
33. Kim, Y.; Kim, H.S.; Larter, R.D.; Camerlenghi, A.; Gambôa, L.A.P.; Rudowski, S. Tectonic deformation in the upper crust and sediments at the South Shetland Trench. In *Geology and Seismic Stratigraphy of the Atlantic Margin*; Cooper, A.K., Barker, P.T., Brancolini, G., Eds.; American Geophysical Union: Washington, DC, USA, 1995; Volume 68, pp. 157–166. ISBN 9781118669013.
34. Pankhurst, R.J. The Paleozoic and Andean magmatic arcs of West Antarctica and southern South America. In *Plutonism from Antarctica to Alaska*; Kay, S.M., Rapela, C.W., Eds.; Geological Society of Amer: Boulder, CO, USA, 1990; Volume 241, pp. 1–7. ISBN 9780813722412.
35. Larter, R.D.; Barker, P.F. Effects of ridge crest-trench interaction on Antarctic-Phoenix spreading: Forces on a young subducting plate. *J. Geophys. Res.* **1991**, *96*, 19583–19607. [CrossRef]
36. Jin, Y.K.; Larter, R.D.; Kim, Y.; Nam, S.H.; Kim, K.J. Post-subduction margin structures along Boyd Strait, Antarctic Peninsula. *Tectonophysics* **2002**, *346*, 187–200. [CrossRef]

37. Dietrich, R.; Rülke, A.; Ihde, J.; Lindner, K.; Miller, H.; Niemeier, W.; Schenke, H.W.; Seeber, G. Plate kinematics and deformation status of the Antarctic Peninsula based on GPS. *Glob. Planet. Chang.* **2004**, *42*, 313–321. [CrossRef]
38. Marín-Moreno, H.; Giustiniani, M.; Tinivella, U.; Pinero, E. The challenges of quantifying the carbon stored in Arctic marine gas hydrate. *Mar. Pet. Geol.* **2016**, *71*, 76–82. [CrossRef]
39. Cohen, J.K.; Stockwell, J.W. *CWP/SU: Seismic Unix Release 4.0: A free Package for Seismic Research and Processing*; Center for Wave Phenomena, Colorado School of Mines: Golden, CO, USA, 2008; pp. 1–153.
40. Gaiser, J.E. Applications for vector coordinate systems of 3-D converted wave data. *Lead. Edge* **1999**, *18*, 1290–1300. [CrossRef]
41. Zelt, C.A.; Smith, R.B. Seismic travel time inversion for 2-D crustal velocity structure. *Geophys. J. Int.* **1992**, *108*, 16–34. [CrossRef]
42. Yelisetti, S. Seismic structure, gas hydrate, and slumping studies on the Northern Cascadia margin using multiple migration and full waveform inversion of OBS and MCS data. Ph.D. Thesis, University of Victoria, Victoria, BC, Canada, 2014.
43. Westbrook, G.K.; Chand, S.; Rossi, G.; Long, S.; Bünz, S.; Camerlenghi, A.; Carcione, J.M.; Dean, S.; Foucher, J.P.; Flueh, E.; et al. Estimation of gas-hydrate concentration from multi-component seismic data at sites on the continental margins of NW Svalbard and the Storegga region of Norway. *Mar. Pet. Geol.* **2008**, *25*, 744–758. [CrossRef]
44. Peacock, S.; Westbrook, G.K.; Bais, G. S-wave velocities and anisotropy in sediments entering the Nankai subduction zone, offshore Japan. *Geophys. J. Int.* **2010**, *180*, 743–758. [CrossRef]
45. Exley, R.J.K.; Westbrook, G.K.; Haacke, R.R.; Peacock, S. Detection of Seismic anisotropy using ocean bottom seismometers: A case study from northern headwall of Storegga Slide. *Geophys. J. Int.* **2010**, *183*, 188–210. [CrossRef]
46. Satyavani, N.; Sain, K.; Gupta, H.K. Ocean bottom seismometer data modeling to infer gas hydrate saturation in Krishna-Godavari (KG) basin. *J. Nat. Gas Sci. Eng.* **2016**, *33*, 908–917. [CrossRef]
47. Tinivella, U. A method for estimating gas hydrate and free gas concentrations in marine sediments. *Boll. Geofis. Teor. Appl.* **1999**, *40*, 19–30.
48. Leclaire, P. Propagation Acoustique dans les Milieux Poreux Soumis au Gel-Modélisation et Expérience. Ph.D. Thesis, Université Paris, Paris, France, 1992.
49. Hamilton, E.L. Variations of density and porosity with depth in deep-sea sediments. *J. Sediment. Res.* **1976**, *46*, 280–300.
50. Hamilton, E.L. *Vp/Vs* and Poisson's ratios in marine sediments and rocks. *J. Acoust. Soc. Am.* **1979**, *66*, 1093–1101. [CrossRef]
51. Tinivella, U.; Loreto, M.F.; Accaino, F. Regional versus detailed velocity analysis to quantify hydrate and free gas in marine sediments: The south Shetland margin target study. *Geol. Soc. Spec. Publ.* **2009**, *319*, 103–119. [CrossRef]
52. Vargas-Cordero, I.; Tinivella, U.; Villar-Muñoz, L.P.; Bento, J. High Gas Hydrate and Free Gas Concentrations: An Explanation for Seeps Offshore South Mocha Island. *Energies* **2018**, *11*, 3062. [CrossRef]
53. Villar-Muñoz, L.; Bento, J.P.; Klaeschen, D.; Tinivella, U.; Vargas-Cordero, I.; Behrmann, J.H. A first estimation of gas hydrates offshore Patagonia (Chile). *Mar. Pet. Geol.* **2018**, *96*, 232–239. [CrossRef]
54. Vargas-Cordero, I.; Tinivella, U.; Villar-Muñoz, L. Gas Hydrate and Free Gas Concentrations in Two Sites inside the Chilean Margin (Itata and Valdivia Offshores). *Energies* **2017**, *10*, 2154. [CrossRef]
55. Vargas-Cordero, I.; Tinivella, U.; Accaino, F.; Loreto, M.F.; Fanucci, F. Thermal state and concentration of gas hydrate and free gas of Coyhaique, Chilean Margin (44°30′ S). *Mar. Pet. Geol.* **2010**, *27*, 1148–1156. [CrossRef]